Quantum Transport Experiments in Strain-Engineered Graphene

Inauguraldissertation

zur
Erlangung der Würde eines Doktors der Philosophie
vorgelegt der
Philosophisch-Naturwissenschaftlichen Fakultät
der Universität Basel

von

Lujun Wang
aus China

Basel, 2020

Originaldokument gespeichert auf dem Dokumentenserver der Universität Basel
edoc.unibas.ch

Genehmigt von der Philosophisch-Naturwissenschaftlichen Fakultät
auf Antrag von
Prof. Dr. Christian Schönenberger
Prof. Dr. Christoph Stampfer
Prof. Dr. Dmitri K. Efetov

Basel, 17.12.2019

Prof. Dr. Martin Spiess
Dekan

Contents

1. Introduction 1

2. Theoretical background 5
- 2.1. Basics of graphene 6
  - 2.1.1. From lattice structure to band structure 6
  - 2.1.2. Pseudospin and Berry-phase 10
  - 2.1.3. Bilayer graphene 11
- 2.2. Charge transport in graphene 13
  - 2.2.1. Field effect 13
  - 2.2.2. Diffusive regime and Drude model 14
  - 2.2.3. Ballistic transport 15
  - 2.2.4. Phase coherent transport 16
  - 2.2.5. Quantum Hall effect in graphene 19
- 2.3. Strain in graphene 21
  - 2.3.1. Strain effects on electronic properties 21
  - 2.3.2. Valley Hall and inverse valley Hall effect 24
  - 2.3.3. Strain characterization with Raman spectroscopy 26
- 2.4. Moiré superlattice 30
  - 2.4.1. Formation of graphene/hBN superlattice 30
  - 2.4.2. Band structure modification 31

3. Experimental methods 35
- 3.1. Sample fabrication 36
  - 3.1.1. Exfoliation 36
  - 3.1.2. Suspension 37
  - 3.1.3. Encapsulation 38
- 3.2. Strain setup 41
  - 3.2.1. Flexible substrate preparation 41
  - 3.2.2. Three-point bending setup 42
- 3.3. Low-temperature electrical measurements 43
  - 3.3.1. Electrical connection 44
  - 3.3.2. Cryogenic measurement setup 45

4. Suspended multiterminal bilayer graphene and non-local signal 47
- 4.1. Introduction 48
- 4.2. Local and non-local signal 49

4.3. Temperature dependence of local and non-local signal 51
4.4. Bias spectroscopy 53
4.5. Discussion, conclusion and outlook 55

5. In situ strain tuning in graphene 57
5.1. Introduction 58
5.2. Strain tuning in suspended graphene 59
5.3. Strain tuning in suspended encapsulated graphene 60
5.4. Strain tuning in on-substrate encapsulated graphene 61
    5.4.1. Device design for different strain fields 62
    5.4.2. Strain fields mapping with spatial Raman spectroscopy 63
    5.4.3. Raman maps of hBN peak 68
    5.4.4. Clamping of edge contacts 68
    5.4.5. Edge contact failure 70
    5.4.6. First transport measurements 71
5.5. Conclusion and outlook 73

6. Mobility enhancement in graphene by in situ reduction of random strain fluctuations 75
6.1. Introduction 76
6.2. Experimental setup and fabrication 77
6.3. Field-effect measurements and mobility extraction 77
6.4. Analysis of fitting results 79
6.5. Raman measurements 81
6.6. Weak localization measurements 83
6.7. Device without mobility enhancement 84
6.8. Conclusion and outlook 84

7. Strain effects in transport experiments 87
7.1. Introduction 88
7.2. Strain setup and device geometries 88
7.3. Strain-induced scalar potential 89
7.4. Strain effects in conductance fluctuations 92
7.5. Strain effects in transverse magnetic focusing 95
7.6. Strain effects in quantum Hall regime 100
    7.6.1. Square devices 100
    7.6.2. Two-terminal trapezoidal devices 102
    7.6.3. Multi-terminal trapezoidal devices 105
7.7. Conclusion and outlook 108

8. Super-superlattice in doubly aligned hBN/graphene/hBN heterostructures 109
8.1. Introduction 110

8.2. Moiré superlattices illustration 111
8.3. Transport experiments and results 112
  8.3.1. Device fabrication 112
  8.3.2. Zero magnetic field measurements 112
  8.3.3. Quantum Hall measurements 113
8.4. Geometrical analysis 115
  8.4.1. Geometrical analysis for super-superlattice 115
  8.4.2. Period for super-superlattice 117
  8.4.3. Comparison to measurements 118
8.5. Measurements on a second sample 118
8.6. Conclusion and outlook 119

9. Summary and Outlook 121

Bibliography 125

A. Fabrication Recipes 141
A.1. Fabrication of LOR-based suspended graphene samples 141
  A.1.1. Bottom gate structures 141
  A.1.2. LOR coating and opening for bonding pads 141
  A.1.3. Lithography on LOR 142
  A.1.4. Suspension of graphene 142
A.2. Preparation of flexible substrate 142
A.3. Fabrication of encapsulated graphene 142
  A.3.1. Wafer preparation and exfoliation 142
  A.3.2. Assembly of hBN/graphene/hBN stacks 143
A.4. E-beam lithography and development 143
  A.4.1. PMMA resist with xylene as developer 143
  A.4.2. PMMA resist with cold-development 143
A.5. Reactive ion etching 144
  A.5.1. CHF_3:O_2 plasma 144
  A.5.2. SF_6:Ar:O_2 plasma 144
  A.5.3. O_2 plasma 144
A.6. Metal evaporation 144
  A.6.1. Pd leads 144
  A.6.2. Cr/Au leads 145

B. Further data and discussions of strain tuning in graphene 147
B.1. Edge contact reinforcement 147
B.2. Scatter plot of ω_{2D} versus ω_{G} 148
B.3. FEM simulations of strain 148
B.4. Discussions on transport measurements of the suspended encapsulated device 150

C. Further data and discussions on mobility enhancement experiments 151
C.1. Geometry factor and reversibility of the strain induced mobility increase . . . 151
C.2. Analysis of the hole side . . . 152
C.3. Second device with mobility-increase effect . . . 154
C.4. Raman spectroscopy . . . 154

D. Additional information and discussions on strain effects in various transport experiments 157
D.1. Conductance fluctuations in gate voltage . . . 157
D.2. Classical Hall effect in Sample3 B . . . 159
D.3. Comparison in quantum Hall regime . . . 160

E. Further data and discussions of super-superlattice 163
E.1. Fabrication . . . 163
E.2. Other devices of sample a . . . 163
E.2.1. Device a3 . . . 165
E.3. Other devices of sample b . . . 165

Curriculum Vitae 169

Publications 171

Acknowledgements 175

1 Introduction

Strictly two-dimensional (2D) crystals were thought to be thermodynamically unstable [1, 2] until the first successful isolation of graphene in 2004 [3]. Graphene is a sheet of carbon atoms arranged in a honeycomb structure, which has proved to be a wonder material with many exceptional properties [4–8]. The great interest for quantum transport lies in the unique electronic band structure of graphene, which was already derived by Wallace in the 1940s [9]. The most striking difference from conventional metals and semiconductors is the low energy linear dispersion relation, which makes the charge carriers in graphene massless Dirac-like. The Dirac nature of the charge carries were confirmed by the experimental observation of the half-integer quantum Hall effect in 2005 [10, 11]. Shortly after that, many other characteristic physical phenomena were predicted and observed in graphene, such as Klein tunneling [12–14], distinct quantum interference effects [15, 16], or giant intrinsic mobility [17, 18].

Although graphene has many superlatives to its name [7], it is not omnipotent. Advantages in one case can become disadvantages in another, for example, the zero band gap for transistor applications [19], or the weak intrinsic spin orbit coupling for spin manipulation [20]. Different engineering approaches have been proposed and used to tailor and enrich the electronic properties of graphene, such as proximity effect and strain engineering.

Graphene is a semimetal [21], but its advent triggered the discovery of a big family of 2D materials spanning a wide spectrum of electronic behaviors: hexagonal boron nitride (hBN) is an insulator [22], MoS_2 is a semiconductor [23], $NbSe_2$ is a superconductor [24], WTe_2 is a topological insulator [25–27] and CrI_3 is a ferromagnet [28]. By placing graphene in proximity to other materials, new electronic properties can be induced in graphene, including ferromagnetism [29, 30], the formation of Andreev states [31, 32], and enhanced spin-orbit coupling [33, 34]. When the graphene lattice is aligned to another similar lattice, a moiré superlattice forms that leads to many new physical observations, such as secondary Dirac points [35–37], the Hofstadter Butterfly [35–39], and strongly correlated states [40, 41].

Graphene has been shown to be the strongest material ever measured and can sustain an elastic tensile strain up 25% [42]. Such a large mechanical strength enables one to modify the electronic properties of graphene by strain engineering [7, 43]. A series of fascinating effects have been predicted for strained graphene, including the appearance of a scalar potential [44], pseudomagnetic fields [44–46], valley filtering [47, 48] and superconductivity [49]. In order to study strain effects in transport experiments, several challenges need to be overcome simultaneously. First, the graphene quality must be preserved after complex fabrication processes, since the observation of strain effects might be hindered by disorder. Second, the strain generation must be compatible with transport measurements, namely the devices should be equipped with electrical contacts and gate structures. Furthermore, mechanical deformations should not degrade the sample quality or generate any artificial effects, such as changes in the gate capacitance, that complicates the analysis of actual strain effects. Most importantly, the strain should be in situ tunable so that strain effects can be disentangled from other effects.

The aim of this thesis is to study electronic transport in graphene with engineered properties. Although numerous engineering approaches are possible, in this thesis, we restrict our focus to strain engineering and moiré superlattices. We first show the development of a straining method that meets all the above mentioned requirements. Then a series of text book mesoscopic transport experiments are studied in the presence of in situ strain tuning. In addition, moiré superlattice engineering from both interfaces of graphene is presented.

Outline of this thesis

The thesis starts with an introduction to relevant theoretical concepts in **chapter 2**. The crystal structure and the unique band structure of graphene are first described, followed by an introduction to basic transport concepts in graphene. Then, different strain effects and the characterization of strain in graphene are discussed. Furthermore, a brief introduction to moiré superlattice effects is given. In **chapter 3**, an overview of the most important fabrication techniques and experimental setups is given. The preparation of flexible substrates and the mechanism for strain generation are shown, followed by a description of the low temperature transport measurement concepts. **Chapter 4** presents the investigation of multiterminal suspended bilayer graphene devices, where an unexpected non-local signal that cannot be attributed to current spread is observed near the charge neutrality point. Different experimental attempts are made to find out the nature of the non-local signal, which however remains to be an open question. The deterministic and reproducible in situ strain tuning in graphene using a three-point bending setup is shown in **chapter 5**. We use spatially resolved Raman spectroscopy to demonstrate that a homogeneous strain field can be achieved with a rectangular device geometry and a strain gradient can be realized in a trapezoidal-shaped device. Additionally, in the first transport experiments with strain we show that the on-substrate encapsulated graphene approach offers two key advantages, including the preservation of the exceptional quality of pristine graphene and the avoidance of gate capacitance change during the deformation process. Even thought the graphene is encapsulated by hBN, microscopic corrugations are still present, which results in random strain fluctuations (RSFs) in the graphene lattice. In **chapter 6**, we show that the RSFs limit the carrier mobility of most high-quality encapsulated graphene devices. With our straining method, the RSFs can be in situ reduced in individual devices. In low-temperature transport measurements, a strong correlation between an increase in carrier mobility and a decrease in residual doping is found when the global strain is increased uniaxially in the graphene. Furthermore, the in situ reduction of RSFs by global straining is substantiated by Raman spectroscopy measurements. In **chapter 7**, different strain effects in various transport experiments are presented and discussed. First, the strain-induced scalar potential is shown, which manifests as a shift of the conductance curve in gate voltage. We then move on to conductance fluctuations measurements, where a shift of the fluctuation features with strain in magnetic field is found. In transverse magnetic focusing measurements, we show an amplitude increase and a position change of the focusing peaks with strain. In the end, strain effects in quantum Hall regime are presented for devices with different geometries. A complete different behavior with strain is found for the trapezoidal devices from that for the square devices. Our fully hBN-encapsulated devices show state-of-the-art transport characteristics, which is exemplified by the formation of a three-layer moiré superlattice in **chapter 8**. The transport signatures of graphene/hBN two-layer moiré superlattices were discovered a couple of years ago [35–37]. In this chapter, we show the transport signature of a super-superlattice, which occurs when both the top and the bottom hBN layers are aligned to the graphene lattice. The overlay of the two two-layer moiré superlattices results in a third superlattice, whose period can be larger than the maximum period ($\sim$14 nm) in a graphene/hBN system. A simple model based on geometrical analysis is also given there for predicting the period of the super-superlattice.

Finally, we summarize the main findings of this thesis in **chapter 9**, where a brief outlook is given as well.

2 Theoretical background

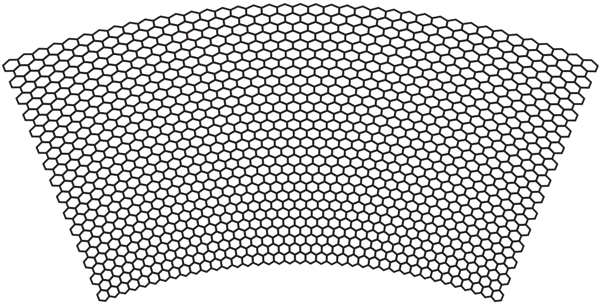

This chapter provides the most important theoretical concepts that are needed for the experiments presented in this thesis. First, an introduction to the crystal structure of graphene and its peculiar band structure is given. Second, some basic concepts of charge transport in graphene, such as field effect, ballistic transport and quantum Hall effect, are introduced. Furthermore, the band structure modification by strain and the induced effects are discussed, including the appearance of a scalar potential and pseudomagnetic fields. Apart from that, the principle of strain characterization by Raman spectroscopy is introduced. In the end, an additional section is dedicated to the moiré superlattice effects when the graphene lattice is aligned to another similar lattice. The first two sections follow partially the references [21, 50–52], whereas the strain part follows partially the references [53, 54].[1]

---

[1] The sketch showing non-uniformly strained graphene was adapted from Ref. [44].

2.1. Basics of graphene

Graphene is a single two-dimensional (2D) sheet of carbon atoms arranged in a hexagonal structure as shown in Fig. 2.1(a). Each carbon atom has six electrons with a configuration of $1s^2\ 2s^2\ 2p^2$. In graphene, the $2s$ orbital hybridizes with the $2p_\mathrm{x}$ and $2p_\mathrm{y}$ orbitals to form three sp^2 orbitals with a trigonal planar structure, while the remaining $2p_\mathrm{z}$ orbital stays perpendicular to this plane. The two core electrons in the $1s$ orbital are inert and do not form any chemical bonds. Three of the four valence electrons occupy the sp^2 orbitals forming a localized σ-bond between carbon atoms. The σ-band is responsible for the robustness of the lattice. The last valence electrons occupy the $2p_\mathrm{z}$ orbitals forming the delocalized π-bonds among the carbon atoms, leading to the formation of a half-filled π-band which determines the low energy electronic states in graphene. In the following a tight-binding model based on nearest-neighbor hoping will be used to derive the low energy spectrum of graphene.

2.1.1. From lattice structure to band structure

The primitive unit cell of graphene has two atoms (A and B), which is spanned by the two lattice vectors

$$\vec{a}_1 = \frac{a_0}{2}\begin{pmatrix} 3 \\ \sqrt{3} \end{pmatrix} \qquad \text{and} \qquad \vec{a}_2 = \frac{a_0}{2}\begin{pmatrix} 3 \\ -\sqrt{3} \end{pmatrix} \tag{2.1}$$

to form the hexagonal lattice, which can be seen as two sublattices A and B. Here, $a_0 = 1.42$ Å is the inter-atomic distance. Each A atom directly neighbors three B atoms and vice versa, as depicted in Fig. 2.1(a). The nearest-neighbors in real space are connected by vectors

$$\vec{d}_1 = a_0\begin{pmatrix} 1 \\ 0 \end{pmatrix} \qquad \text{and} \quad \vec{d}_2 = \frac{a_0}{2}\begin{pmatrix} -1 \\ -\sqrt{3} \end{pmatrix} \qquad \text{and} \qquad \vec{d}_3 = \frac{a_0}{2}\begin{pmatrix} -1 \\ \sqrt{3} \end{pmatrix}. \tag{2.2}$$

The reciprocal lattice is shown in Fig. 2.1(b) with the hexagon being the first Brillouin zone. The two reciprocal lattice vectors are given by

$$\vec{b}_1 = \frac{2\pi}{3a_0}\begin{pmatrix} 1 \\ \sqrt{3} \end{pmatrix} \qquad \text{and} \qquad \vec{b}_2 = \frac{2\pi}{3a_0}\begin{pmatrix} 1 \\ -\sqrt{3} \end{pmatrix}, \tag{2.3}$$

which are obtained by the relation $\vec{a_\mathrm{i}}\vec{b_\mathrm{j}} = 2\pi\delta_\mathrm{ij}$.

In a tight-binding model, the electrons are assumed to be well localized in atomic orbitals at the site of each atom, but are allowed to hop between neighboring atoms. Usually only the nearest neighbor hopping is considered, which describes the physics accurate enough in most cases. Next-nearest neighbor hopping and higher terms will lead to a correction of the band structure at

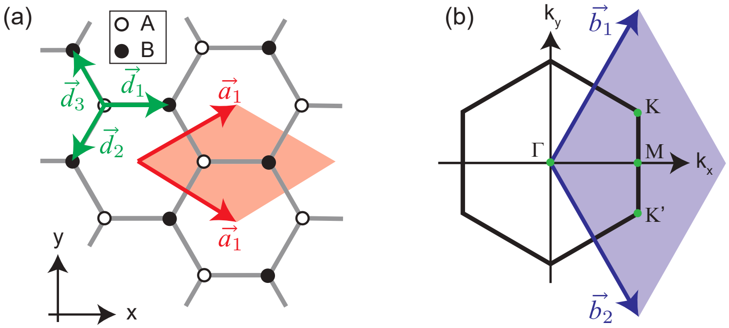

Figure 2.1. Graphene lattice in real and reciprocal space. (a) The unit cell (shaded in red) of graphene containing two atoms (A and B) is spanned by the two lattice vectors $\vec{a_1}$ and $\vec{a_2}$ in real space. **(b)** The first Brillouin zone shown as hexagon is spanned by the two reciprocal lattice vectors $\vec{b_1}$ and $\vec{b_2}$. The two inequivalent sets of valleys K and K' sit at the six corners of the Brillouin zone. Figure adapted from Ref. [55].

high energies and are often neglected. As mentioned above, the low energy electronic states are determined by electrons in the $2p_z$ orbitals. We therefore take the two $2p_z$ orbitals, $|\phi_\mathrm{A}\rangle$ for A atom and $|\phi_\mathrm{B}\rangle$ for B atom, in the unit cell to construct the Bloch functions for the tight-binding calculation. The Bloch functions depend on the position vector $\vec{r}$ and the wave vector $\vec{q}$ and are given by

$$\psi_{\mathrm{A(B)}}(\vec{r}) = \frac{1}{\sqrt{N}} \sum_{\vec{R}_{\mathrm{A(B)}}} e^{i\vec{q}\vec{R}_{\mathrm{A(B)}}} \phi_{\mathrm{A(B)}}(\vec{r} - \vec{R}_{\mathrm{A(B)}}), \tag{2.4}$$

where the sum is over N different unit cells and $\vec{R}_{\mathrm{A(B)}}$ denotes the location of the atoms. Due to the two sublattices, the Hamiltonian takes the form

$$H = \begin{pmatrix} H_{\mathrm{AA}} & H_{\mathrm{AB}} \\ H_{\mathrm{BA}} & H_{\mathrm{BB}} \end{pmatrix} . \tag{2.5}$$

The diagonal terms are given by

$$H_{\mathrm{AA(BB)}} = \langle \psi_{\mathrm{A(B)}}(\vec{r}) | \, H \, | \psi_{\mathrm{A(B)}}(\vec{r}) \rangle \, , \tag{2.6}$$

yielding $H_{\mathrm{AA}} = H_{\mathrm{BB}} = \epsilon$ with ϵ being the on-site energy which is usually set to zero without loss of generality. The off-diagonal terms are calculated with

$$H_{\mathrm{AB(BA)}} = \langle \psi_{\mathrm{A(B)}}(\vec{r}) | \, H \, | \psi_{\mathrm{B(A)}}(\vec{r}) \rangle \, , \tag{2.7}$$

yielding

$$H_{\mathrm{AB}} = H_{\mathrm{BA}}^* = t \cdot \left(e^{i\vec{q}\vec{d}_1} + e^{i\vec{q}\vec{d}_2} + e^{i\vec{q}\vec{d}_3} \right) = t \cdot f(\vec{q}) \tag{2.8}$$

with $t = \langle \phi_{\mathrm{A}}(\vec{r}) | H | \phi_{\mathrm{B}}(\vec{r}) \rangle \approx -2.7\,\mathrm{eV}$ being the nearest neighbor hopping energy [21]. The Hamiltonian can then be written as

$$H = t \cdot \begin{pmatrix} 0 & f(\vec{q}) \\ f(\vec{q})^* & 0 \end{pmatrix} . \tag{2.9}$$

The eigenvalues readily come out as $E_{\pm} = \pm|t|\sqrt{|f(\vec{q})|^2}$, where the ±-sign accounts for the conduction and valence band. An explicit expression can be written as

$$E_{\pm}(\vec{q}) = \pm t \sqrt{1 + 4\cos\left(\frac{3}{2} q_{\mathrm{x}} a_0\right) \cos\left(\frac{\sqrt{3}}{2} q_{\mathrm{y}} a_0\right) + 4\cos^2\left(\frac{\sqrt{3}}{2} q_{\mathrm{y}} a_0\right)} \tag{2.10}$$

by plugging in the nearest neighbour vectors from Eq. 2.2. This function is plotted in Fig. 2.2(a) for the first Brillouin zone[2], capturing the electronic band structure of graphene. In pristine graphene, the Fermi level lies at zero energy.

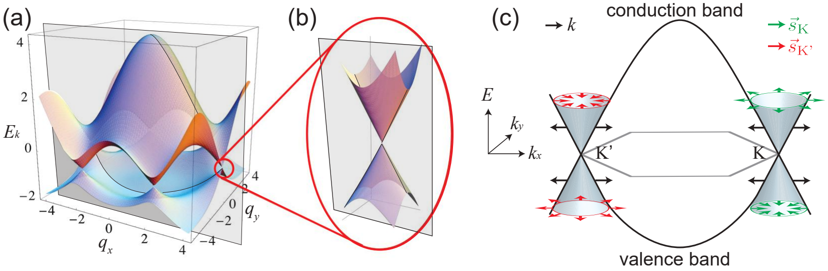

Figure 2.2. Band structure of graphene. **(a)** Energy spectrum (in units of t) for $t = -2.7\,\mathrm{eV}$ and the next-nearest neighbor hopping $t' = 0.2\,\mathrm{t}$. Figure adapted from Ref. [21]. **(b)** Low-energy spectrum in the vicinity of one Dirac point. **(c)** Cut for $q_{\mathrm{y}} = 0$ as indicated with the grey plane in **(a)** and **(b)**. The orientation of the pseudospin ($\vec{s}_{\mathrm{K,K'}}$) is parallel (anti-parallel) to $\vec{k}$ for the $K(K')$ valley in the conduction band. In the valence band the opposite chirality is found. Figure adapted from Ref. [55]

---

[2] Next-nearest neighbor hopping is included for calculating Fig. 2.2 which leads to an asymmetric valence and conduction band.

Valley degree of freedom

The conduction band touches the valence band at the six corners of the first Brillouin zone. Therefore, graphene has a zero band gap, which distinguishes it from conventional semiconductors and metals. The touching points are the so-called Dirac points, which are divided into two sets (K and K') because they cannot be connected with a reciprocal lattice vector. Therefore the Fermi surface of graphene has two inequivalent cones located at the two different Dirac points, giving the charge carriers in graphene an additional degree of freedom. This degeneracy is referred to as the valley degree of freedom. The K and K' points of the Brillouin zone are located at the positions

$$\vec{K} = \frac{2\pi}{3a_0}\begin{pmatrix}1\\ 1/\sqrt{3}\end{pmatrix} \qquad \text{and} \qquad \vec{K}' = \frac{2\pi}{3a_0}\begin{pmatrix}1\\ -1/\sqrt{3}\end{pmatrix}, \tag{2.11}$$

respectively. Since the two valleys are well separated in k-space, intervalley scattering is strongly suppressed, making valley a good quantum number in graphene.

Linear dispersion

The dispersion relation can be expanded around the K point for low energies with $\vec{q} = \vec{K} + \vec{k}$, where $|\vec{k}| \ll |\vec{K}|$ is the quasi-momentum measured from the K point. Similar expansion can be done for the K' point. A Taylor expansion of Eq. 2.10 around $\vec{K}$ yields a linear dispersion relation:

$$E_{\pm}(\vec{k}) = \pm\hbar v_{\mathrm{F}}|\vec{k}|, \tag{2.12}$$

with $\hbar$ the reduced Planck constant and $v_{\mathrm{F}} = 3ta_0/(2\hbar) \approx 1 \times 10^6\,\mathrm{m\,s^{-1}}$ the Fermi velocity. The + (-) accounts for the conduction (valence) band. The linearized Hamiltonian for both valleys can be written as

$$H_0 = \hbar v_{\mathrm{F}}(\kappa k_{\mathrm{x}}\hat{\sigma}_{\mathrm{x}} - k_{\mathrm{y}}\hat{\sigma}_{\mathrm{y}}) \tag{2.13}$$

with $\kappa = +(-)$ for the K (K') valley and $\hat{\sigma}_{\mathrm{i}}$ the Pauli matrices acting on the sublattice space. This Hamiltonian has the form of the Dirac equation. Therefore, charge carriers in graphene are often described as “massless” Dirac Fermions with velocity v_{F}.

Density of states

As discussed above, charge carriers in graphene have valley degeneracy in addition to the normal spin degeneracy. Since the dispersion relation is linear in $\vec{k}$, the density of states (DoS) in graphene depends linearly on energy, given by

$$DoS(E) = \frac{g_{\mathrm{s}}g_{\mathrm{v}}E}{2\pi(\hbar v_{\mathrm{F}})^2}, \tag{2.14}$$

where $g_s = g_v = 2$ are the degeneracies due to spin and valley. This energy dependent DoS is in stark contrast to that of conventional 2D semiconductors which have a constant DoS due to the parabolic dispersion relation. With the relation $|\vec{k}| = k_F = \sqrt{\pi n}$, one can write the Fermi energy of graphene as a function of carrier density:

$$E(n) = \hbar v_{\mathrm{F}} \sqrt{\frac{4\pi n}{g_s g_v}}. \tag{2.15}$$

2.1.2. Pseudospin and Berry-phase

Due to the presence of A and B sublattices, the charge carriers in graphene have an additional quantum number, called pseudospin, in analogy to a real spin. It describes the relative contribution of the two orbital wave functions, $|\phi_{\mathrm{A}}\rangle$ and $|\phi_{\mathrm{B}}\rangle$, to the total wave function. Using $k_{\mathrm{x}} + ik_{\mathrm{y}} = ke^{i\theta}$ with $\theta = \arctan(k_{\mathrm{y}}/k_{\mathrm{x}})$, Eq. 2.13 can be rewritten as

$$H = \hbar v_{\mathrm{F}} k \begin{pmatrix} 0 & \pm e^{\mp i\theta} \\ \pm e^{\pm i\theta} & 0 \end{pmatrix}, \tag{2.16}$$

where the ±-sign accounts for the solution around the K and K' valley. The eigenvectors of Eq. 2.16 are given for the conduction ($|EV_{\mathrm{C}}\rangle$) and valence band ($|EV_{\mathrm{V}}\rangle$) as

$$|EV_{\mathrm{C}}\rangle = \frac{1}{\sqrt{2}} \begin{pmatrix} e^{\mp i\theta/2} \\ e^{\pm i\theta/2} \end{pmatrix} \qquad \text{and} \qquad |EV_{\mathrm{V}}\rangle = \frac{1}{\sqrt{2}} \begin{pmatrix} e^{\mp i\theta/2} \\ -e^{\pm i\theta/2} \end{pmatrix}, \tag{2.17}$$

with ±-sign accounting for the K and K' valley. In a more compact way, the eigenvectors can be written as

$$|\mathbf{s}\rangle = \frac{1}{\sqrt{2}} \begin{pmatrix} e^{\mp i\theta/2} \\ s e^{\pm i\theta/2} \end{pmatrix}, \tag{2.18}$$

where $s = +(-)$ accounts for the conduction (valence) band. The probability of finding the wave function on sublattice A or B is given by the absolute square of the two components of the vector in Eq. 2.18. Similar to a real spin, this vector can be viewed as the result of a spin-1/2 rotation operator $R(\theta)$ acting on the initial state $|\mathbf{s}_0\rangle$ pointing along the x-direction:

$$|\mathbf{s}\rangle = R(\theta)|\mathbf{s}_0\rangle = \left(\begin{array}{cc} e^{\mp i\theta/2} & 0 \\ 0 & e^{\pm i\theta/2} \end{array} \right) \left(\begin{array}{c} 1/\sqrt{2} \\ s/\sqrt{2} \end{array} \right) \tag{2.19}$$

For a 2π rotation, which is equivalent to a charge carrier encircling the K or K' point, the wave function picks up a phase of π. This phase is the so-called Berry phase.

As shown in Fig. 2.2(c), the pseudospin is parallel (anti-parallel) to $\vec{k}$ in the conduction (valence) band for the K valley, while it is the opposite for the K' valley. A relevant quantity used to characterize the eigenvectors is the chirality, which is defined as the projection of the pseudospin onto the momentum. At low energies, the chirality is conserved. Therefore, backscattering within one valley is not allowed because this would require to change the chirality of the charge carrier. Backscattering would then need to involve the other valley, which requires a momentum change on the order of $\sim \vec{K} \sim 1/a_0$. Such a large momentum change can only be provided by scattering at short-range disorders, such as edges or atomic defects.

2.1.3. Bilayer graphene

Bilayer graphene (BLG) can be seen as two monolayer graphene (MLG) stacked on top of each other. The most common stacking order is the AB stacking, where the A atom of the top layer sits directly above the B atom of the bottom layer. The lattice of an AB stacked BLG is shown in Fig. 2.3(a) with the most relevant hopping terms γ_i indicated. The intralayer hopping between A1 (A2) and B1 (B2) in the bottom (top) layer corresponds to the nearest neighbor hopping in MLG and therefore $\gamma_0 = t = -2.7\,\mathrm{eV}$. All other hopping terms are interlayer and describe the coupling between the two layers with $\gamma_1 = -0.4\,\mathrm{eV}$ connecting the B1 and the A2 atoms, $\gamma_3 = -0.3\,\mathrm{eV}$ connecting the A1 and the B2 atoms, and $\gamma_4 = -0.04\,\mathrm{eV}$ connecting the B1 and the B2 atoms [56].

The tight-binding model can be adapted to derive the electronic structure of BLG as well. Considering only γ_0 and γ_1, the low energy electronic structure of BLG is described by the following energy dispersion relation:

$$E_\pm^\alpha = \pm\left[V^2 + \hbar^2 v_\mathrm{F}^2 \vec{k}^2 + \frac{\gamma_1^2}{2} + (-1)^\alpha \sqrt{4V^2\hbar^2 v_\mathrm{F}^2 \vec{k}^2 + \gamma_0 \hbar^2 v_\mathrm{F}^2 \vec{k}^2 + \frac{\gamma_1^4}{2}}\right], \tag{2.20}$$

where + (-) accounts for the conduction (valence) band, $v_\mathrm{F} = 1 \times 10^6\,\mathrm{m\,s^{-1}}$ is the Fermi velocity of MLG and V describes a possible difference of the electrochemical potential between the two layers, which can, for example, be tuned by an external perpendicular electric field [50]. The parameter α is used for describing the two subbands in the conduction and valence band, which are shifted away from zero energy by γ_1 in the case of $V = 0$. For $V = 0$, Eq. 2.20 can be simplified to:

$$E_\pm^\alpha = (-1)^\alpha \cdot \frac{\gamma_1}{2} \pm \frac{\gamma_1}{2}\sqrt{1 + (\vec{k}/k_0)^2}. \tag{2.21}$$

where $k_0 = \gamma_1/(2\hbar v_\mathrm{F})$ is a characteristic wave vector. For small $\vec{k}$ ($|\vec{k}| \ll k_0$), Eq. 2.21 describes a parabolic dispersion relation with an effective mass

$m^* = \gamma_1/(2v_{\mathrm{F}}^2) \sim 0.03m_e$, where m_e is the free electron mass. For large $\vec{k}$ ($|\vec{k}| \gg k_0$), the dispersion relation becomes linear. The turning point is around a charge carrier density of $5 \times 10^{12}\,\mathrm{cm}^{-2}$. At low energies, the DoS of BLG is independent of energy due to the parabolic dispersion relation [50]:

$$DoS(E) = \frac{4m^*}{2\pi\hbar^2}, \tag{2.22}$$

where the factor 4 accounts for the spin and valley degeneracy.

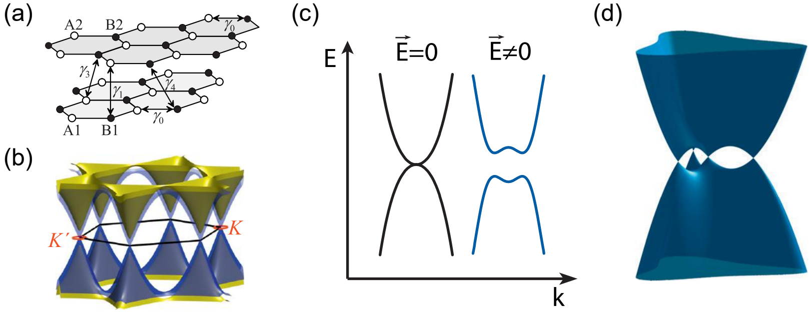

Figure 2.3. Band structure of bilayer graphene. (a) The lattice of an AB stacked bilayer graphene shown in real space with all relevant hopping terms indicated by γ_{i}. Figure adapted from Ref. [50]. **(b)** Electronic structure of bilayer graphene shown on an energy scale of 3 eV measured from the Dirac point. The black hexagon represents the first Brillouin zone. The blue (yellow) surfaces show the low-energy (split) bands. The K and K' valleys are indicated with red circles. Figure adapted from Ref. [57]. **(c)** Band structure around the K point with and without a perpendicular electric field. A finite gap opens up with electric field. The trigonal warping is not taken into account. Figure adapted from Ref. [19]. **(d)** Low energy spectrum at the K valley including trigonal warping. Figure adapted from Ref. [57].

In Fig. 2.3(b) the band structure of BLG is shown with the two split bands represented by two colored surfaces. The gap opened by an external perpendicular electric field is schematically shown in Fig. 2.3(c). When the other interlayer hopping terms γ_3 and γ_4 are included, the topology of the band structure at low energy changes from a parabola to four mini Dirac cones, as shown in Fig. 2.3(d) [57]. As it deforms the band structure into a trigonal shape, this effect is usually called trigonal warping. For pristine BLG, the transition of the Fermi surface from a single circle to four disconnected circles happens at an energy ∼1 meV. This transition is called the Lifshitz transition. The charge carriers in BLG are also chiral and the chirality is opposite for the two valleys, the same as in MLG. However, the Berry phase is 2π [50, 58], different to that in MLG.

2.2. Charge transport in graphene

Since the experiments presented later in this thesis focus mostly on electron transport in graphene, it is helpful to introduce the relevant transport concepts first. In this section we first define some length scales, followed by an introduction to the field effect and some basic quantities which characterize the device quality, such as mobility and residual doping. Second, different transport regimes and corresponding effects are discussed. Furthermore, the quantum Hall effect in graphene is introduced.

For a rectangular 2D conductor, the system size is defined by the device width W and the device length L. One important length scale is the mean free path l_{mfp}, which is the distance the charge carriers can travel between two momentum scattering events. Another relevant length scale is the phase coherence length l_{ϕ}, which is defined as the distance the charge carriers travel before their phases are randomized. The length scales can also be expressed in their corresponding time scales: momentum relaxation time τ and phase coherence time τ_{ϕ}.

Different transport regimes can occur depending on the ratio of the characteristic length scales to the device size. If $l_{\mathrm{mfp}} \ll W, L$, which is called the diffusive regime, many scattering events happen when the charge carriers travel through the device and their momenta are fully randomized. On the other hand, if $l_{\mathrm{mfp}} \sim W, L$, the ballistic regime occurs. Similarly, the phase coherent transport regime is entered when $l_{\phi} \sim W, L$. Several transport regimes and corresponding phenomena are introduced later.

2.2.1. Field effect

A typical device investigated in this thesis has two electrodes (source and drain) and a global back gate. In transport experiments, usually a small voltage V_{SD} is applied between the source and drain electrodes, inducing a current I_{SD} in the device which can be measured. The conductance is then calculated with $G = I_{\mathrm{SD}}/V_{\mathrm{SD}}$. For graphene devices, the conductance can be tuned by varying the charge carrier density, which can be realized by applying a finite voltage difference between the graphene channel and the gate electrode. In most cases, the induced charge carrier density is very well estimated by the plate capacitor model with a gate capacitance of

$$C = \epsilon_0 \epsilon_{\mathrm{r}} \frac{A}{d}, \tag{2.23}$$

where A is the device area, d is the thickness of the dielectric and ϵ_r is the relative dielectric constant. The induced density leads to a shift of the Fermi level in graphene, which can be tuned into both the electron and the hole band due to the zero-gap of graphene, as shown in Fig. 2.4. Theoretically the Fermi level can be tuned to the Dirac point in graphene, however, potential fluctuations, which cannot be screened at low carrier densities, prevent this in real devices. The device breaks into random electron-hole puddles near the Dirac point instead of having a homogeneous carrier density. Therefore, the Dirac point is often referred to as charge neutrality point (CNP). The residual doping n_0, which is the lowest homogeneous carrier density that can be realized in a device, characterizes the device quality in terms of how close the Fermi level can be tuned to the Dirac point.

2.2.2. Diffusive regime and Drude model

In the diffusive regime, the conductivity based on the classical Drude model is given as

$$\sigma = \frac{ne^2\tau}{m}, \tag{2.24}$$

where τ is the average time between two momentum scattering events. Using $m = |\vec{p}|/v_\mathrm{F} = \hbar k_\mathrm{F}/v_\mathrm{F}$ as the charge carrier mass for graphene, the following equation arises:

$$\sigma = \frac{2e^2\tau v_\mathrm{F}\sqrt{\pi n}}{h}, \tag{2.25}$$

Usually, the two dominant scattering sources are charged impurities [59–65] and random strain fluctuations [66, 67]. Both scattering mechanisms give a $\tau \propto k_\mathrm{F}$ relation, yielding a linear dependence of the conductivity on carrier density:

$$\sigma \sim ne\mu, \tag{2.26}$$

with a carrier density independent mobility μ.

In Fig. 2.4 a typical plot of the conductance versus carrier density of a two-terminal device is shown. In a two-terminal configuration, the graphene resistance is measured in series with the contact resistance R_C (including line resistance of the measurement circuit). The conductance starts to saturate at higher gate voltages because the contact resistance starts to dominate. The slight asymmetry between the electron (n-doped) and hole (p-doped) side originates from the formation of a *p*-*n* junction near the contact due to contact doping. The conductance is related to the conductivity by $\sigma = \alpha G$ with a geometry factor α, which is the aspect-ratio (L/W) for rectangular devices. Taking the contact resistance into account, the conductance of a two-terminal

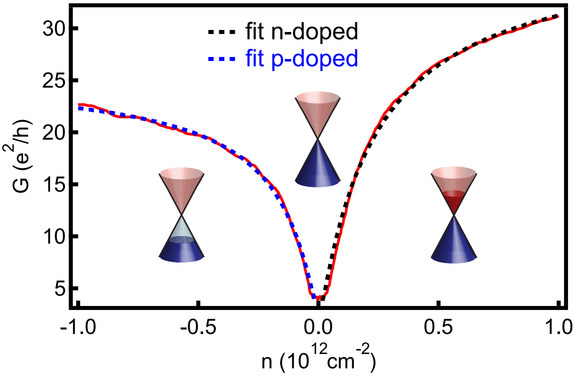

Figure 2.4. Field effect in graphene: Carrier density dependence of the graphene conductance showing ambipolar field effect. Red solid line represents the data and dashed lines are the fits. Different doping levels are shown schematically with the insets. Fitting with equation 2.27 yielding $\mu \approx 54\,000\,\mathrm{cm^2V^{-1}s^{-1}}$ for both sides and $n_0 \approx 2 \times 10^{10}\,\mathrm{cm^{-2}}$.

device as a function of carrier density is given by

$$G = \frac{1}{\frac{\alpha}{e\mu\sqrt{n^2+n_0^2}} + R_\mathrm{c}}, \tag{2.27}$$

where n_0 is the residual doping. Therefore, Eq. 2.27 can be used to extract the mobility and residual doping by fitting the conductance curve as shown in Fig. 2.4.

2.2.3. Ballistic transport

The mean free path of the charge carriers is given by $l_\mathrm{mfp} = v_\mathrm{F}\tau$. Using Eq. 2.25 and Eq. 2.26, l_mfp can be written as

$$l_\mathrm{mfp} = \frac{\hbar}{e}\mu\sqrt{n\pi}. \tag{2.28}$$

For high mobility samples, l_mfp can approach the size of the device and the system becomes ballistic. Since in this regime scattering only happens at the edges and the contacts, the diffusive formulas mentioned above start to fail. The conductance is then given by the number of modes and each of them carries a conductance of $4e^2/h$ due to spin and valley degeneracy. The number of modes is determined by the width W of the graphene channel and the total conductance is given by [68]

$$G = \frac{4e^2}{h}\frac{W}{\lambda_\mathrm{F}/2} = \frac{4e^2}{h}W\sqrt{n/\pi}, \tag{2.29}$$

with $\lambda_\mathrm{F} = 2\pi/k_F$.

Many interesting phenomena can be observed in ballistic regime, such as transverse magnetic focusing (TMF) [69, 70], Fabry-Pérot resonances [71, 72] and snake states [71, 73]. In the following we discuss the TMF in more detail.

Transverse magnetic focusing

When graphene is subject to an out-of-plane magnetic field, the charge carriers will undergo a cyclotron motion with a radius of

$$r_\mathrm{c} = \frac{\hbar\sqrt{\pi n}}{eB}. \tag{2.30}$$

In the ballistic regime, such cyclotron motion allows one to focus the charge carriers, which is known as the transverse magnetic focusing. An illustration of TMF in a hBN/graphene/hBN heterostructure is shown in Fig. 2.5(a), where the measurement configuration is sketched with the bottom-left and -right contacts as the injector and collector, respectively.

Whenever the condition $d = i{\cdot}2r_\mathrm{c}$ is fulfilled, where d is the distance between the injector and the collector and i is an integer, a non-local signal is detected as $R_\mathrm{NL} = V_\mathrm{c}/I_\mathrm{i}$. The measurement is shown in Fig. 2.5(b), where the dashed lines are the expected signal maxima calculated according to Eq. 2.30 for $i = 1, 2, 3$. The observation of higher-order TMF signals ($i = 2, 3, 4...$) implies specular reflection at the graphene edge, which only occurs when the graphene edge is smooth on the order of the Fermi wavelength λ_F. Therefore, TMF can be used as a tool to characterize the edge quality of the sample [74]. Effects which are determined only by ballistic transport, such as TMF or snake states, can survive up to ~100 K [69, 70, 73], because the mechanisms suppressing the ballistic transport, such as phonon scattering and electron-electron scattering [70], are strongly reduced below these temperatures.

2.2.4. Phase coherent transport

If the phase coherence length l_ϕ is comparable to the device size, the quantum mechanical phase of the charge carriers is preserved during transport and the system enters the phase coherent regime. Effects due to interference, such as universal conductance fluctuations (UCF) and weak localization (WL), arise in this regime. In the following we give a short introduction to both effects.

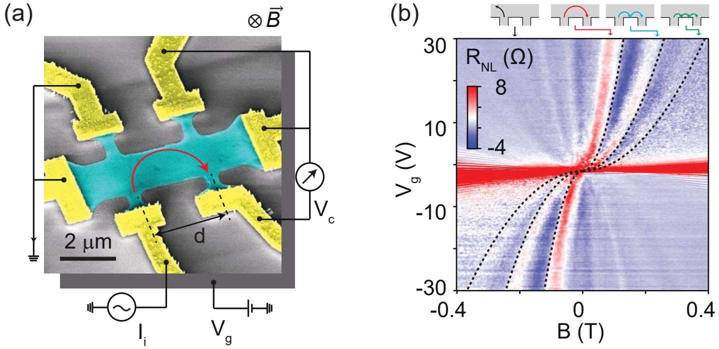

Figure 2.5. Transverse magnetic focusing. (a) False-colored SEM image of a typical device for TMF measurements. The hBN-encapsulated graphene is colored in cyan and the metal contacts in yellow. In the presence of an out-of-plane magnetic-field, charge carriers perform a cyclotron motion as indicated with the red arrow. **(b)** Non-local resistance as a function of gate voltage V_g and magnetic field B. Black-dashed lines are the first three expected TMF features calculated according to Eq. 2.30. Figure adapted from Ref. [55]

Universal conductance fluctuations

In a diffusive conductor, the charge carriers can travel through different paths, which interfere with each other due to the coherent phase. These constructive and destructive interferences result in a deviation of the conductance from the classically expected value. If $l_\phi \sim L, W$, the amplitude of the conductance fluctuations is of the order of the conductance quantum e^2/h and is independent of the device size and the strength of the disorder [52, 75], which made people call the fluctuations *universal*.

The interference pattern can be tuned by both the path length and the wavelength. One way to modify the paths of the charge carriers is to apply a perpendicular magnetic field, which bends the trajectories of the charge carriers. The charge carrier wavelength λ_F can be changed by changing the Fermi level with an electric gate. In addition, gating also modifies the charge carrier paths by changing the disorder potential. These allow one to tune the conductance fluctuations by varying the magnetic field or the gate voltage.

When the phase coherence length is smaller than the device dimensions, the overall UCF amplitude reduces, as it can be seen as an average of fluctuations over several independent regions with size $\sim l_\phi^2$. Therefore, the UCF can be suppressed by reducing l_ϕ (e.g. by increasing temperature). Furthermore, an ensemble averaging over different densities or magnetic fields can also be used to reduce the UCF amplitude.

If phase coherent transport occurs in the ballistic regime, interference can only happen at the edge or electrostatic defined boundaries. In this case, effects such as Fabry-Pérot resonances arise [71, 72].

Weak localization

Charge carrier trajectories can form closed loops after several scattering events in a diffusive system, as shown schematically in Fig. 2.6. The forward (solid lines) and the reversed paths (dashed lines) are identical in possibility and are related to each other by time-reversal symmetry. If we use A^+ and A^- to denote the complex quantum mechanical amplitudes of the two paths, the probability of returning to the starting point is given by

$$|A^+ + A^-|^2 = |A^+|^2 + |A^-|^2 + A^+A^{-*} + A^{+*}A^- . \tag{2.31}$$

The first two terms on the right-hand side describe the classical contributions to backscattering, which are captured in the Drude formalism presented in section 2.2.2. The last two terms arise from the interference of the two paths which are neglected in the incoherent approximation of Drude formalism. At zero magnetic field, $A^+ = A^- \equiv A$ is required by time-reversal symmetry. The classical return probability is then given by

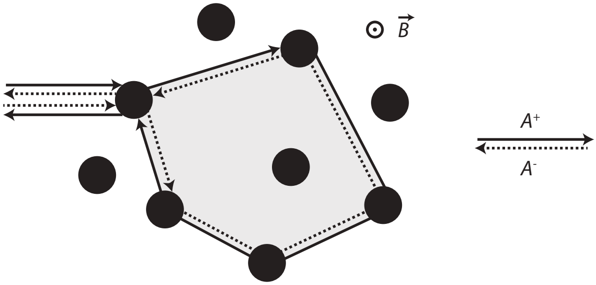

Figure 2.6. Schematics of weak localization. Time-reversed loops due to multiple scattering events. At zero magnetic field, the interference of the forward and the reversed paths is always constructive, leading to an enhanced backscattering probability. A finite magnetic field $\vec{B}$ applied through the loop area (grey shaded region) changes the interference condition and suppresses the backscattering probability. Figure adapted from Ref. [76]

$$P_{\text{cl}} = 2|A|^2, \tag{2.32}$$

while the quantum mechanical return probability is doubled due to the interference terms and is given by

$$P_{\mathrm{qm}} = 4|A|^2. \tag{2.33}$$

This correction due to quantum interference is called weak localization [52].

In the presence of an out-of-plane magnetic field, the wave function will pick up an Aharonov-Bohm phase

$$\phi_{\mathrm{AB}} = 2\pi \frac{BS}{h/e} \tag{2.34}$$

with opposite signs for the two paths upon returning to the starting point. Here, S is the loop area. The quantum mechanical amplitudes therefore become magnetic field dependent, $A^{\pm}(B) = Ae^{\pm i\phi_{\mathrm{AB}}}$, leading to

$$P_{\mathrm{qm}} = 2|A|^2 + 2|A|^2 \cos\left(4\pi \frac{BS}{h/e}\right), \tag{2.35}$$

which is periodic in magnetic field. Since many pairs of time-reversed paths enclosing different areas will occur in a macroscopic diffusive device, the oscillatory contribution of individual time-reversed paths averages out completely at finite magnetic fields. At zero field, however, the cosine function has its maximum for all these oscillations and therefore the backscattering is at its maximum, yielding a minimum in the conductance. As a result, WL can be suppressed by magnetic filed leading to an increase of the conductance.

2.2.5. Quantum Hall effect in graphene

In the presence of a magnetic field, charge carriers experience a Lorentz force and undergo cyclotron motion. In a conductor, when a magnetic field is applied perpendicular to the direction of current flow, a voltage normal to the plane of the magnetic field and the current flow appears [77], which is now commonly called the classical Hall effect. In a 2D system, the Hall voltage is given by [52] $V_{\mathrm{H}} = IB/(en)$, where I is the applied current. This makes the Hall effect a way to measure the charge carrier density in a 2D conductor, e.g. graphene.

The cyclotron radius is inversely proportional to the applied magnetic field, as given in Eq. 2.30 for graphene. For very large magnetic fields the charge carriers can complete a full cyclotron orbit within the sample and quantum effects start to play a role. In this case, the longitudinal resistance R_{xx} drops to zero, whereas the Hall resistance R_{xy} becomes quantized. This effect is the so-called quantum Hall effect (QHE). It was first realized with a 2D electron gas in a silicon metal-oxide-semiconductor field-effect transistor at low temperature [78, 79], where $R_{\mathrm{xy}} = h/(e^2\nu)$ was observed with ν being an integer. The quantum Hall effect can be understood with dissipationless edge channels carrying the current while the bulk of the sample is gapped, which results in the quantized Hall conductance. Two main conditions are required for observing the quantum Hall effect. First, the magnetic filed should be large enough so that the charge carriers can perform full cyclotron motion without being scattered. Second, the temperature must be low enough such that the thermal energy scale $k_\mathrm{B}T$ is smaller than the Landau level (LL) spacing.

For graphene, solving the Dirac equation in a perpendicular magnetic field one obtains the LL energies as

$$E_\mathrm{N} = \mathrm{sign}(N) v_\mathrm{F} \sqrt{2e\hbar B|N|}, \tag{2.36}$$

with N being the LL index. The LLs have non-equidistant spacing (in contrast to conventional semiconductors) due to the square-root dependence on B. The zeroth LL is at zero energy, containing half electrons and half holes. The largest LL spacing is between the first two LLs, which is so large that QHE is observed even at room temperature [80]. The quantum Hall conductance of graphene takes the form

$$G_\mathrm{xy} = \frac{g_\mathrm{s} g_\mathrm{v} e^2}{h}(N + 1/2), \tag{2.37}$$

with $g_\mathrm{s} = g_\mathrm{v} = 2$ being the spin and valley degeneracy. The shift of 1/2 comes from the Berry phase picked up by closed loops. In very clean samples, the spin and valley degeneracy can be lifted due to electron-electron interactions, leading to the observation of quantized conductance at all integer values of e^2/h [81].

The quantum Hall effect is usually measured in a six-terminal device, commonly referred to as a Hall-bar. In this thesis, most investigated devices have only two terminals, where the R_xx and G_xy cannot be measured independently. Instead, a combination of both components is measured, but well defined plateaus with values given in Eq. 2.37 can still be observed for devices with an aspect ration of $W/L \sim 1$ [82, 83].

For BLG, the LL energy is given by [84]

$$E_N = \pm\hbar\omega\sqrt{N(N-1)}, \tag{2.38}$$

which is nearly equidistant due to the approximately parabolic dispersion at low energies, as introduced in section 2.1.3. The LLs are fourfold degenerate due to spin and valley degeneracy except for $N = 0$ and $N = 1$. As can be seen from Eq. 2.38, both the $N = 0$ and $N = 1$ LLs lie at zero energy, which leads to an eightfold degeneracy. The same as in MLG, this LL contains half electrons and half holes. The usual quantum Hall conductance in BLG has values of $\pm 4, \pm 8, \pm 12...$ in unit of e^2/h [84].

2.3. Strain in graphene

The large mechanical strength of graphene allows one to modify its electronic properties by externally induced strain fields [7, 43], which has been extensively discussed theoretically [43, 85–90]. In this section, the main strain effects in graphene are discussed, followed by a brief introduction to strain characterization with Raman spectroscopy.

2.3.1. Strain effects on electronic properties

An intuitive way to understand the strain effects in graphene is to look at the strain induced perturbations to the Dirac cones shown in Fig. 2.2. Strain induced scalar potential can be understood as the up/down shift of the Dirac cones in energy, while the vector potential/pseudomagnetic field originates from the in-plane displacement of the Dirac cones in momentum. The slope of the Dirac cones can also be modified by strain, that is the Fermi velocity renormalization. In the following, we discuss the above effects one by one.

The unstrained graphene lattice is illustrated in Fig. 2.7(a) with the bond vectors denoted $\vec{d}_\mathrm{j}$, where $j = 1, 2, 3$ and $|\vec{d}_\mathrm{j}| = a_0$, as given in Eq. 2.2. Strain induced lattice deformations can be seen as relative displacement of the atoms. Assuming the center atom is fixed, the displacement of the three neighboring atoms are described with the displacement vectors $\vec{u}_\mathrm{j}$, which results in a set of new bond vectors $\vec{d}'_\mathrm{j} = \vec{d}_\mathrm{j} + \vec{u}_\mathrm{j}$, as depicted in Fig. 2.7(b). The change in bond

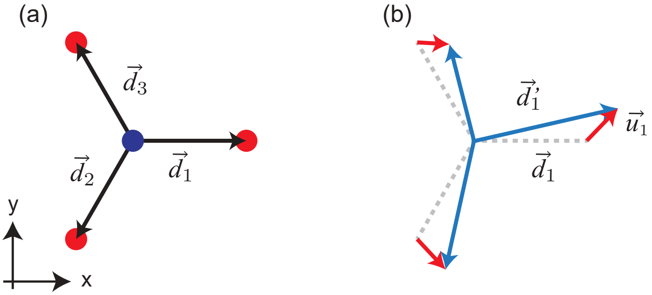

Figure 2.7. Lattice distortion. (a) Illustration of a carbon atom with its three nearest neighbors for unstrained graphene. The bond vectors are denoted $\vec{d}_\mathrm{j}$. **(b)** Illustration of distorted graphene lattice, with distorted bond vectors denoted $\vec{d}'_\mathrm{j}$ and atom displacement vectors denoted $\vec{u}_\mathrm{j}$. Figure adapted from Ref. [53].

length is approximated as

$$\Delta d = |\vec{d}_{\mathrm{j}}'| - |\vec{d}_{\mathrm{j}}| \approx \vec{u}_{\mathrm{j}} \cdot \frac{\vec{d}_{\mathrm{j}}}{a_0}. \tag{2.39}$$

In the continuum limit, the strain tensor $\bar{\varepsilon}$ can be obtained from the theory of elasticity with its components given as [91]

$$\varepsilon_{\mathrm{mn}} = \frac{1}{2}(\partial_{\mathrm{n}} u_{\mathrm{m}} + \partial_{\mathrm{m}} u_{\mathrm{n}}), \qquad m, n \in \{x, y\}\,. \tag{2.40}$$

For simplicity, only in-plane strain is considered here. Then, the displacement vectors can be approximated in terms of strain tensor as

$$\vec{u}_{\mathrm{j}} \approx \begin{pmatrix} \varepsilon_{\mathrm{xx}} & \varepsilon_{\mathrm{xy}} \\ \varepsilon_{\mathrm{yx}} & \varepsilon_{\mathrm{yy}} \end{pmatrix} \cdot \vec{d}_{\mathrm{j}}. \tag{2.41}$$

Scalar potential

The changed bond lengths lead to shifts in the on-site energies of the p_{z} orbitals, resulting in a modification in the Dirac equation that can be described by an effective scalar potential [44, 92]. The strain dependence of this scalar potential can be written as [44, 90, 93]

$$V(x, y) = V_0 \cdot (\varepsilon_{\mathrm{xx}} + \varepsilon_{\mathrm{yy}}) \tag{2.42}$$

with $V_0 \approx 2.5\,\mathrm{eV}$, which is estimated from a theoretical work function study of graphene [90]. The scalar potential manifests as an additional doping for graphene, which can be observed in transport experiments as a strain-induced shift of the CNP in gate voltage.

Vector potential and pseudomagnetic field

For the nearest-neighbor tight-binding model, a change in the bond length would lead to a perturbation of the hopping energy t and thus results in different hopping energies t_{j} for the neighboring atoms. Based on an exponential decay assumption, the dependence of the renormalized hopping energy on the change of the bond length can be written as [43]

$$t_{\mathrm{j}} = t e^{-\beta \frac{\Delta d}{a_0}}, \tag{2.43}$$

where $\beta = \partial \log t / \partial \log a\,|_{a=a_0} \approx 3.37$ is the modulation factor for the strained hopping energy. For small strain, Eq. 2.43 can be expanded to the first order and one obtains

$$t_{\mathrm{j}} = t(1 - \beta \frac{\Delta d}{a_0}), \tag{2.44}$$

In the assumption of a spatially smooth strain field and a set of constant hopping energies $\{t_1, t_2, t_3\}$ within a local vicinity, a "local" effective Hamiltonian could be written as

$$\tilde{H} = t \cdot \begin{pmatrix} 0 & \tilde{f}(\vec{q}) \\ \tilde{f}(\vec{q})^* & 0 \end{pmatrix}, \tag{2.45}$$

where

$$\tilde{f}(\vec{q}) = \sum_j (1+\delta_\mathrm{j}) e^{i\vec{q}\cdot\vec{d}_\mathrm{j}} \qquad \text{and} \qquad \delta_\mathrm{j} \equiv (t_\mathrm{j} - t)/t. \tag{2.46}$$

Expending $\tilde{f}(\vec{q})$ around the two valleys to the first order in $\vec{q}$ with Eq. 2.39, Eq. 2.41 and Eq. 2.44, the Hamiltonian in Eg. 2.45 becomes

$$\tilde{H}_{\pm K} \approx v_\mathrm{F}\hat{\sigma}(\hbar\vec{k} \pm e\vec{A}), \tag{2.47}$$

where

$$\vec{A} = \frac{\hbar\beta}{2ea_0}\begin{pmatrix} \varepsilon_\mathrm{xx} - \varepsilon_\mathrm{yy} \\ -2\varepsilon_\mathrm{xy} \end{pmatrix} \tag{2.48}$$

and the ±-sign accounts for the two valleys. The term $\vec{A}$ induced by strain resembles the vector potential from a magnetic field, which is commonly called pseudo-vector potential. Taking the curl of the pseudo-vector potential, one obtains the pseudomagnetic field (PMF) as

$$\vec{B}_\mathrm{ps} = \bigtriangledown \times \vec{A} = (0,\ 0,\ \partial_\mathrm{x}A_\mathrm{y} - \partial_\mathrm{y}A_\mathrm{x}) = (0,\ 0,\ B_\mathrm{ps}). \tag{2.49}$$

It is important to note that the PMF has an opposite sign for the two valleys, as can be seen in Eq. 2.47.

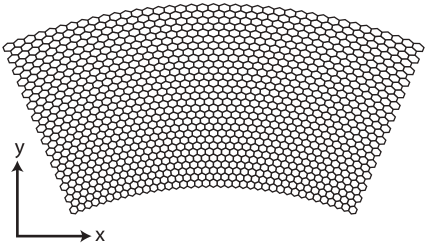

Figure 2.8. Strain pattern for homogeneous PMF. Illustration of rectangular graphene deformed into an arc. A strain gradient is generated along y-direction. Figure adapted from Ref. [44].

It is obvious from Eq. 2.48 that the PMF depends on the strain configurations. For uniform strain fields, such as uniaxial and biaxial strain, $\vec{A}$ is a constant which leads to zero PMF [43, 45, 86]. One needs a non-uniform strain field to generate a PMF. An example is given in Fig. 2.8, where a strain gradient is generated in y-direction by deforming a rectangular graphene ribbon into a circular arc. The deformation field can be described approximately with the following form [44]:

$$\vec{u}(x, y) = \frac{1}{R}\left(xy, -\frac{x^2}{2}\right), \tag{2.50}$$

with R being the radius of the inner circle. Plugging it into Eq. 2.48 results in

$$\vec{A} = \frac{\hbar\beta}{2ea_0}\begin{pmatrix} y/R \\ 0 \end{pmatrix}, \tag{2.51}$$

which would then translate to a fairly homogeneous PMF using Eq. 2.49.

Fermi velocity renormalization

For pristine graphene, usually a constant Fermi velocity v_F is assumed. In the case of strain, the Fermi velocity becomes directional-dependent, which comes from a warping of the Dirac cones and can be written in a tensorial notation as [94–97]

$$\bar{\boldsymbol{v}} = v_\mathrm{F}\left(\bar{\boldsymbol{I}} + (1-\beta)\bar{\varepsilon}\right), \tag{2.52}$$

where $\bar{\boldsymbol{I}}$ is the 2×2 identity matrix and $\bar{\varepsilon}$ is the strain tensor. For uniaxial strain, it exhibits a strong anisotropy [43]. With large uniaxial strains, quasiparticles can even become massive along the strain direction while in the perpendicular direction they remain massless [90].

Since the strain levels involved in the experiments presented in this thesis are quite small ($\leqslant 1\,\%$), where the Fermi velocity renormalization is not pronounced, we will not go into the details of this effect. More information about this topic can be found in Ref. [90, 94, 97].

2.3.2. Valley Hall and inverse valley Hall effect

As introduced in section 2.1.1, valley is another degree of freedom in graphene, which can be manipulated to generate charge-neutral current. In analogy to the spin Hall effect and the inverse spin Hall effect, the valley Hall effect (VHE) and the inverse valley Hall effect (IVHE) are phenomena that converts charge currents to pure valley currents and vice-versa.

In a study of graphene/hBN superlattice, a detected non-local signal was interpreted with the VHE and the IVHE [99]. It has been argued that the aligned hBN substrate breaks the inversion symmetry of graphene which opens an energy gap at the Dirac point and gives rise to a finite Berry curvature. Due to the opposite sign of the Berry curvature for the two valleys, electrons acquire an anomalous velocity and lead to a valley-polarized current in the

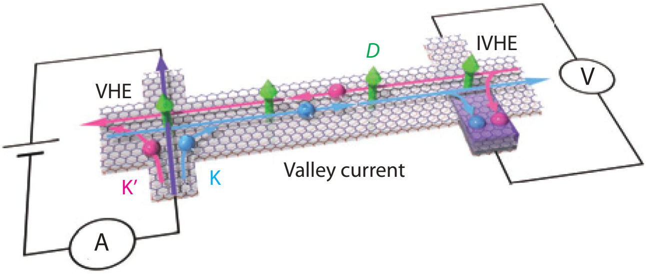

Figure 2.9. Valley Hall and inverse valley Hall effect. Schematic of non-local measurement based on VHE and IVHE in bilayer graphene. A displacement field (D) realized with dual-gating is used to induce a gap. On the left side, the charge current leads to a pure valley current in the transverse direction via the VHE. On the right side, this valley current is converted into a charge current by means of the IVHE, generating a non-local voltage. Figure adapted from Ref. [98].

bulk transverse to the charge current, which is the VHE. By means of the IVHE, the valley current is converted back to charge current and results in an electrical response in remote regions. Similar results have been reported for bilayer graphene [98, 100], where dual-gating is used to break the inversion symmetry. A schematic demonstrating the VHE and the IVHE in bilayer graphene is shown in Fig. 2.9. Analogous to the spin Hall effect and the inverse spin Hall effect [101], a non-local resistance from the VHE and the IVHE is given by[98, 100]

$$R_{\mathrm{NL}} = \frac{1}{2}\rho_{\mathrm{xx}}^{3}(\sigma_{\mathrm{xy}}^{\mathrm{VH}})^{2}\frac{W}{\lambda_{\mathrm{v}}}\exp(-\frac{L}{\lambda_{\mathrm{v}}}), \tag{2.53}$$

where ρ_{xx} is the local resistivity, $\sigma_{\mathrm{xy}}^{\mathrm{VH}}$ is the valley Hall conductivity and λ_{v} is the intervalley scattering length. L and W represent the length and width of the Hall bar channel, respectively. Therefore a cubic dependence of the non-local resistance on the local resistivity is thought to be an evidence of pure valley current.

Since strain induced PMF has opposite signs for the two valleys, as introduced in section 2.3.1, non-uniform strain field can be used as another approach to generate valley-polarized currents. It has been predicted that strain-induced VHE and IVHE can be observed even with modest strain levels (lower than those required for observing pseudo-LLs) in disordered samples (diffusive regime), with a large non-local resistance as the hallmark [102]. Our related experiments are presented in chapter 4.

2.3.3. Strain characterization with Raman spectroscopy

Raman spectroscopy has been used extensively to characterize properties of semiconductors [103–105]. It has proven to be a versatile tool for studying the properties of graphene as well, such as to determine the number of layers, the defect density, the amount of doping, the edge chirality, and the strain levels [54, 106, 107].

Raman spectroscopy in graphene

To interpret the Raman spectra of graphene, it is essential to understand the phonon dispersion, which is shown in Fig. 2.10. There are in total six phonon branches in graphene due to the two-atom unit cell, including three acoustic (A) and three optical (O) phonons [106]. Two of the phonon branches are out-of-plane (o): one acoustic and one optical. The other four branches are in plane (i). The phonon modes are further classified as longitudinal (L) or transverse (T) according to vibrations along or perpendicular to, respectively, the carbon-carbon bonds.

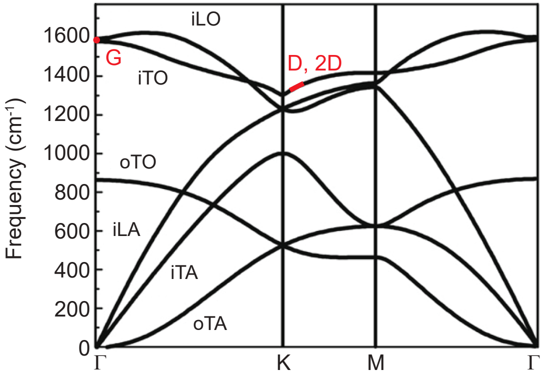

Figure 2.10. Phonon dispersion of graphene. All six phonon branches are shown. The phonons associated with the G, D and 2D Raman bands are highlighted. Figure adapted from Ref. [54, 106, 108].

The in-plane transverse optical (iTO) and in-plane longitudinal optical (iLO) phonons are responsible for the main Raman bands, the G band and the 2D band, in graphene. It is important to note that the energies of both the iTO and the iLO phonons are strongly dispersive and relatively lower at the Γ and K points, as can be seen in Fig. 2.10. Such phonon energy softening is caused by the renormalization of the phonon energy due to electron-phonon coupling at these points, which is known as the Kohn anomaly [109, 110].

The mechanism for the G band is shown schematically in Fig. 2.11(a), an incident photon resonantly excites a virtual electron-hole pair in the graphene, which is scattered by either an iTO or an iLO phonon at the Γ point (center of the first Brillouin zone) and then re-combines, emitting a photon that is red-shifted by the amount of energy given to the phonon. The phonons involved in this process have very little momentum, since it occurs at the Γ point.

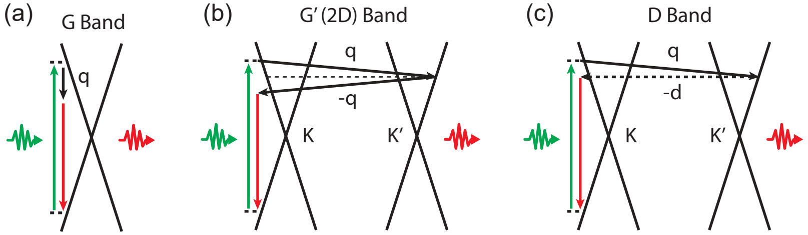

Figure 2.11. Illustration of main Raman processes in graphene. (a) G band, involving a phonon with almost zero momentum. **(b)** G' or 2D band originating from a double resonant process with electronic levels. Two phonons are involved. **(c)** D band, involving one phonon and a defect scattering (horizontal dashed line). Figure adapted from Ref. [54].

The strongest Raman peak in graphene is the 2D (or G') band, which is a second order process involving two iTO phonons, as shown in Fig. 2.11(b). The incident photon creates an electron-hole pair near the K point. The electron is then scattered by an iTO phonon to the K' point inelastically. Due to the energy and momentum conservation, the electron must scatter back to the K point in order to recombine with the hole. In the 2D band case, the back-scattering of the electron is mediated by a second iTO phonon. Since the incident photon and the first phonon scattering (or the scattered photon and the second phonon scattering) are resonant with electronic levels in the graphene, this process is known as double resonant. In experiments, the number of graphene layers in a flake can be determined by the 2D band [111].

Another important band is the D band, which is induced by disorder and therefore can be used to determine the defect density in graphene. The first half of the Raman process for this band is the same as that for the 2D band. In the second half of the process, the electron is elastically back-scattered from the K point to the K' point by a defect [112–114], different from the inelastic scattering with a second iTO phonon for the 2D band. Since the process only involves one phonon for the D band, the energy shift is half of that for the G' (2D) band. This is the reason why the G' band is now commonly called 2D band.

A typical Raman spectrum with characteristic G and 2D peaks of a pristine graphene flake is shown in Fig. 2.12. The intensity of the 2D peak is much higher than that of the G peak, which is a signature of monolayer graphene. The D peak is absent, indicating a defect-free graphene. The G peak occurs at $\sim$1580 cm^{-1}, which is independent of the energy of the incident photon. This is because only virtual elecoton-hole pairs are involved in this process and the involved phonons are always from the Γ point. In the case of 2D and D bands, the involved phonon frequency changes with the incident photon energy due to the resonance with the electronic levels and the highly dispersive phonon energy at the K/K' point. For incident photons with an energy of 2.41 eV, the 2D peak appears at $\sim$2700 cm^{-1}.

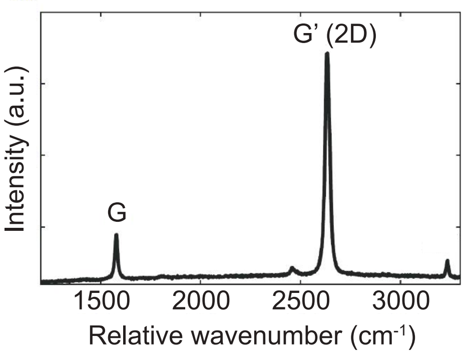

Figure 2.12. Example Raman spectrum of graphene. Raman spectrum of a pristine graphene flake, showing the characteristic G and 2D (G') bands.

Strain characterization

Since Raman spectroscopy probes the phonon frequency in graphene, strain, which shifts the frequency of the phonons involved in the G and 2D bands, can therefore be determined from Raman measurements [89]. Strain changes the inter-atomic distance and hence modifies the vibration frequency of the lattice. Tensile strain usually results in phonon softening, and the opposite for compressive strain [115].

Characteristic redshifts in the Raman peaks of graphene have been observed with tensile strain [115–117]. One example is shown in Fig. 2.13, where the strain was induced by bending a flexible substrate with graphene flakes directly deposited on top. The strain values were calculated from the bending of the substrate. In addition to the redshift, the G peak shows a clear splitting into two subbands (G^+ and G^-) with strain due to the degeneracy lifting of iTO and iLO phonon modes at the Γ point. The 2D peak does not develop a splitting, which has been reported to only occur when large strain is applied along high-symmetry directions [118]. The orientation of the graphene crystal with respect to the uniaxial strain axis can be determined from measurements with different light polarization, thanks to the polarization dependence of the G^+ and G^- intensities [115].

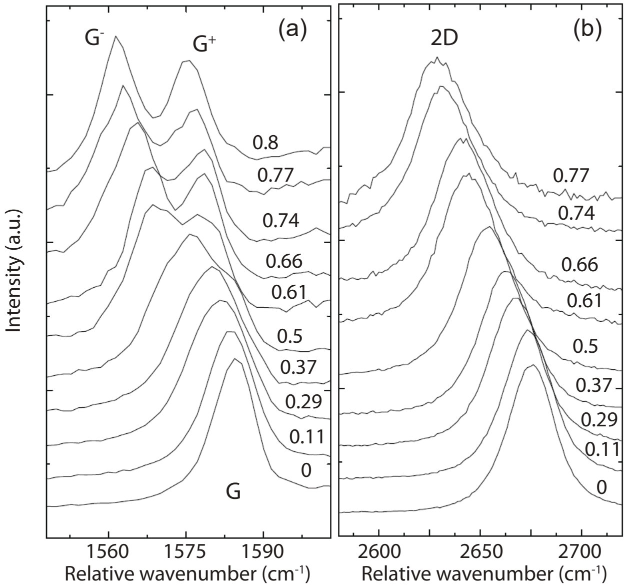

Figure 2.13. Redshift of Raman peaks with strain. (a) G and **(b)** 2D peaks of graphene Raman spectra measured with linearly polarized light along the uniaxial strain direction for different strain levels. For higher strain, the G peak splits into two subbands, G^+ and G^-, while the 2D peak broadens. The numbers on the right side of the spectra indicate strain values in %. Figure adapted from Ref. [115]

In our experiments, we use Raman spectroscopy as a tool to quantify the strain generated in graphene, based on the redshift of the G and 2D peaks. It is worth noting that there is a disagreement in the literature about the shifting rates [115–120], which might arise from the different ways of strain determination. We choose an intermediate one among the reported values for the strain characterization, which can still be recalibrated when the shift rates are precisely confirmed.

2.4. Moiré superlattice

A moiré superlattice is a larger-scale lattice structure that can be produced when two similar lattices are superimposed. Such a superlattice was already observed in 1925 in an X-ray diffraction study on gold-copper and palladium-copper systems [121]. Hexagonal boron nitride (hBN) is now a widely used substrate for graphene devices. It has also a honeycomb lattice and therefore can form moiré superlattice with graphene, which can modify the electronic properties of graphene. In the following we introduce the graphene/hBN moiré superlattice and also discuss its implications on the electronic band structure of graphene.

2.4.1. Formation of graphene/hBN superlattice

Similar to graphene, the lattice of hBN is also hexagonal, but its unit-cell consists of two different atoms (boron and nitrogen) as illustrated in Fig. 2.14(a). The lattice constant of hBN is ~1.8 % larger than that of graphene. Instead of a zero-gap semiconductor, hBN is an insulator with a large band-gap of 5.97 eV, making it a good substrate and dielectric for graphene devices. When a graphene lattice is place on a hBN lattice, a moiré superlattice forms. Due to the small lattice mismatch, the supperlattice is present even when the two lattices are fully aligned, as shown in Fig. 2.14(b).

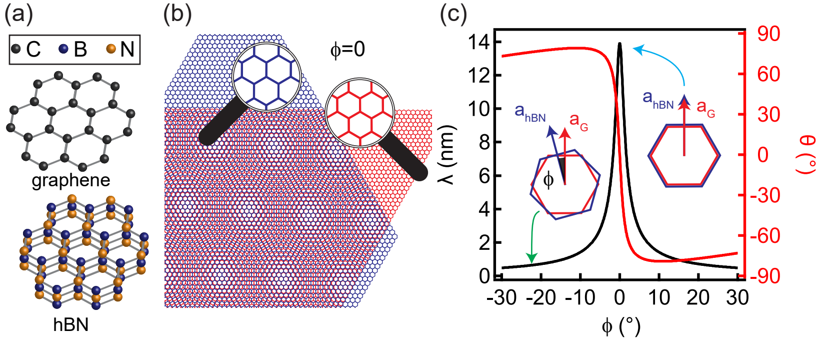

Figure 2.14. Graphene/hBN moiré superlattice. (a) Lattice structures of graphene and hBN. The unit-cell of graphene consists of two carbon atoms, while that of hBN consists of one boron and one nitrogen atom. **(b)** Illustration of the moiré superlattice when graphene and hBN lattices are fully aligned. **(c)** Superlattice period λ and orientation θ plotted as a function of twist angle ϕ according to Eq. 2.54 and Eq. 2.55. Figure adapted from Ref. [55]

With only geometrical analysis, the period (λ) of a graphene/hBN superlattice can be calculated and is given by [122, 123]

$$\lambda = \frac{(1+\delta)a}{\sqrt{2(1+\delta)(1-\cos\phi)+\delta^2}} \tag{2.54}$$

with $a = 2.46\,\text{Å}$ ($a = \sqrt{3}a_0$) being the graphene lattice constant, $\delta = 0.018$ being the lattice mismatch between hBN and graphene, and ϕ being the twist angle between the two lattices. The orientation of the superlattice relative to the graphene lattice is described by the angle θ:

$$\tan\theta = \frac{-\sin\phi}{(1+\delta)-\cos\phi}. \tag{2.55}$$

In Fig. 2.14(c), the functional dependence of λ and θ on ϕ is plotted for $-30° \leqslant \phi \leqslant -30°$, which covers all the possibilities due to hexagonal symmetry. The superlattice period reaches its maximum at $\phi = 0$ with a value of $\lambda \approx 14\,\text{nm}$, while it decreases rapidly with increasing ϕ. The superlattice orientation is also very sensitive to ϕ at small twist angles, whereas it almost saturates at large angles. The graphene/hBN superlattices have been first observed and studied by scanning tunneling microscopy (STM) [122, 124, 125].

2.4.2. Band structure modification

The presence of moiré superlattice causes a modification to the electronic band structure of graphene. The signature of that is the emergence of additional Dirac points located symmetrically around the original Dirac point of graphene, which are commonly called satellite/secondary/superlattice Dirac points (SDPs). Using the model of a simple potential modulation, the SDPs are predicted to appear at the boundary of the superlattice Brillouin (SBZ) [126]. However, the details of the modified band structure is still not fully known. Three different moiré band reconstructions for graphene on hBN from Ref. [127] are shown in Fig. 2.15, which strongly depend on the model and the parameters therein. The corresponding DoS for the three different models are plotted in the bottom panel of Fig. 2.15. The DoS drops to zero at one point (SDP) on the hole side ($E < 0$) for all three cases, while on the electron side ($E > 0$) only a modulation of the DoS is observed. The number of SDPs generated in the SBZ for each main DP also depends on the model and parameters, as can be seen in the top panel of Fig. 2.15.

In transport measurements, the moiré superlattice manifests as conductance dips at high doping symmetrically around the main DP. As mentioned above, SDPs are expected to form at the SBZ boundaries at $\vec{k} = \vec{G}/2$, where $|\vec{G}| = 4\pi/(\sqrt{3}\lambda)$ is the length of the superlattice wave vector and λ the moiré period.

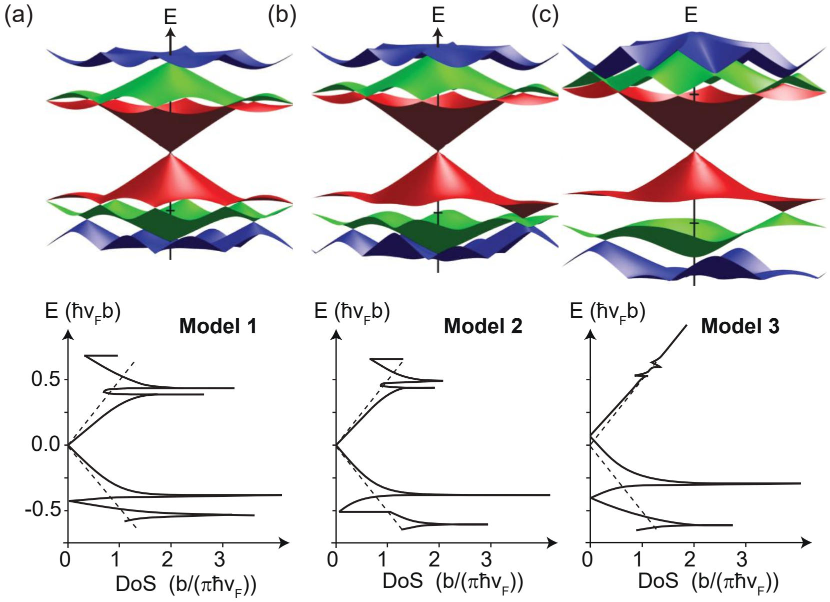

Figure 2.15. Possible reconstructed band structure by moiré superlattice. (a-c) Top: three different moiré miniband calculated using different model-parameters. Bottom: corresponding DoS as a function of energy. The dashed lines indicate the DoS of pristine graphene. Figure adapted from Ref. [55, 127].

For graphene, k is related to n by $k = \sqrt{\pi n}$. The position of the SDPs in charge carrier density for a given period λ is then given by

$$n_\mathrm{s} = \frac{4\pi}{3\lambda^2} \tag{2.56}$$

Therefore, the moiré period and the twist angle can be extracted from the charge carrier density where the characteristic conductance dips are observed. It is important to note that even though a moiré superlattice is always present in graphene/hBN systems, the signature in transport measurements is only observable for small twist angles. This is because for large twist angles, the moiré period is very small and the characteristic conductance dips would occur at very high carrier densities, as can be seen from Eq. 2.56, which cannot be accessed with conventional gating. The moiré superlattice has been demonstrated in various transport experiments [35–37, 39, 70, 99, 128–130]. In quantum Hall regime, a fourfold degeneracy of the LLs was found around the SDPs, implying only one SDP in the SBZ for each main DP [35, 37].

3 Experimental methods

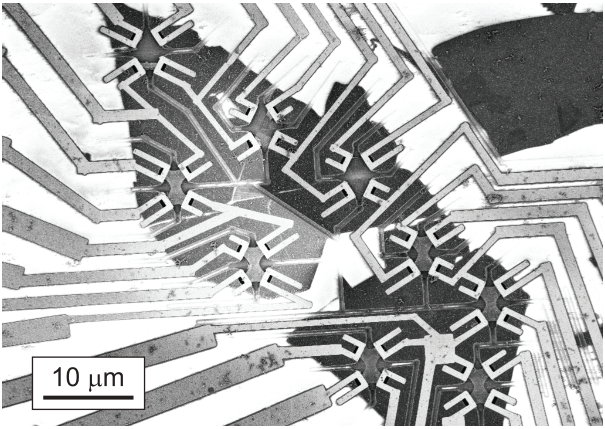

This chapter is dedicated to the description of important experimental methods used in this thesis. First, the key fabrication techniques for different types of devices are introduced, followed by an introduction to the bending setup for strain measurements. Furthermore, the basic concepts of the low temperature transport measurements is briefly described[1].

---

[1] A SEM image of multiple suspended devices is shown.

3.1. Sample fabrication

For all the experiments presented in this thesis, clean graphene is a prerequisite. To obtain clean graphene devices, two main techniques have been developed in the community. The first one is to suspend graphene above the SiO_2 substrate in order to avoid its influence and perform current annealing to remove the resist residuals from fabrication [131–135]. A more widely used technique nowadays is to use hBN as the substrate [18, 136–138], which is atomically flat and expected to be free of surface charge traps, and encapsulate graphene in order to protect it from resist residuals.

In this section, we introduce the most important techniques of fabricating clean graphene devices. First, the exfoliation of graphene and hBN is described. Then a short introduction to the fabrication of suspended devices is given, followed by the presentation of assembling hBN/graphene/hBN heterostructures. Standard nanofabrication procedures, such as electron beam lithography, reactive ion etching and metallization with thermal or e-beam evaporation are used to complete the device fabrication, but are not discussed here. All the detailed fabrication recipes can be found in the appendix A.

3.1.1. Exfoliation

The 2D material research field started with the first successful isolation of graphene with mechanical exfoliation in 2004 [3]. Nowadays the exfoliation technique is applied to the isolation of many other materials, such as hBN and TMDCs.

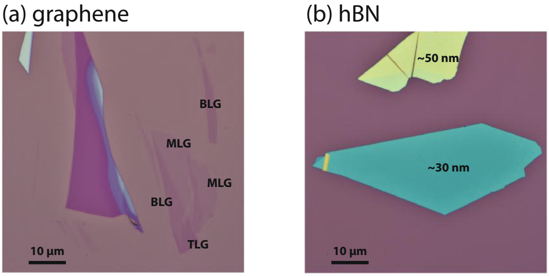

Figure 3.1. Graphene and hBN exfoliation. (a) Exfoliated graphene flakes on a Si wafer with ~285 nm of SiO_2. Monolayer (MLG), bilayer (BLG) and trilayer (TLG) graphene can be easily distinguished. **(b)** Exfoliated hBN flakes. We usually use the flakes with a thickness of ~30 nm.

In our experiments, Nitto[2] tape was used for exfoliation. Graphene flakes were exfoliated from natural graphite[3]. The hBN flakes were exfoliated from high quality crystals grown by K. Watanabe and T. Tanaguchi [139]. Examples of exfoliated graphene and hBN flakes are shown in Fig. 3.1. The number of layers for graphene can be easily determined from the optical contrast, when the flakes are exfoliated onto Si wafers with ∼285 nm of SiO_2. For the fabrication of suspended samples, graphene was exfoliated onto PMMA, where contrast enhancement with filters was used for the recognition of monolayers. For hBN, we usually choose the flakes with a thickness of ∼30 nm, which can be recognized by the color under optical microscope, see e.g. the flake shown in Fig. 3.1(b).

3.1.2. Suspension

The suspension of graphene was first achieved by etching away the SiO_2 below the contacts using Hydrofluoric acid (HF) [131, 133]. Later an alternative suspension technique based on lift-off resist (LOR) was developed [134], which is compatible with most standard PMMA based nanofabrication procedures.

In our experiments, the LOR[4] based technique was used and the samples were fabricated following a recipe by Maurand et al. [135], shown schematically in Fig. 3.2(a-c). The fabrication starts with the preparation of substrates with bottom gates, followed by the spin coating of LOR. A further lithography step is needed to open a window in LOR for bonding pads. Graphene is then transferred and aligned to the bottom gates using a wet transfer method [136]. First, graphene flakes are exfoliated on wafers with a PMMA/dextran double layer. The dextran layer is then dissolved in water, releasing the PMMA membrane with the graphene floating on the surface of water. In the next step, the floating PMMA layer is fished out with a glass slide with a volcano structure. After drying, it is transferred on top of the bottom gate structures with the help of a transfer stage and a microscope. Standard e-beam lithography and oxygen plasma are then used to make metal contacts and shape the device. In the last step, the LOR below the graphene and contacts is exposed with a very high e-beam dose (much higher than that for PMMA) and subsequently dissolved in Ethyl-lactate, leaving the graphene and contacts freely suspended. The SEM image of a multi-terminal test device is shown in Fig. 3.2(d), where resist residuals can be easily seen on the suspended graphene.

Before transport measurements, current annealing is performed at low temperatures to remove the resist residuals, where a DC voltage is ramped up and down across the device, heating up the graphene to hundreds of degrees [140]. Ultraclean graphene has been achieved for two-terminal devices [141], while the current annealing on multi-terminal devices remains challenging. Details of the fabrication and discussions on limitations of suspended graphene samples can be found in Ref. [142].

---

[2] For example, SPV 224P, Nitto Europe NV

[3] Obtained from NGS Trading & Consulting GmbH.

[4] LOR 5A, MicroChem Corp.

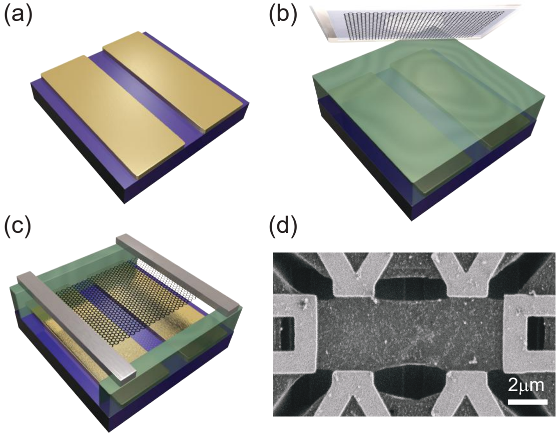

Figure 3.2. Fabrication of suspended graphene (a) Bottom gates prefabricated on the substrate. **(b)** LOR spin-coated. Then graphene is transferred on LOR with alignment to the bottom gates. **(c)** Graphene is shaped and the LOR is removed with selective e-beam exposure. The device is suspended with free-standing contacts. **(d)** A SEM image of a multi-terminal suspended graphene device for test. Fabrication schematics are adapted from Ref. [135].

3.1.3. Encapsulation

The key steps of encapsulating graphene with hBN are shown schematically in Fig. 3.3 following the pick-up technique introduced by Wang et al. [138] and Zomer et al. [143]. First, a polycarbonate (PC) film is prepared on a glass slide, which is later picked up by an adhesive tape with a ~1 cm × 1 cm window in the center. The PC film is then transferred on top of a ~0.5 cm × 0.5 cm PDMS stamp fixed on a glass slide, as shown in Fig. 3.3(b). Additional tape is used along the edges of the window to fix the PC film on the glass slide. The glass slide with the assembled PDMS/PC stamp is then mounted on a xyz-stage of a home-built transfer microscope for picking up the flakes exfoliated on Si wafers. The flakes are selected and located optically beforehand. The wafer with the top hBN is first mounted on the transfer stage and a clean area

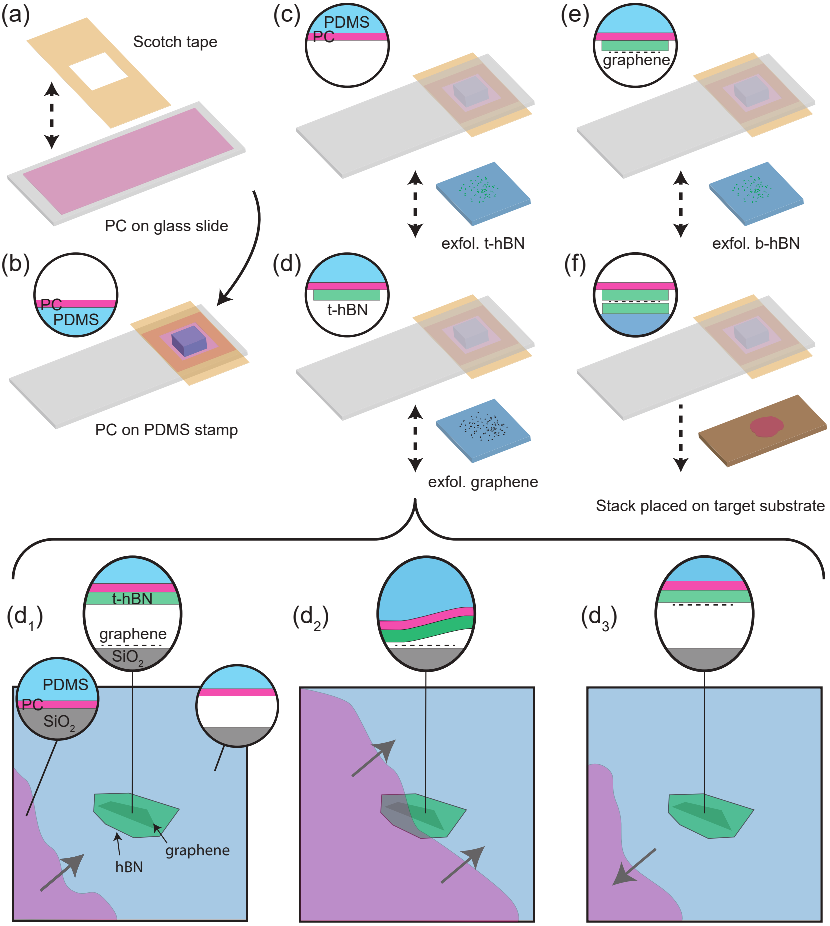
(a)
Scotch tape
PC on glass slide
(b)
PC
PDMS
PC on PDMS stamp
(c)
PDMS
PC
exfol. t-hBN
(d)
t-hBN
exfol. graphene
(e)
graphene
exfol. b-hBN
(f)
Stack placed on target substrate
(d$_1$)
t-hBN
graphene
SiO$_2$
PDMS
PC
SiO$_2$
graphene
hBN
(d$_2$)
(d$_3$)

Figure 3.3. Flow chart of graphene encapsulation. (a-b) PC film and PDMS/PC stamp preparation. **(c-e)** Picking up the flakes sequentially, top hBN, graphen and bottom hBN. **(f)** Placing down the assembled stack onto the target substrate. Details of each step is shown in the circular insets. Figure adapted from Ref. [55, 76].

of the PC film is then used to pick up the desired flake, see Fig. 3.3(c). Details of this process will be described in the next step for picking up graphene. After a successful pick-up of the top hBN, we exchange the wafer for the one with graphene flake and use the picked-up top hBN to pick up the graphene flake. The transfer stage also has a roll and pitch degree of freedom. These two parameters are used to tilt the bottom stage relative to the top translation stage, so that the PC film can touch the wafer gradually. In this step, the flakes need to be aligned so that the graphene is fully covered by the hBN. As shown in Fig. 3.3(d1), the PDMS/PC stamp is lowered until it touches the wafer at one corner. The contact front (CF), which is the interface between the region still suspended and that in contact with the wafer, is moved forward slowly by further lowering the PDMS/PC stamp carefully until the top hBN is just next to the graphene flake. The stage is then heated, leading to a thermal expansion of the PC film, which moves the contact front across the graphene flake making the top hBN fully in contact with the graphene, see Fig. 3.3(d2). This usually happens during heating from room temperature to 80 °C. Once it goes over both flakes, the CF is kept at a fixed position by slowly retracting the PDMS/PC stamp until the temperature reaches 80 °C. The heater is switched off at 80 °C and the substrate starts to cool down. A few minutes later, the PC film starts to shrink and retract automatically, as shown in Fig. 3.3(d3). The flake will be picked up during retraction because graphene sticks better to hBN than to SiO_2 due to stronger interaction. That is also the mechanism when picking up the top hBN layer in the first step.

For making moiré superlattice samples, one needs to align the sharp edges of both flakes, because the flakes tend to cleave along crystallographic directions. Since the zigzag and armchair directions are equally favorable, theoretically only half of the attempts will succeed on average. In reality, the yield can be lower due to the imperfect alignment accuracy.

For the bottom hBN, there can be different procedures depending on the experiments. Usually, the top hBN/graphene half stack is place onto the bottom hBN, which is exfoliated on a wafer with markers. Afterwards, other fabrication steps can be done directly on this wafer. For strain experiments, the full stack needs to be transferred onto a flexible substrate. Therefore, we pick up the bottom hBN in the similar way instead of placing the first two layers onto it, see Fig. 3.3(e). In the last step, the assembled hBN/graphene/hBN stack is transferred onto the target substrate by heating the substrate to 150 °C to detach the PC film from the PDMS stamp, as shown in Fig. 3.3(f). At this temperature, the PC film sticks better to the substrate than to the PDMS stamp. In the end, the PC is dissolved in chloroform, leaving the assembled stack on the substrate.

Afterwards, the stack is characterized with AFM to locate bubble-free regions and determine the thickness of both hBN layers for device design. Later, standard nanofabrication techniques, including e-beam lithography, reactive ion etching and metallization processes, are used to make electric contacts and shape the stack into the desired device geometry. Detailed recipes are given in the appendix A.

Suspend encapsulated graphene

A few suspended encapsulated graphene devices were also fabricated for strain experiments before we fully focused on the on-substrate approach.

First, palladium leads are fabricated on LOR above the bottom gate structures with thermal evaporation, which are used to support the stack and also to protect the LOR underneath from unwanted exposure during the e-beam evaporation of Cr/Au contacts. The stacks are assembled in the way described above and transferred onto the palladium supporting leads. Afterwards, standard fabrication processes for encapsulated samples are used and in the end the devices are suspended in the way described in section 3.1.2.

3.2. Strain setup

For generating strain in graphene, we fabricate the devices on a flexible substrate and use a three-point bending setup to deform the substrate, which is adapted from a home-built break-junction setup. In this section, we first introduce the preparation of the flexible substrates, followed by the description of the bending setup. Furthermore, a brief introduction to the Raman setup for characterizing strain is given.

3.2.1. Flexible substrate preparation

We use 0.3 mm thick phosphor bronze plate[5] as the flexible substrate. The commercially available phosphor bronze plates are already quite flat, but for our nanofabrication purpose it is not flat enough, as can be seen later in Fig. 3.4. The plate is first cut into 5 cm × 5 cm pieces and polished with a lapping machine. Afterwards, a layer of ∼5 µm polyimide[6] (PI) is deposited onto the polished plate by spin coating for electrical isolation. The roughness of the PI surface is characterized with a profilometer and compared to that of PI deposited on an unpolished plate, as shown in Fig. 3.4. The surface is much flatter after polishing and on the length scale of 20 µm, the length scale for device fabrication, it is almost as flat as the surface of Si wafers. Detailed recipe for PI deposition and curing is given in the appendix A

The plate with PI is then cut into smaller pieces with dimensions of 24 mm × 9.5 mm using a diamond wire saw. PMMA is spin coated on the PI surface beforehand to protect the PI surface from metal fragments generated during sawing. After that, the protecting PMMA layer is removed and standard nanofabrication techniques are used to prefabricate big structures, including the bottom gate with markers, metallic leads and contact pads. The bottom gate has a varying width of 10 µm to 30 µm for different size of flakes. Till then the preparation of the substrate is completed. A typical prepared substrate is shown in Fig. 3.5(b). Both suspended and encapsulated devices can be fabricated on these substrates with the methods described in section 3.1.

---

[5] CuSn6, häuselmann metall GmbH

[6] PI2610, HD MicroSystems GmbH

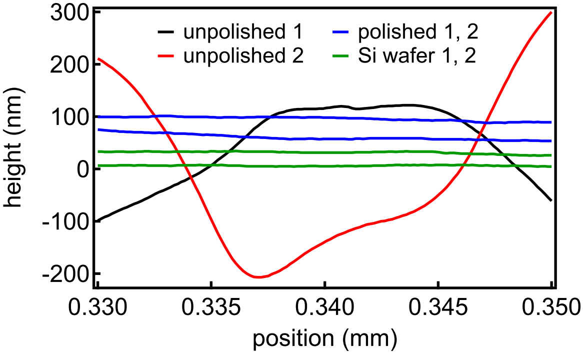

Figure 3.4. Surface roughness. The height profiles of PI surface on unpolished bronze plates (black and red) and on polished bronze plates (blue) are plotted for a 20 µm distance. For reference, the height profiles on the surface of Si wafers (green) are also plotted. In this length scale, the polished surface is almost as flat as the Si wafer. The curves are shifted in y-direction for clarity.

3.2.2. Three-point bending setup

Inspired by the break junction technique [144–147], we use a three-point bending setup to deform the flexible substrate and therefore generate strain in graphene. The setup cross section is shown schematically in Fig. 3.5(a), where the substrate is mounted between two fixed counter supports and a movable wedge. The deformation of the substrate is controlled by the displacement Δz of the pushing-wedge relative to the mounting position.

Strain in graphene can be characterized with Raman spectroscopy, as introduced in section 2.3.3. We use a commercially available confocal Raman system WiTec alpha300. The bending setup can be mounted under the Raman microscopy, as shown in Fig. 3.5(c), making the strain characterization very convenient. The displacement Δz of the pushing-wedge is controlled by the long screw sticking out. Due to the reduction effect of the gear system, one full rotation of the screw corresponds to a displacement of $\Delta z \approx 20\,\mu\text{m}$, giving a very fine control of the substrate deformation and hence the strain in graphene. With the fine-positioning piezoelectric stage, spatially resolved Raman maps can be measured, which is important for characterizing strain fields over the whole device area. The system is also equipped with light polarizers, making it possible to determine the strain direction with respect to the crystallographic directions of graphene [115]. The presented Raman spectra in this thesis were acquired in ambient conditions using linearly polarized laser with a wavelength of 532 nm and a power of 1 mW, unless otherwise stated. The laser spot size is around 500 nm and the used grating of the spectrometer is 600 grooves/mm. The measurements of strain characterization on different types of devices are presented in chapter 5.

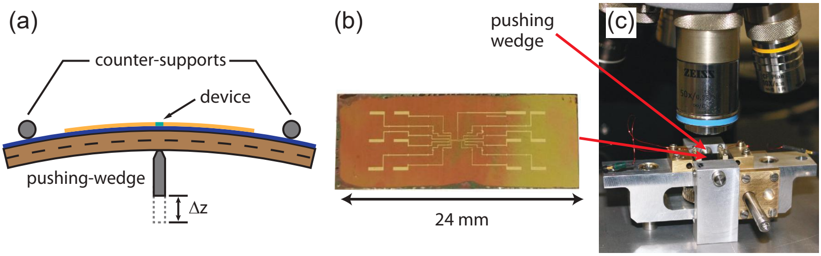

Figure 3.5. Three-point bending setup. (a) Schematic cross section of the bending setup. The displacement Δz of the pushing-wedge determines the substrate deformation. **(b)** A typical prepared flexible substrate. The gate structure in the center, metallic leads and contact pads are prefabricated. **(c)** Room temperature bending setup mounted under the Raman microscope.

For low-temperature transport measurements, we have another bending setup shown in Fig. 3.7. We relate the induced strain from one setup to the other through the displacement Δz of the pushing-wedge. More details of the low temperature setup are discussed in section 3.3.2.

3.3. Low-temperature electrical measurements

For studying strain effects in transport measurements at low temperatures, we need to make the bending setup compatible with cryostat. At the same time, the electrical contact to the devices should be reliable during bending of the substrate. In this section, we first introduce the method we use to electrically connect the devices. Then a introduction to the low temperature bending setup is given, follow by a brief description of electrical measurements.

3.3.1. Electrical connection

For devices using SiO_2/Si as substrate, electrical connection is usually made by wire bonding. In our case, wire bonding is not applicable due to the special substrate (PI coated phosphor bronze). Instead, we use electrical clamps which can be fixed to the nanofabricated contact pads on the substrate with screws, as shown in Fig. 3.6(a,b). First, small indium pieces with a diameter of ∼2 mm and a thickness of ∼0.5 mm are placed on the contact pads, see left side of Fig. 3.6(b). Second, the clamp is placed on top, with the pins aligned to the indium pieces, and fixed to the substrate by screwing to the counterparts on the other side of the substrate, see right side of Fig. 3.6(b). The connector at the other end of the clamp can then be plugged into a socket and makes connections to measurement electronics. In the other direction, the contact pads on the substrate are connected to the devices through on-chip metallic lines, as shown in Fig. 3.6(c,d). With this method, we can make in total 12 contacts to the sample, including gate electrodes.

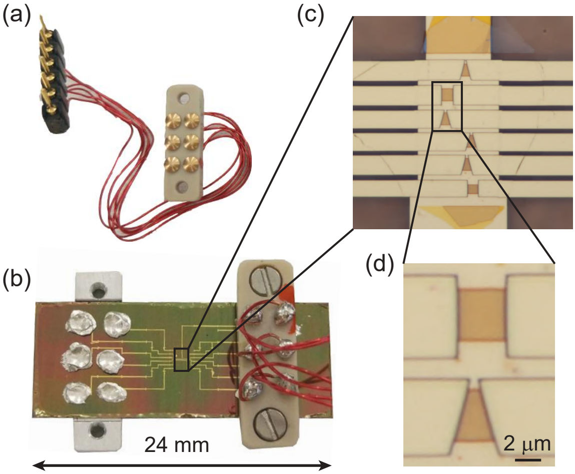

Figure 3.6. Electrical connection to the devices. (a) A typical electrical clamp with six pins. **(b)** Demonstration of clamping. First, indium pieces are placed on the contact pads, shown on the left side. Then the clamp is fixed with two screws to the substrate with the pins aligned to the indium pieces, shown on the right side. **(c,d)** Zoom-in to typical encapsulated devices.

3.3.2. Cryogenic measurement setup

The measurements of suspended samples presented in chapter 4 were performed in a cryostat with a variable temperature insert (VTI) having a base temperature of ∼1.5 K. All the other low temperature measurements were conducted using a home-built insert equipped with three-point bending setup, as shown in Fig. 3.7(a). The sample is mounted between the pushing-wedge and two counter-supports. The pushing-wedge is connected all the way up to the controlling knob with a rotating rod. A differential screw is used to make fine controls over the substrate bending. One full rotation of the controlling knob corresponds to a displacement of $\Delta z \approx 100\,\mu\text{m}$. The insert is

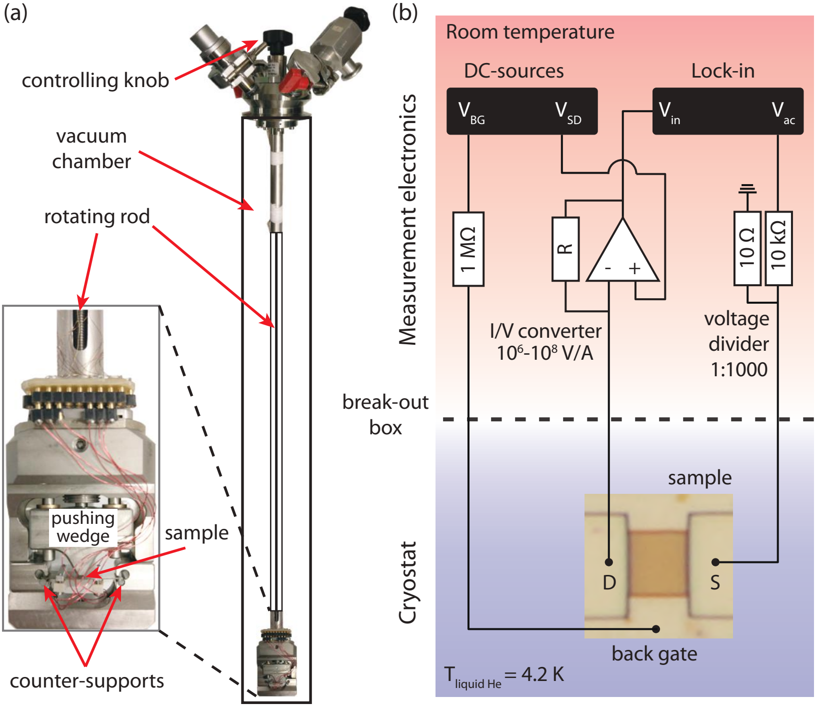
(a)
controlling knob
vacuum chamber
rotating rod
pushing wedge
sample
counter-supports
(b)
Room temperature
DC-sources
Lock-in
V_BG
V_SD
V_in
V_ac
Measurement electronics
1 MΩ
R
- +
10 Ω
10 kΩ
I/V converter
10⁶-10⁸ V/A
voltage divider
1:1000
break-out box
sample
D
S
Cryostat
back gate
T_liquid He = 4.2 K

Figure 3.7. Cryogenic measurement setup. (a) Home-built insert for studying strain effects in transport measurements. The inset shows the three-point bending setup. **(b)** Schematic of the setup for a typical voltage-biased differential conductance measurement at low temperature, with the most important components indicated. Schematic adapted from Ref. [148]

enclosed with a metallic tube, which is pumped into vacuum, see black box in Fig. 3.7(a). A tiny amount of helium gas is let in as exchange gas before cooling down. The tube is then immersed in liquid ^{4}He bath in a cryostat equipped with superconducting magnets. The base temperature for this setup is then ∼4.2 K. Since the insert was designed to be compatible for different cryostats, in principle all magnetic field configurations available in our lab can be applied to the sample, e.g. up to 9 T out-of-plane field or up to 4 T in-plane field.

Electrical connections from the clamps are made with twisted wire pairs to a break-out box at room temperature, which is then connected to measurement electronics with BNC cables. Differential conductance/resistance measurements were performed with standard low-frequency lock-in techniques[7]. In Fig. 3.7(b), the schematic of a typical measurement setup is shown. Home-built low-noise/low-drift I/V-converters and voltage amplifiers[8] were used for detecting the signals. For DC voltage sources, we used either a home-built low-noise/high-resolution DAC or a commercially available instrument (Yokogawa YK7651). A DC voltage was applied to the offset voltage of the IV-converter for bias measurements. Small magnetic fields required for weak localization and UCF measurements were generated using a Keithley 2400 source meter instead of the standard power supply for the superconducting magnets. All measurement instruments were communicated and controlled through RS232 or GPIB interfaces with LabView programs, Igor Pro scripts or Qcodes based on Python.

---

[7] Standford SR830 lock-in amplifier.

[8] Designed and made by the Electronics Lab at the Department of Physics, University of Basel.

4 Suspended multiterminal bilayer graphene and non-local signal

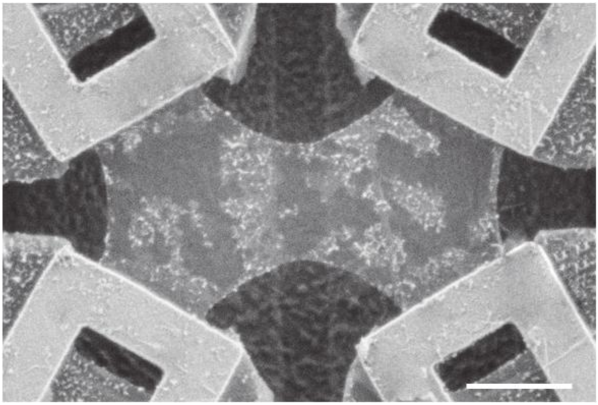

In this chapter, we investigate multiterminal suspended bilayer graphene devices [1]. Using in situ current annealing technique at low temperature, four-terminal bilayer graphene devices with reasonable quality have been achieved and measured. Tuning the charge carrier density by the bottom gates, an unexpected non-local signal larger than the ohmic contribution is observed near the charge neutrality point. With bias spectroscopy and temperature dependent measurements we try to understand the nature of the non-local signal. We discuss possible sources of the non-local signal, however, no solid conclusions can be drawn.

---

[1] A scanning electron microscope image of a partially current annealed suspended four-terminal bilayer graphene device. Resist residuals can still be seen on the graphene. The scale bar corresponds to 1 µm

4.1. Introduction

It has been introduced in section 2.1 that the valley degree of freedom in clean graphene is a good quantum number, implying the potential use for electronic applications, referred to as valleytronics, in a way similar to the role of spin in spintronics [149]. In order to address valley, ultraclean disorder-free graphene is a prerequisite. With in situ current annealing, which cleans the resist residues from fabrication process, ultraclean suspended graphene has been developed, yielding very high mobilities and ballistic transport over micron distances [141]. Secondly, one needs a handle to control valley for generating and detecting the valley current. As shown in section 2.3 that non-uniform strain configurations can generate pseudomagnetic fields that act with opposite signs on the two different valleys [45], we try to use strain as the handle to control the valley degree of freedom in graphene.

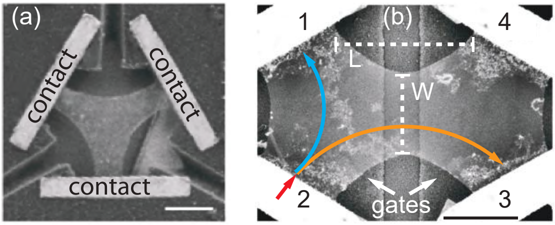

Figure 4.1. Device architectures and measurement mechanism. (a) SEM image of triangle-shaped graphene suspended symmetrically by contacts. **(b)** SEM image of the measured device, where two triangles are connected in order to perform non-local measurements. Resist residuals are not fully cleaned away by current annealing, especially near the contacts. The two bottom gates are connected together to act as one global gate in this experiment. The red arrow indicates the current injection. The blue (orange) arrow represents the path of K (K') valley polarized current. The scale bars correspond to 1 µm. $L \approx 2\,\mu\text{m}$ and $W \approx 1.1\,\mu\text{m}$.

One possible strain configuration has been proposed in Ref. [45] in order to generate a homogeneous pseudomagnetic field, where stresses need to be applied perpendicular to the perimeter of a triangular graphene flake. However, this strain configuration is still experimentally challenging. Instead, we start with a simplified variation, in which the three arms are fixed on the contacts, as shown in Fig. 4.1(a). The strain in graphene can be generated by pulling down the flake capacitively using an electric bottom gate and the strain configuration is determined by the triangular geometry. For this geometry, one can perform measurements based on the valley Hall effect (VHE) and the inverse valley Hall effect (IVHE), as introduced in section 2.3.2. In order to detect the valley Hall voltage, we connect a second triangular graphene as shown in Fig. 4.1(b). If a current is injected from the bottom-left contact, for example, electrons from K valley (blue) will go to the up-left contact while electrons from K' valley (orange) will bend to the right triangle. Then again in the second triangle, the K' electrons will bend to the right and go to the bottom-right contact resulting in a potential difference between the right two contacts. This potential difference can be detected by voltage measurements as a non-local signal.

The fabrication of suspended graphene devices is described in section 3.1.2. Our yield of suspending four-terminal devices is quite high (∼80%), but the challenging part is the current annealing. Usually only bilayer graphene can be successfully current annealed for multiterminal devices [150, 151]. We have tried to current anneal more than 20 monolayer devices and none of them was cleaned successfully. For bilayer devices, approximately 5 out of 10 devices were successfully cleaned with current annealing. The experiment presented in the following was conducted on a bilayer device. All measurements were performed at $T \approx 1.6\,\mathrm{K}$ using standard low-frequency lock-in techniques unless otherwise stated.

4.2. Local and non-local signal

First, we define $R_{\mathrm{a,b-c,d}} \equiv V_{\mathrm{cd}}/I_{\mathrm{ab}}$, where I_{ab} is the current passed from contact a to contact b and V_{cd} is the voltage probed between contact c and contact d. The local resistance R_{L} is measured as a function of gate voltage V_{g} with four different schemes which give very similar results, as shown in Fig. 4.2(a). A field-effect mobility of $\sim 150\,000\,\mathrm{cm^2\,V^{-1}\,s^{-1}}$ is extracted from a linear fit near the charge neutrality point (CNP) and a residual doping of $\sim 3 \times 10^9\,\mathrm{cm^{-2}}$ is estimated from a log-log plot of the conductance versus the carrier density [132]. The "shoulder" on the electron side might originate from the inhomogeneity of the device. The non-local resistance R_{NL} measured with two different schemes is plotted in Fig. 4.2(b), which also show almost identical results.

In Fig. 4.2(c), we compare R_{NL} with R_{L}. Interestingly, R_{NL} exhibits a much sharper peak than R_{L} around the CNP. The ohmic contribution to the non-local resistance due to current spread can be estimated by:

$$R_{\mathrm{ohmic}} = \frac{\rho}{\pi} e^{-\pi \frac{L}{W}}, \tag{4.1}$$

with ρ being the sheet resistance, W the width and L the length between the current path and the non-local voltage detection [152]. It is important to note that Eq. 4.1 is based on a Hall-bar geometry, which can only give an order of magnitude estimate in our case. The comparison of the measured R_{NL} with the

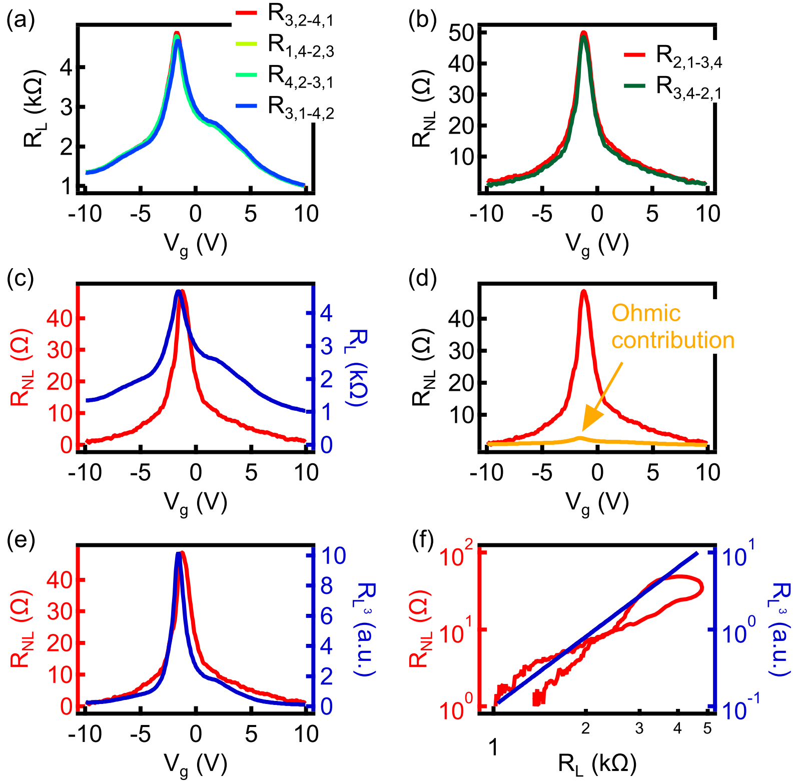

Figure 4.2. Measured local and non-local resistances R_L and R_NL: **(a)** Gate voltage dependence of R_L. **(b)** Gate voltage dependence of R_NL. **(c)** Comparison of the R_NL curve (red) with the R_L curve (blue). **(d)** Comparison of the non-local signal R_NL (red) with the calculated ohmic contribution (orange). **(e)** Shape comparison of the R_NL curve (red) with the R_L^3 curve (blue). **(f)** R_NL and R_L^3 plotted against R_L in logarithmic scale.

estimated ohmic contribution is shown in Fig. 4.2(d). It is clear that current spread alone cannot account for the large non-local resistance observed.

Here we try to investigate the valley Hall origin of the non-local signal. Other possible origins are discussed later in section 4.5. In Ref. [98–100], R_{NL} larger than ohmic contribution is also observed at zero magnetic field for both monolayer and bilayer graphene. They attribute it to the VHE and the IVHE due to the broken inversion symmetry, realized either by moiré superlattice (for monolayer) or by interlayer electric field with dual gating (for bilayer). The broken inversion symmetry opens a band gap at the CNP and gives rise to non-zero valley-contrasted Berry curvatures [153], which act effectively as magnetic fields in the momentum space that causes the Hall effect [154]. In the diffusive regime, the non-local resistance from this origin can be described by a power law relation [98–101]:

$$R_{\mathrm{NL}} \propto R_{\mathrm{L}}^3 \sigma_{\mathrm{xy}}^2 e^{-L/\lambda_{\mathrm{v}}} / \lambda_{\mathrm{v}}, \tag{4.2}$$

where σ_{xy} is the valley Hall conductivity and λ_{v} is the valley diffusion length. Figure 4.2(e) shows the comparison of R_{NL} with R_{L}^3. The curves are quite similar in shape except a small offset of the maxima. This offset might originate from device inhomogeneity [100]. In Fig. 4.2(f), R_{NL} (red) and R_{L}^3 (blue) are plotted as a function of R_{L} in logarithmic scale. The red line follows quite well the blue line, showing a good agreement with a cubic dependence. This seems to imply the valley Hall origin of the non-local signal. Compared to Ref. [98–100], however, we have neither superlattice nor an interlayer electric field induced by dual gating to break the inversion symmetry in our device. The non-local signal maximizes at the CNP, but the strain induced by capacitive coupling to the gate is minimum and negligible at this point [155]. Therefore, the non-local signal is unlikely an effect of the strain-induced pseudomagnetic field either.

4.3. Temperature dependence of local and non-local signal

Figure 4.3(a,b) present R_{L} and R_{NL} as a function of V_{g} for different temperatures. Although no insulating state is observed at the CNP down to $T \approx 1.6\,\mathrm{K}$, both R_{L} and R_{NL} show a strong temperature dependence. The temperature dependence at the CNP is very different from that at higher V_{g}. Both R_{L} and R_{NL} decrease very fast at the CNP with increasing temperature, which is reminiscent of a thermal activation behavior, suggesting the presence of a band gap. In contrast, at higher V_{g}, both R_{L} and R_{NL} increase slowly with increasing temperature, implying a metallic-like transport.

The Arrhenius-type plots of R_{L} and R_{NL} at the CNP are shown respectively in Fig. 4.3(c,d). The slope of the line fit to the linear part gives an estimate of the thermal activation energy, which yields $\sim$0.4 meV from R_{L} and $\sim$1.2 meV

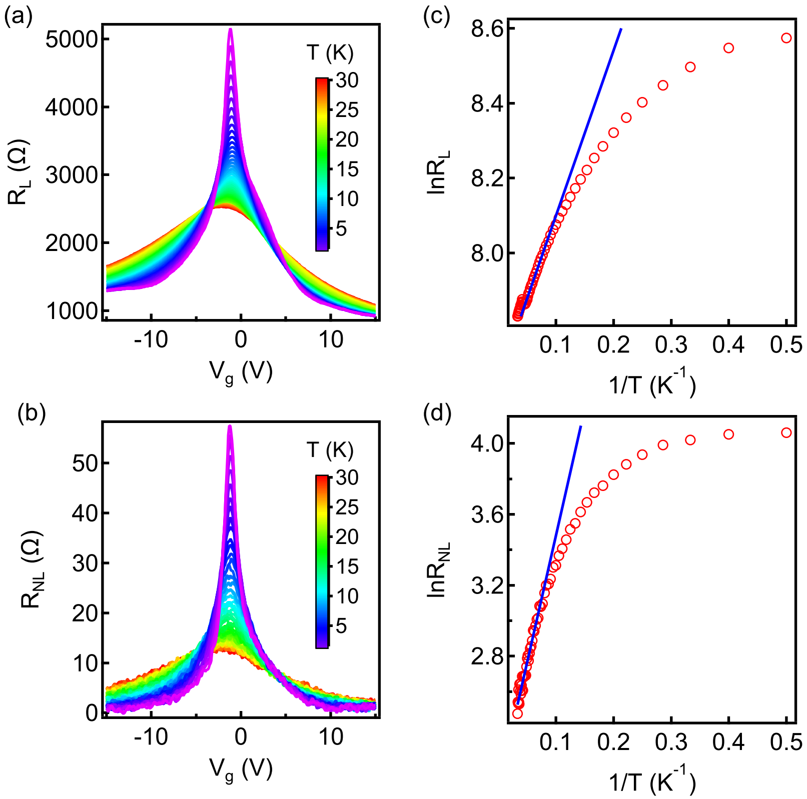

Figure 4.3. Temperature dependence of R_L and R_{NL}: The gate voltage and temperature dependence of the **(a)** local and **(b)** non-local resistance. There is no offset between traces. **(c,d)** Arrhenius-type plots of local and non-local resistances at the CNP. Red symbols are the experimental data and blue lines are the line fit to the linear part.

from R_{NL}. Both activation energies are orders of magnitude smaller than those achieved in Ref. [98–100] with inversion symmetry broken by external means. Interestingly, the activation energy extracted from R_{NL} is roughly triple of that from R_{L}, which is similar to the bilayer case with inversion symmetry broken by interlayer electric field [98]. The factor of three difference in the two activation energies already implies the non-linear relation between R_{NL} and R_{L} in our device. This observation is in stark contrast to the monolayer case with morié superlattice breaking the inversion symmetry, where both activation energies are similar [99].

Note, the electric field at the CNP is negligibly small in our device and is unlikely to induce a substantial layer asymmetry that results in a gap [156, 157]. One possibility could be the spontaneously gapped state in suspended bilayer graphene, which were reported previously in several studies [157–160]. In the following we use bias spectroscopy to gain more insights into the gap-like behavior.

4.4. Bias spectroscopy

The conductance map as a function of source-drain bias V_{sd} and gate voltage V_{g} is presented in Fig. 4.4(a), which shows a dip feature around zero V_{sd} bias for the CNP. Cuts at three different gate voltages are shown in Fig. 4.4(c), where different behaviors are observed for different regions. The conductance increases with bias at the CNP while the opposite is observe for regions away from the CNP. This observation is consistent with the temperature dependent measurements discussed in the previous section. Figure 4.4(b) shows the spectroscopy measurement at the CNP with out-of-plain magnetic field, where hint of the development of an insulating state with magnetic field is observed. Cuts at three different magnetic fields are shown in Fig. 4.4(d). The conductance drops rapidly with increasing magnetic field.

Compared to similar measurements in Ref. [157, 160], where both insulating and conducting phases were observed at the CNP in devices fabricated in the same way, our device belongs more likely to the conducting case. That means no spontaneously gapped state is present in our device. The reason why the insulating state is not always observed remains unclear [161]. In Ref. [150], this sample-dependent behavior has been attributed to the sample-dependent inhomogeneity of the device after current annealing. It has also been pointed out in Ref.[160] that increasing disorder has an effect similar to increasing temperature on the insulating state, which obscures the observation of the insulating state in experiments. The absence of the insulating state in our device might be related to the disorder due to the remaining resist residuals, as can be seen in Fig. 4.1(b).

In summary, although gap-like behavior is observed, the band gap is not

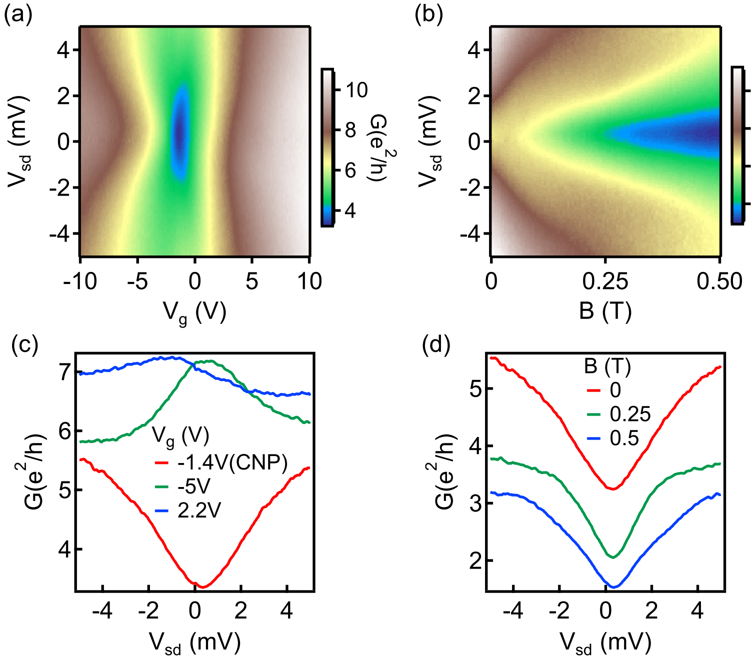

Figure 4.4. Bias spectroscopy: (a) Two-terminal differential conductance as a function of source-drain bias V_{sd} and gate voltage V_{g}. **(b)** Two-terminal differential conductance as a function of V_{sd} and out-of-plane magnetic field at the CNP. **(c)** Cuts for **(a)** at three different gate voltages. **(d)** Cuts for **(b)** at three different magnetic fields.

directly measured. We further current annealed the device, the conductance minimum dropped further but still remained finite (not shown here). Therefore, we could not conclude that the band gap is present in our device.

4.5. Discussion, conclusion and outlook

In Ref. [102], Zhang et al. shows theoretically that graphene can sustain a classical VHE with modest strain levels which can be detected in non-local transport measurements. Modest strain levels are defined as strain levels lower than those required for observing pseudo-Landau levels. Such strain levels may occur after current annealing in suspended devices, as reported in a recent study where built-in strain up to $\sim 4\%$ has been observed [162]. This mechanism could be a possible origin of our non-local signal.

Another possible origin is the edge current due to enhanced doping or additional conducting channels along the edge of graphene flakes, as reported in Ref. [150, 163–165]. Non-local signal larger than ohmic contribution is also observed on monolayer graphene Hall-bars [76], which also points to the direction of an enhanced doping along the edge.

In conclusion, we measured large non-local resistance in suspended bilayer graphene which cannot be explained by current spread. The valley Hall origin due to band gap was investigated, but no strong evidence was found. Further work is needed to fully clarify the origin of the large non-local signal observed. For example, a scanning technique to map the current distribution at the CNP would be helpful to determine the bulk or edge origin of the non-local signal. Or measurements at lower temperatures would help to investigate the presence of the gapped state at the CNP. Furthermore, low temperature Raman spectroscopy can directly determine the strain in the graphene and thus might help to justify the possibility of built-in strain induced VHE.

5 In situ strain tuning in graphene [1] [2]

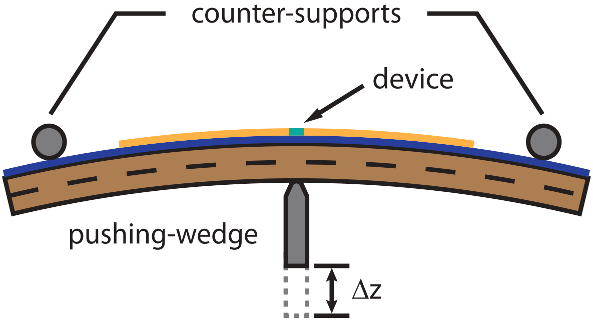

In this chapter we demonstrate deterministic and reproducible in situ strain tuning in graphene devices by bending a flexible substrate. The technique is first used for suspended graphene, then adapted for suspended encapsulated graphene and finalized with the on-substrate encapsulated graphene approach. The full hBN encapsulation preserves the exceptional quality of pristine graphene for transport experiments. In addition, the on-substrate approach allows one to exploit strain effects in the full range of possible sample geometries and at the same time guarantees that changes in the gate capacitance remain negligible during the deformation process. We use Raman spectroscopy to spatially map the strain magnitude in devices with two different geometries and demonstrate the possibility to engineer a strain gradient, which is relevant for accessing the valley degree of freedom with pseudomagnetic fields. Comparing the transport characteristics of a suspended device with those of an on-substrate device, we demonstrate that our new approach does not suffer from the ambiguities encountered in suspended devices.

---

[1] Raman measurements on suspended samples in this chapter are done in collaboration with Jan Overbeck and Oliver Braun.

[2] Parts of this chapter have been published in a similar form in Ref. [166]. © 2019 American Chemical Society

5.1. Introduction

A series of intriguing effects were predicted for strained graphene, such as the appearance of a scalar potential [44], pseudomagnetic fields [44–46], valley filtering [47, 48] or superconductivity [49]. Different methods have been introduced to generate strain in graphene. One common approach is based on suspended graphene, where strain is induced by using different microactuators [120, 167–169] or by simply bending a flexible substrate [170]. In other approaches, graphene is not suspended and strain can be generated by bending a flexible substrate [115], by using highly stressed metallic pads [171], or by placing graphene on periodic structures [172–174]. However, several challenges that need to be overcome simultaneously hampered the progress of these platforms for studying strain effects in transport experiments. First, complex fabrication usually significantly degrades the graphene quality and hinders the observation of the strain effects. In addition, the device is often limited to very basic structures, without the possibility of local gating or multi-terminal devices. Second, mechanical deformations often result in changes in the gate capacitance that cannot be easily distinguished from the actual strain effects. The third challenge is that the strain should be in situ tunable and non-hysteretic to disentangle strain effects from other effects.

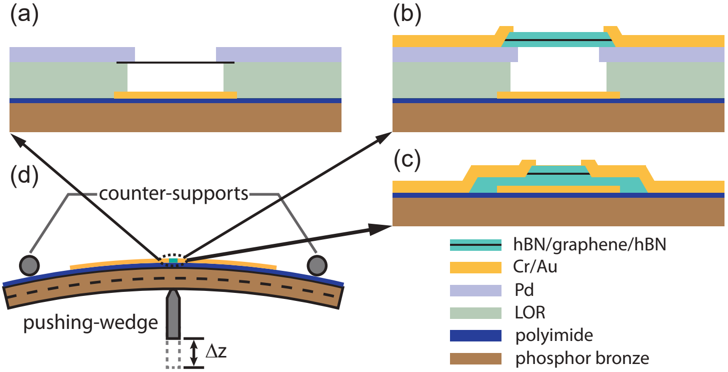

Figure 5.1. Schematic cross sections: (a) suspended graphene device, **(b)** suspended encapsulated graphene device, **(c)** on-substrate encapsulated graphene device and **(d)** three-point bending setup. The bending is described by the displacement of the pushing-wedge, Δz.

In this chapter we first demonstrate deterministic strain tuning in three different types of devices, i.e. suspended graphene, suspended encapsulated graphene and on-substrate encapsulated graphene. The schematic cross sections of them are shown in Fig. 5.1(a-c), respectively. Fabrication details of these devices are given in section 3.1. Bending the flexible substrate in a three-point bending setup, as illustrated in Fig. 5.1(d), generates strain in the graphene. The deformation of the substrate is determined by the displacement Δz of the pushing-wedge relative to the mounting position. Second, we compare the first low temperature transport characteristics of a suspended encapsulated device with those of an on-substrate encapsulated device and conclude that the latter meets all the above requirements for studying strain effects in transport experiments.

5.2. Strain tuning in suspended graphene

The schematic cross section of the device is illustrated in Fig. 5.1(a), where a graphene flake is suspended over an electrical bottom gate on a polyimide coated metal plate. A typical suspended device is shown in Fig. 5.2(a). Usually ripples can be observed, suggesting built-in strain in the graphene which is confirmed by the Raman measurements later. Figure 5.2(b) shows a device broke after fabrication while Fig. 5.2(c) shows the device broke after strain measurements. One can easily see the differences.

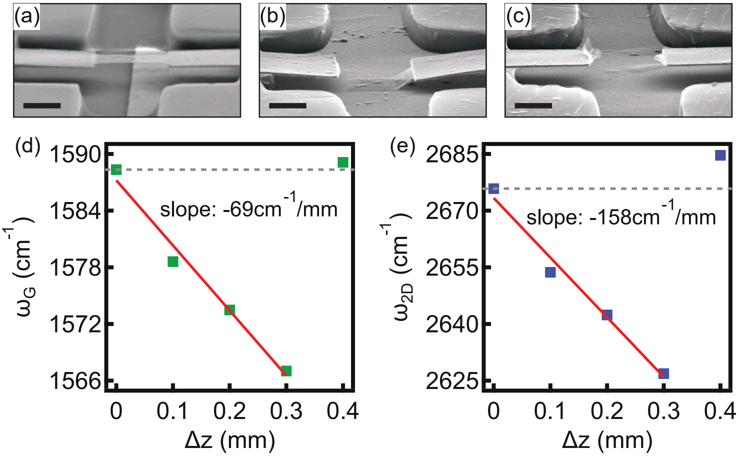

Figure 5.2. SEM images of suspended graphene devices and Raman measurements. **(a)** A suspended device after fabrication. **(b)** A broken device after fabrication. **(c)** A broken device after strain experiment. The scale bars correspond to 1 µm. **(d)** $\bar{\omega}_G$ and **(e)** $\bar{\omega}_{2D}$ plotted as a function of Δz. The red lines are linear fits. The grey dashed lines are guides to the eye.

Previous studies reported characteristic redshifts in the Raman peaks of graphene [115–117], which we now use to quantify the local strain generated in our devices. For small strain values, both the G peak and the 2D peak can be fitted by a single Lorentzian with center frequency ω_{G} and ω_{2D} [115], respectively. To investigate strain tuning, we acquire Raman spectra at the center of the device for different Δz. The extracted ω_{G} and ω_{2D} are plotted for a series of increasing Δz in Fig. 5.2(d,e), respectively. From $\Delta z = 0\,\mathrm{mm}$ to $0.3\,\mathrm{mm}$, both ω_{G} and ω_{2D} shift to lower values, indicating increasing strain in the graphene sheet. The corresponding strain value of a $\Delta\omega_{\mathrm{2D}} \approx -49\,\mathrm{cm}^{-1}$ is $\sim 0.91\%$, which is obtained using $\partial\omega_{\mathrm{2D}}/\partial\varepsilon = -54\,\mathrm{cm}^{-1}/\%$ from theoretical calculations [89]. We note that the shift rate is not known very accurately and our choice is among the intermediate reported values [89, 115–120]. Since the bending of the substrate is small and the device size is more than three orders of magnitude smaller than the size of the substrate, one can assume the induced strain in graphene increases linearly with Δz. We then fit the data with a linear function and the corresponding slopes are shown as annotations in Fig. 5.2(d,e). The ratio of the ω_{2D} slope to the ω_{G} slope is ~ 2.3, which confirms strain as the origin of the redshift of the Raman peaks [169, 175–177]. The data points at $\Delta z = 0.4\,\mathrm{mm}$ jump to higher values, suggesting the rupture of the device. Compared with the first data point, we estimate the built-in strain to be $\sim 0.16\%$ after fabrication.

5.3. Strain tuning in suspended encapsulated graphene

For transport experiments, clean graphene is required. Current annealing suspended graphene is a possible way to make graphene exceptionally clean [141], but the combination with strain tuning is very challenging. An alternative to get clean graphene is to encapsulate it with hBN [138], which preserves the exceptional quality of pristine graphene for transport experiments. The device also becomes much more robust due to encapsulation. Since generation of tunable strain by bending a flexible substrate has been demonstrated for suspended graphene in section 5.2, in this section we apply this method to suspended encapsulated graphene and investigate strain tuning in such suspended stacks.

The schematic cross section of this type of devices is illustrated in Fig. 5.1(b). One-dimensional edge contacts [138] are used to contact the graphene instead of two-dimensional top contacts. We use exfoliated graphene from natural graphite and usually choose $\sim$20 nm thick hBN for the top layer and $\sim$30 nm thick hBN for the bottom layer. A typical fabricated device is shown in the inset of Fig. 5.3. We performed Raman measurements at the center of the stack for different Δz, the same way as for suspended graphene samples. The extracted 2D peak center frequency ω_{2D} is plotted as a function of Δz in

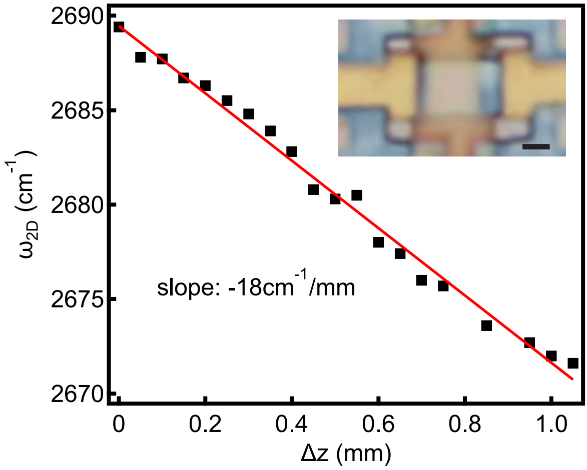

Figure 5.3. Raman measurements of a suspended encapsulated device: $\bar{\omega}_{2D}$ plotted as a function of Δz. The red line is a linear fit. The inset is a micrograph of the measured device. The scale bar corresponds to 1 µm.

Fig. 5.3. A shift of roughly $-18\,\mathrm{cm}^{-1}$ is achieved for ω_{2D} at $\Delta z = 1\,\mathrm{mm}$, corresponding to a strain of $\sim 0.33\%$. It is surprising that the edge contacts can sustain such amount of strain. We then fit the data linearly and a slope of $-18\,\mathrm{cm}^{-1}/\mathrm{mm}$ is obtained, which is almost one order of magnitude smaller than that for suspended graphene (see Fig. 5.2(e)). The reduced straining efficiency can be attributed to the thickness of the stack (tens of nm), which is orders of magnitude larger than that of monolayer graphene.

In summary, we have demonstrated that it is possible to tune the strain in graphene even when it is encapsulated. Transport measurements have been done on such devices as well (see section 5.4.6), but a gate capacitance change occurs due to the bending-induced change in the graphene-to-gate distance, which makes it very difficult to separate strain effects from other effects.

5.4. Strain tuning in on-substrate encapsulated graphene

Since the encapsulation already protects graphene from resist residuals during fabrication, the suspension is actually not necessary anymore for the purpose of clean graphene. We therefore simplify the fabrication and directly strain the van der Waals (vdW) heterostructure on-substrate, as shown schematically in Fig. 5.1(c). We use spatially resolved Raman spectroscopy to demonstrate that our method is versatile and allows one to engineer various strain fields, such as strain gradients, which are important for the generation of pseudomagnetic fields [44]. We also show that the edge contacts work reliably and can sustain strain up to $\sim 1\%$. The metallic contacts and the gate allow us to perform transport experiments while tuning the strain in situ. In the first low-temperature electron transport measurements, we demonstrate that our method solves the problem of the gate capacitance change due to a bending-induced change in the graphene-to-gate distance, which occurs in suspended graphene devices. Therefore, our approach of on-substrate encapsulated graphene offers an ideal platform for studying strain effects in transport experiments.

5.4.1. Device design for different strain fields

The metallic contacts are essential for generating strain in a vdW heterostructure. In section 5.4.4, we present a comparison between devices with and without contacts. The result shows that strain cannot be induced by substrate bending in devices without contacts. Based on the assumption that the graphene sheet is pulled uniaxially by the contacts during the bending of the substrate, we designed devices with two different geometries in order to obtain different strain fields. This is illustrated in Fig. 5.4(a), where the rectangle (device A) is expected to result in a homogeneous strain field, while the trapezoid (device B) should exhibit a strain gradient along the y-axis, i.e. perpendicular to the straining axis. An optical micrograph of two fabricated devices is shown in Fig. 5.4(b).

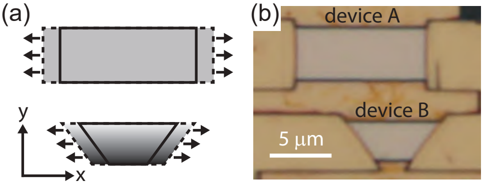

Figure 5.4. (a) Illustration of the mechanism for different strain fields. The solid lines represent devices without strain while the dashed lines stand for strained devices. The arrows indicate the elongation of the device along the contacts. The magnitude of strain is shown in grayscale with black corresponding to large strain. **(b)** Micrograph of two typical devices with different geometries.

5.4.2. Strain fields mapping with spatial Raman spectroscopy

Typical Raman spectra of encapsulated graphene are shown in Fig. 5.5(d) for two different Δz. The zoomed-in to the hBN peak and the graphene G and 2D peaks are shown in Fig. 5.5(a-c), respectively. The bending of the substrate results in a redshift of all peaks, with the most prominent effect on the graphene 2D peak. In the following, we use spatially resolved Raman spectroscopy to map the strain field based on the redshift of the graphene 2D peak. The same analysis for the hBN Raman peak is presented in section 5.4.3, which shows that both hBN and graphene are strained similarly in this method.

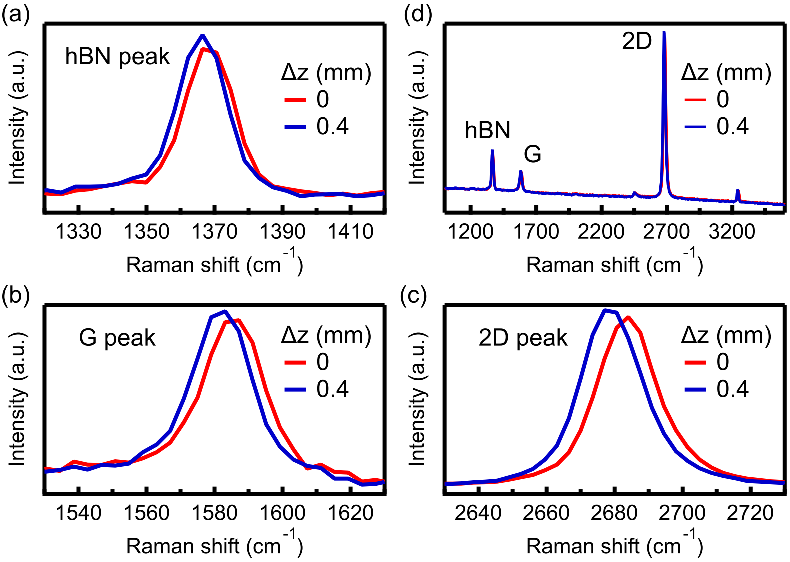

Figure 5.5. Raman spectra: Typical Raman spectra of an encapsulated device for two different Δz, zoomed in to **(a)** the hBN peak, **(b)** the graphene G peak and **(c)** 2D peak, respectively.

We first focus on the investigation of the rectangular device A. In Fig. 5.6a-g, ω_{2D} is plotted as a function of position for device A, for a series of increasing Δz from 0 mm to 0.6 mm (straining) and then decreasing back to 0 mm (relaxing), as indicated by the gray arrows. With increasing Δz, ω_{2D} shifts to lower values at all positions on the map, consistent with increasing strain everywhere in the graphene sheet. When Δz is decreased back to 0 mm, ω_{2D} reverts back to the initial values. The mean value $\bar{\omega}_{2D}$ averaged over the whole device is plotted as a function of Δz in Fig. 5.7(a), where Δz is first increased from 0 mm to 0.6 mm then decreased back to 0 mm. The very symmetric V-shape reveals a linear dependence and a good reproducibility of the strain tuning in the graphene device and exhibits no significant hysteresis. This process was repeated several times (up to 8 cycles) and no degradation was observed. The corresponding average strain values ($\bar{\varepsilon}$) are shown on the right axis, which are calculated using $\partial\omega_{2\mathrm{D}}/\partial\varepsilon = -54\,\mathrm{cm}^{-1}/\%$ [89] with $\omega_{2D} \approx (2685 \pm 4.4)\mathrm{cm}^{-1}$ for unstrained graphene. The latter value is obtained as the average over 10 Raman spectra measured at different positions on three different hBN/graphene/hBN stacks before fabrication. The strain values at $\Delta z = 0\,\mathrm{mm}$ are not 0, probably due to the intrinsic strain accumulated in the device after fabrication. We obtain an average strain of up to 0.23% and a maximum strain near the contacts of 0.3% for device A at $\Delta z = 0.6\,\mathrm{mm}$. Figure 5.8(c) shows the plot of $\bar{\omega}_{2\mathrm{D}}$ versus $\bar{\omega}_{\mathrm{G}}$ (center frequency of the graphene G peak) of both devices for different Δz values. The data points fall on a line of slope 2.2, which confirms strain as the origin of the redshift of the Raman peaks [169, 175–177].

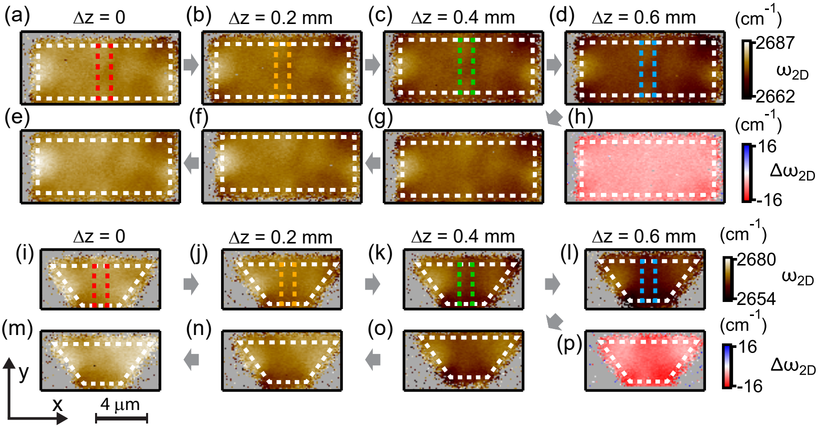

Figure 5.6. Spatial Raman maps. (a-g) Spatially resolved Raman maps of $\omega_{2\mathrm{D}}$ for device A at different Δz values. The white dashed lines outline the device boundaries and the colored dashed boxes mark the positions of the profiles shown in Fig. 5.8. The gray arrows show the sequence of the measurements. **(h)** Spatially resolved Raman maps of $\Delta\omega_{2\mathrm{D}}$ for device A, obtained by subtracting map (a) from map (d). **(i-o)** Spatially resolved Raman maps of $\omega_{2\mathrm{D}}$ for device B at different Δz values. **(p)** Spatially resolved Raman maps of $\Delta\omega_{2\mathrm{D}}$ for device B, obtained by subtracting map (i) from map (l).

We note that there is a small inhomogeneity in the map of $\omega_{2\mathrm{D}}$ for device A in Fig. 5.6(a) which does not change significantly with external straining. We analyze the data in a scatter plot of ω_{2D} versus ω_{G} in the appendix B, which shows that the inhomogeneity in the maps of ω_{2D} originates mostly from the strain variation over the large device area [175–178]. The homogeneity of the externally induced strain field can be seen directly in Fig. 5.6(h), which shows a map of the *change* in the Raman shift, $\Delta\omega_{\mathrm{2D}}$, between the map at $\Delta z = 0.6\,\mathrm{mm}$ (Fig. 5.6(d)) and the map without external straining (Fig. 5.6(a)). For this rectangular geometry, the externally induced strain is fairly homogeneous in the bulk with a vanishing strain gradient, which matches quite well the expected strain fields for device A as shown in Fig. 5.4(a). The detailed strain pattern for this geometry from finite element method (FEM) simulations is shown in the appendix B.

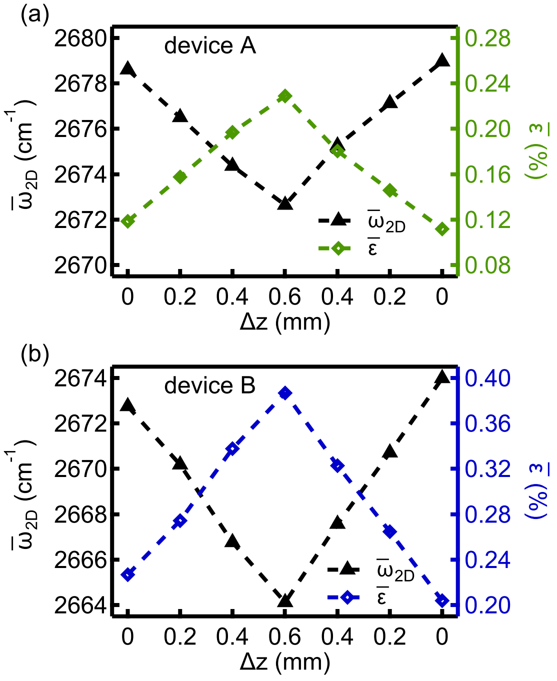

Figure 5.7. Averaged values over the maps. $\bar{\omega}_{\mathrm{2D}}$ and the corresponding strain values plotted as a function of Δz for **(a)** devices A and **(b)** device B.

We now turn to the investigation of strain and strain gradients in the trapezoidal device B. The spatially resolved maps of ω_{2D} for device B are plotted in

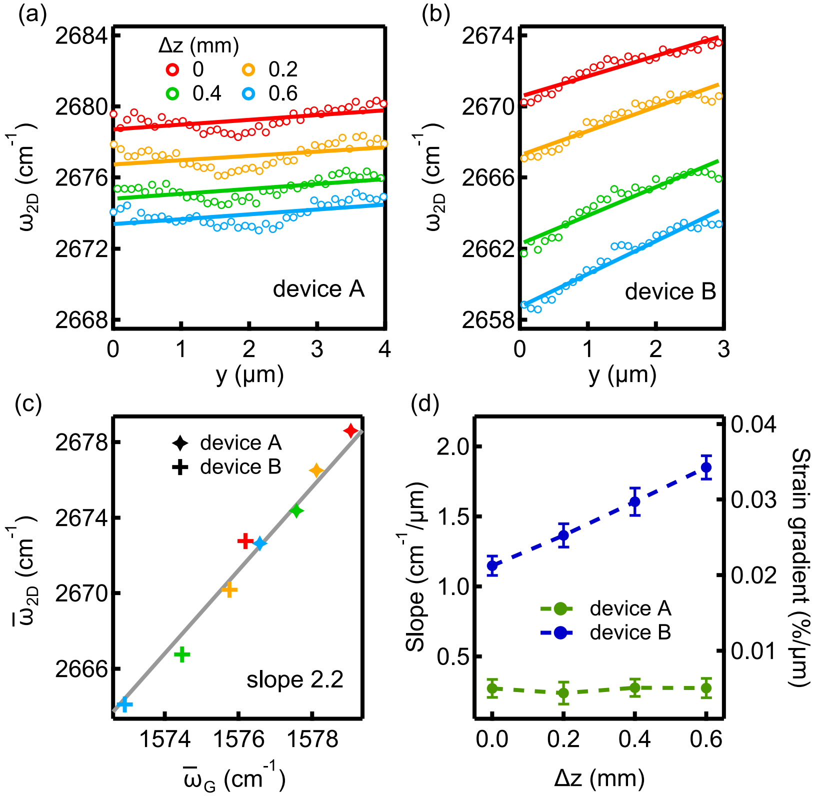

Figure 5.8. Profiles of the maps. (a,b) Profiles at the center of the maps indicated in Fig. 5.6 for $\Delta z = 0\,\mathrm{mm}$ (red), 0.2mm (orange), 0.4mm (green), 0.6mm (blue). Open circles are data, solid lines are linear fit. **(c)** $\bar{\omega}_{2D}$ versus $\bar{\omega}_G$ at different Δz for both devices, the grey line has a slope of 2.2. **(d)** Slopes of the profiles plotted as a function of Δz. The slopes are extracted from linear fitting in **(a)** and **(b)**. The error bars are the fitting errors. The corresponding strain gradient is shown on the right axis.

Fig. 5.6(i-o) for the same series of Δz as above for sample A. Also this device shows a tunable average strain controlled by Δz. The device averaged $\bar{\omega}_{\mathrm{2D}}$ and the corresponding extracted strain values are plotted in Fig. 5.7(b) as a function of Δz. At identical Δz values, the average strain for device B is larger than that for device A due to the smaller size of device B, but shows a similar V-shape, i.e. a linear, non-hysteretic dependence on Δz. These findings can also be seen directly in the Raman maps. We obtain an average strain of up to 0.38% and maximum values at the lower sample edge of 0.52% for device B at $\Delta z = 0.6\,\mathrm{mm}$. The existence of a strain gradient is visible in Fig. 5.6(j-l). At the shorter (bottom) edge of the device, ω_{2D} shows a stronger shift than that at the longer (top) edge, which matches the predicted strain pattern for a trapezoidal geometry, as illustrated in Fig. 5.4(a) (see also the FEM simulations in in the appendix B). Figure 5.6(p) shows the difference between the Raman signals at large bending (Fig. 5.6(l)) and no bending (Fig. 5.6(i)).

To demonstrate the deterministic generation of a strain gradient in more detail, we plot ω_{2D} for both devices in Fig. 5.8(a,b) as a function of the position along the y-axis in the center of the device area, averaged over 1 µm in the x-direction, as indicated by the colored dashed boxes in Fig. 5.6(a-d) and (i-l). For both devices we find a clear increase in the average strain (overall shift of the curves) and an essentially unchanged background variation with increasing Δz. In addition, for the trapezoidal geometry (device B) we find a clear linear increase in the strain when moving from the longer to the shorter sample edge.

We now take the average slope of these curves as an estimate of the large scale (non-microscopic) strain gradient along the y-axis. For this purpose we plot in Fig. 5.8(d) the slopes of linear fits to the data in Fig. 5.8(a) (device A) and Fig. 5.8(b) (device B) as a function of Δz, with the right axis showing the corresponding extracted strain gradient. The small non-zero slope for device A stems from the small intrinsic strain variation over the large device area discussed above and stays constant for increasing Δz. In contrast, for device B we find a linear dependence of the average slope on the Δz, demonstrating that strain gradients can be generated by modifying the device geometry. The pseudo-magnetic field (B_{ps}), as introduced in section 2.3.1, depends on the strain gradients [44, 45],

$$B_{\mathrm{ps}} = \frac{\hbar\beta}{ea}\left[-2\frac{\partial\varepsilon_{\mathrm{xy}}}{\partial x} - \frac{\partial(\varepsilon_{\mathrm{xx}} - \varepsilon_{\mathrm{yy}})}{\partial y}\right], \tag{5.1}$$

with $\beta \approx 3.37$ the Grüneisen parameter [43] and $a = 1.42\,\text{Å}$ the interatomic distance. To estimate B_{ps}, we use

$$B_{\mathrm{ps}} \approx \frac{\hbar\beta}{ea}\frac{\partial\varepsilon_{\mathrm{xx}}}{\partial y}, \tag{5.2}$$

and obtain values on the order of 10 mT in the bulk of device B at $\Delta z = 0.6\,\mathrm{mm}$. We note that much larger strain gradients occur near the corners of the device, which might result in local pseudo-magnetic fields larger than 100 mT. We also point out that larger average strain values can be achieved in this setup (see section 5.4.5), but with an increased probability of device failure, which happens at a strain on the order of 1%.

5.4.3. Raman maps of hBN peak

In this section we plot the center frequency of the hBN Raman peak, ω_{hBN}, as a function of position for device A and device B. The displacement Δz is first increased from 0 mm to 0.6 mm and then decreased back to 0 mm, as indicated by the gray arrows. The ω_{hBN} shifts to lower values with increasing Δz at all positions on the map for both devices, consistent with increasing strain everywhere in the hBN [179]. The ω_{hBN} reverts back to the initial values, when Δz is decreased back to 0 mm, demonstrating a good reversibility of the strain tuning. In device A, the externally induced strain is fairly homogeneous in the bulk with no strain gradient, as shown in Fig. 5.9(a). In device B, ω_{hBN} shows a larger red-shift on the bottom edge than on the top edge, demonstrating an externally induced strain gradient, as shown in Fig. 5.9(b). These results are consistent with those extracted from the graphene 2D peak in section 5.4.2.

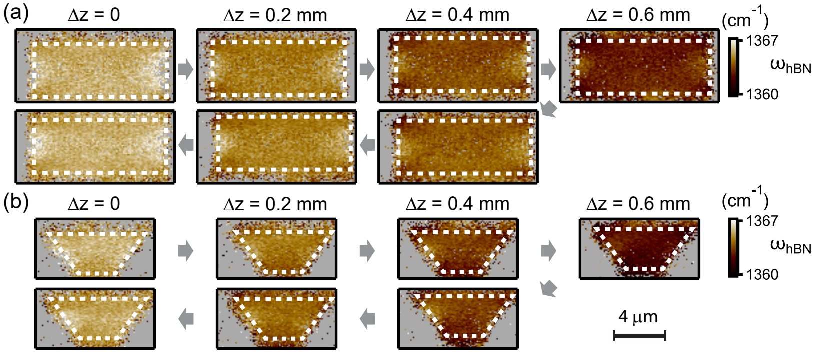

Figure 5.9. Raman maps of hBN peak. (a) Spatially resolved Raman maps of ω_{hBN} for device A at different Δz values. The white dashed lines outline the device boundaries and the gray arrows show the sequence of the measurements. **(b)** Spatially resolved Raman maps of ω_{hBN} for device B.

5.4.4. Clamping of edge contacts

Here we compare the devices with edge contacts to devices without any contacts in Raman measurements. The micrograph of the devices are shown in

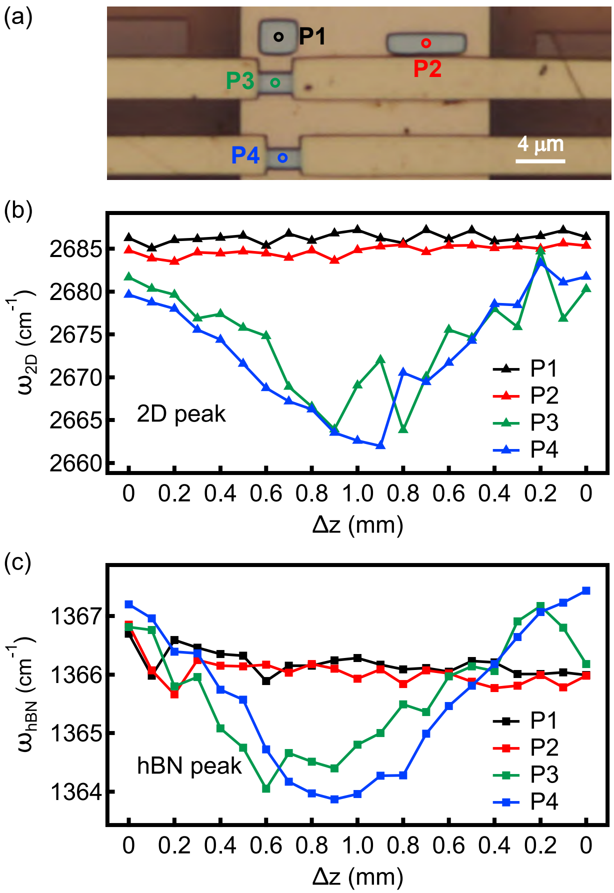

Figure 5.10. Comparison between devices with and without contacts. (a) Micrograph of the sample with two devices without contacts (P1, P2) and two devices with contacts (P3, P4). The circles mark the laser spot positions for the Raman measurements. **(b)** Center frequency ω_{2D} of the graphene 2D peak plotted as a function of Δz for all four devices. **(c)** Center frequency ω_{hBN} of the hBN peak plotted as a function of Δz for all four devices.

Fig. 5.10(a). During the measurements, the substrate bending, Δz, is first increased to 1 mm and then decreased back to 0 mm in steps. In Fig. 5.10(b), the ω_{2D} of device P3 and P4 shows the V-shape behavior, revealing a linear dependence and a good reversibility of the strain tuning in the contacted devices, similar to the devices shown in section 5.4.2. The fluctuations on the curves can be attributed to the relative shift of the laser spot between each measurement and the not fully homogeneous strain within the device. In contrast, ω_{2D} in the devices P1 and P2 do not show any dependence on Δz, suggesting no strain induced in these devices by bending the substrate. Similar results are observed in the hBN Raman peak, as shown in Fig. 5.10(c). These results demonstrate that the contact clamping is essential for generating strain in encapsulated devices.

5.4.5. Edge contact failure

Here we show a typical straining sequence leading to contact failure of a device at large bending. In Fig. 5.11(a-c), ω_{2D} shifts to lower values with increasing Δz for the whole device area, as expected for an externally induced strain in the graphene. After a critical amount of bending, here around 0.9 mm, the ω_{2D} does not redshift with increasing bending, but instead blueshifts. This indicates a failure of the mechanical contact to the metal. This process is gradual as one can see in Fig. 5.11(d,e). When the contact failure happens, the electrical contact resistance increases dramatically. The average strain achieved in this device is about 0.7% before the contact failure.

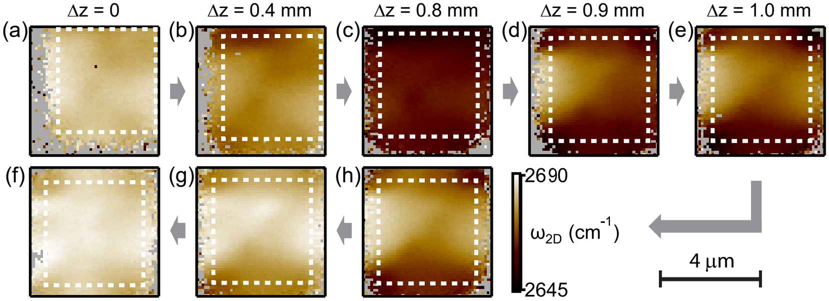

Figure 5.11. Demonstration of contact failure: spatially resolved Raman maps of ω_{2D} for a rectangular device at different Δz values. The white dashed lines outline the device boundaries and the gray arrows show the sequence of the measurements.

5.4.6. First transport measurements

One of the major advantages of our technique is that the edge contacts not only act as clamps for the mechanical deformation, but also allow for simultaneous transport experiments. Here we show the first low-temperature (4 K) transport experiments with in-situ strain tuning of a device fabricated in the described fashion and compare the results to similar measurements on a device where the encapsulated graphene is suspended, using the LOR based suspension technique [134, 135]. The two experiments are shown schematically in Fig. 5.12(a-b). For both devices the two-terminal differential conductance, G, is measured as a function of the gate voltage, V_g, for different Δz values using standard low-frequency lock-in techniques (see Fig. 5.12(c,e)).

There are significant differences between suspended and on-substrate devices for bending experiments. For the suspended device one can immediately find a systematic change of the curves in gate voltage with increasing Δz (see Fig. 5.12(c)), while such an obvious effect is absent for the on-substrate device (see Fig. 5.12(e)). The effects found in the suspended device can be fully accounted for by the change in the graphene-to-gate distance when bending the substrate, as depicted in Fig. 5.12(a). This is illustrated in Fig. 5.12(d), where we plot the data of Fig. 5.12(c) rescaled linearly in gate voltage for each curve with $V_\mathrm{g} = 0\,\mathrm{V}$ as a fix point. This can be understood in a simple capacitor model in which the charge induced in the graphene are given by $Q = CV_\mathrm{g}$, with C the effective capacitance between the graphene layer and the gate. If the capacitance is changed by a factor α to αC due to the substrate bending, the same charge Q is induced at V_g/α, which is equivalent to a rescaling in the gate voltage. This scaling factor is extracted for each curve by matching the CNP to that of the curve at $\Delta z = 0\,\mathrm{mm}$ and it is linear in Δz. After rescaling, all data points fall onto the same curve, see Fig. 5.12(d). This demonstrates that the bending-induced gating effect is dominant for the suspended graphene device, which makes it very difficult to study effects due to actual strain.

This effect is absent in the on-substrate devices optimized for strain tuning. For comparison, we performed the same type of measurements also on an on-substrate device, with the results shown in Fig. 5.12(e). Since the gate voltage lever arm in this device is much larger than that for the suspended device due to the shorter graphene-to-gate distance, we apply smaller gate voltages to obtain a similar carrier density range as that in the data of the suspended device (see top axes of Fig. 5.12(d,e)). An electron mobility of $\sim 100\,000\,\mathrm{cm}^2\,\mathrm{V}^{-1}\,\mathrm{s}^{-1}$ is extracted from a linear fit around the CNP, suggesting a high graphene quality in our device. On this gate voltage scale and also on much larger scale (see inset of Fig. 5.12(e)), all curves with different Δz values are virtually identical, which demonstrates that there are no bending-induced changes in the carrier density or in the contact resistance in this experimental configuration. The additional conductance minimum at $V_\mathrm{g} \approx 1.3\,\mathrm{V}$ comes from

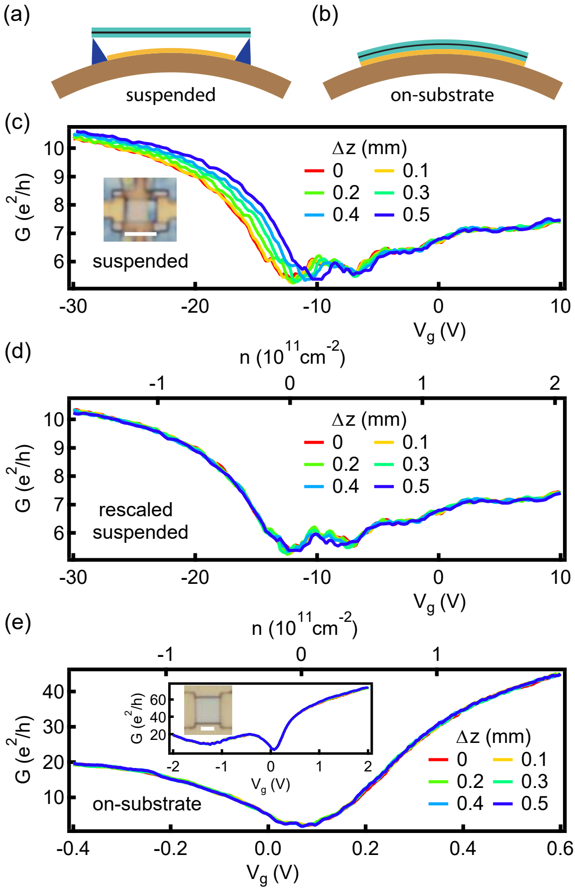

Figure 5.12. Low temperature transport measurements. (a,b) Illustration of substrate bending for suspended and on-substrate devices, respectively. **(c)** Two-terminal differential conductance, G, plotted as a function of gate voltage, V_g, for a suspended device for different Δz values. The inset is the micrograph of the measured device. **(d)** The same data as in **(c)** with the curves rescaled in V_g with respect to $V_\mathrm{g} = 0\,\mathrm{V}$ by matching the CNP of each curve with that of the curve at $\Delta z = 0$. The corresponding carrier density is shown on the top axis. **(e)** G of an on-substrate device for a similar charge carrier density range for different Δz values. The inset shows G on a larger V_g range. The micrograph is the measured device. The scale bars correspond to $2\,\mu\mathrm{m}$.

a double moiré superlattice effect in encapsulated graphene [180]. We point out that on this scale of graphene straining we could not detect significant changes in the conductance.

5.5. Conclusion and outlook

In conclusion, we have successfully generated tunable strain in suspended graphene, suspended encapsulated graphene and on-substrate encapsulated graphene devices. For the on-substrate encapsulated devices, it allows us to design a large variety of device geometries. As an example, we use spatially resolved Raman imaging to demonstrate that the edge contact clamping and rectangular geometry result in a fairly homogeneous straining of the graphene. In a second step, we use this design freedom to generate a strain gradient in a trapezoidal geometry. In first transport experiments we then demonstrate another major advantage of on-substrate encapsulated devices, namely that the bending-induced gate capacitance change can be avoided, which is crucial for studying strain effects in transport experiments. This approach is not limited to graphene, but also suitable for studying strain effects in other 2D materials and complex vdW heterostructures, for example in MoS_2 [181–183]. Because our method is simple and intuitive, nonetheless allowing complex device structures, we expect that it will pave the way towards deterministic strain engineering and new approaches to valleytronics.

6 Mobility enhancement in graphene by in situ reduction of random strain fluctuations[1]

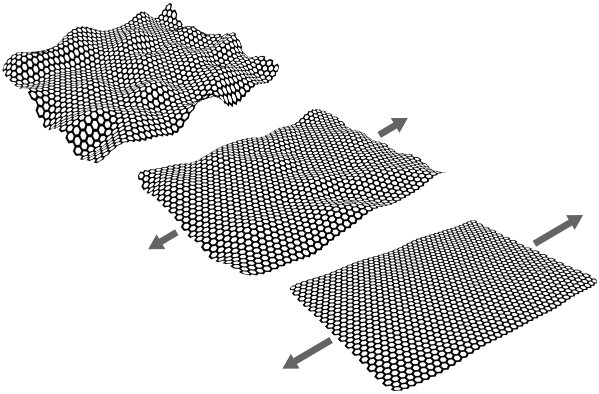

Microscopic corrugations are ubiquitous in graphene even when placed on atomically flat substrates. These result in random local strain fluctuations limiting the carrier mobility of high quality hBN-supported graphene devices. In this chapter we present transport measurements in hBN-encapsulated devices where such strain fluctuations can be in situ reduced by increasing the average uniaxial strain. When $\sim 0.2\%$ of uniaxial strain is applied to the graphene, an enhancement of the carrier mobility by $\sim 35\%$ is observed while the residual doping reduces by $\sim 39\%$. We demonstrate a strong correlation between the mobility and the residual doping, from which we conclude that random local strain fluctuations are the dominant source of disorder limiting the mobility in these devices. Our findings are also supported by Raman spectroscopy measurements.

---

[1] This chapter has been published in a similar form in Ref. [184]. © 2020 American Physical Society

6.1. Introduction

In the first generation of graphene devices, where SiO_2 was used as the substrate, it is commonly believed that random charged impurities at the substrate surface are the dominant source of disorder limiting the device quality [59–65]. One way to improve the device quality is to suspend graphene to spatially separate it from the charge traps [131–135]. Nowadays, a more widely used technique is to place graphene on hexagonal boron nitride (hBN) [18, 136–138], which is atomically flat and expected to be free of surface charge traps. A significant improvement in device quality has been achieved, exhibiting very high carrier mobilities, enabling the observation of a series of new physical phenomena, such as the fractional quantum Hall effect [185–187], transverse magnetic focusing [69, 70, 188] and various moiré superlattice effects [35–37, 180]. Although the mobility of hBN-supported graphene devices is generally higher than that of the SiO_2-supported, the reported mobility values vary over a large range, suggesting another mechanism that limits the mobility. It has been pointed out that random strain fluctuations (RSFs) in graphene could be a dominant source of disorder leading to electron scattering [66]. In a recent statistical study of many devices on hBN substrates, a clear correlation between the carrier mobility μ and the residual doping n_0 was found, pointing to RSFs as the dominant microscopic source of scattering [67]. The residual doping caused by charge fluctuations manifests in a broadening of the resistance peak around the charge neutrality point (CNP), as introduce in section 2.2.2. Similar results have been found as well in bilayer graphene [189].

Ripples and pronounced corrugations can form naturally in graphene due to its two-dimensional nature, as, for example, demonstrated by transmission electron microscopy in suspended graphene membranes [190]. In stacked layers, microscopic corrugations can spontaneously form during exfoliation due to thermal fluctuations at room temperature [66, 191, 192]. These corrugations might persist through the fabrication processes and give rise to RSFs in the final device. In SiO_2-supported devices, nanometer-scale ripples have been observed in scanning probe microscopy studies [193–196] and their effects on electron transport have been reported in weak localization studies [15, 197, 198]. Although the hBN surface is typically much flatter, height fluctuations are still present in hBN-supported graphene devices [136], which can result in RSFs. These RSFs have been confirmed in Raman spectroscopy measurements [176, 199].

In this chapter we demonstrate in a direct experiment that RSFs can be the mechanism limiting the mobility of encapsulated devices. We compare the transport characteristics of individual devices before and after increasing the average uniaxial strain, which directly reduces the strain fluctuations in the same device. In Fig. 6.1(a) the RSFs in graphene lattice are illustrated, which we believe can be reduced gradually by increasing the average strain, as

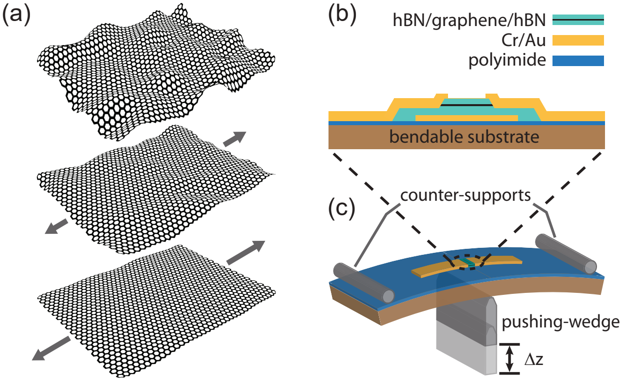

Figure 6.1. Demonstration of in situ reduction of strain fluctuations. **(a)** Illustration of strain fluctuations and the effects of increasing average strain. The arrows indicate the direction and the strength of the externally induced strain by substrate bending mediated by contacts. **(b,c)** Schematics of the device cross section and the three-point bending setup. The bending of the substrate is determined by the displacement of the pushing-wedge, Δz.

indicated by the arrows. The reduction of the RSFs due to increasing average strain is further confirmed by directly probing the RSFs using Raman spectroscopy [176]. This not only allows us to determine the dominant microscopic mechanism, but also to actually increase the mobility of the device.

6.2. Experimental setup and fabrication

The setup of the experiment is shown schematically in Fig. 6.1(b,c). It allows us to tune the average uniaxial strain in hBN-encapsulated graphene devices by bending a flexible substrate [166]. The displacement Δz of the pushing-wedge relative to the mounting position determines the deformation of the substrate and is used to tune the average strain in the graphene. Details of the sample fabrication and the setup for strain generation are given in chapter 5.

6.3. Field-effect measurements and mobility extraction

To investigate the effects of average strain on the transport characteristics of graphene, we measure the two-terminal differential conductance G as a function of the gate voltage V_g for different Δz values, as plotted in Fig. 6.2(a). The measurements were performed at low temperature ($T = 4.2\,\mathrm{K}$) using stan-

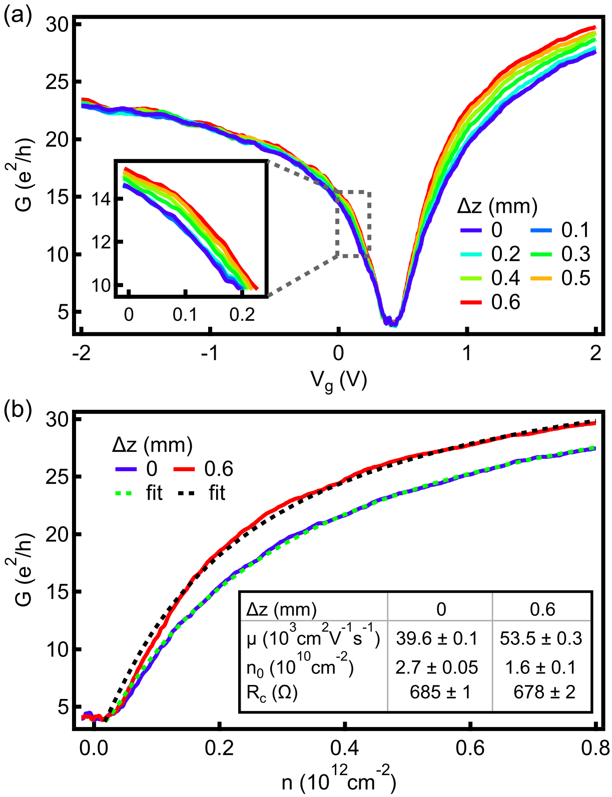

Δz (mm)	0	0.6
μ (10^3 cm^{2}V^{-1}s^{-1})	39.6 ± 0.1	53.5 ± 0.3
n_0 (10^{10} cm^{-2})	2.7 ± 0.05	1.6 ± 0.1
R_c (Ω)	685 ± 1	678 ± 2

Figure 6.2. Field-effect measurements and mobility extraction. (a) Two-terminal differential conductance G plotted as a function of gate voltage V_g for different Δz values. The slope of the curves becomes steeper for larger Δz, for both the electron and hole side. The inset shows a zoom-in to the hole side. **(b)** G versus n for two different Δz on the electron side. The fits according to Eq. 6.1 are shown as dashed lines for $\Delta z = 0$ and 0.6 mm, respectively, with the fitting parameters given in the table.

dard low-frequency lock-in techniques. The CNP is at $V_\mathrm{g} = 0.4\,\mathrm{V}$, indicating an offset p-doping in our device. The conductance of the graphene increases faster when gated away from the CNP for larger Δz, suggesting an increase in field effect mobility with increasing Δz. This effect is reversible when Δz is decreased (see appendix C). A displacement of $\Delta z = 0.6\,\mathrm{mm}$ corresponds to $\sim 0.2\%$ of average strain, which is determined from Raman measurements shown later [166]. The conductance starts to saturate at higher gate voltages because of the contact resistance. On the hole side (p-doping), a p-n junction forms near each contact due to the n-doping from the contact, resulting in a sightly larger contact resistance and a lower saturation conductance, which renders the mobility-change less visible. The zoomed-in data in the inset of Fig. 6.2(a) shows qualitatively the same effect as for the electron side.

To quantitatively evaluate the effects of strain tuning on the electrical properties of graphene, we fit each curve on the electron side (n-doping) with the following formula based on the Drude model [65, 136], as introduced in section 2.2.2:

$$G = \frac{1}{\frac{\alpha}{e\mu\sqrt{n^2+n_0^2}} + R_\mathrm{c}}, \tag{6.1}$$

where e is the elementary charge and α is the geometry factor describing the aspect ratio, which is 1.28 in this case (see appendix C). The fitting parameters are the charge-carrier density independent mobility μ, the residual doping n_0 around the CNP and the contact resistance R_c. The charge-carrier density n is calculated from the applied gate voltage V_g with a lever arm of $5.13 \times 10^{11}\,\mathrm{cm^{-2}\,V^{-1}}$ using a parallel plate capacitor model. The thickness of the bottom hBN, which is the gate dielectric, is determined by atomic force microscopy. Two examples of the fitting are shown as dashed lines for $\Delta z = 0$ and $0.6\,\mathrm{mm}$ in Fig. 6.2(b) with the corresponding parameters given in the inset.

6.4. Analysis of fitting results

The fitting results for μ and n_0 are plotted as a function of Δz in Fig. 6.3(a,b), respectively. The mobility μ shows a clear increase with increasing Δz, while n_0 decreases significantly. The change is slower in the beginning, which might be attributed to a small mechanical hysteresis of the bending setup. The extracted contact resistance R_c (including $\sim 350\,\Omega$ line resistance) is shown in the inset of Fig. 6.3(c) and is essentially unaffected by the bending, demonstrating the mechanical robustness of the device for these levels of applied average strain [166]. The mobility increases gradually from $\sim 40\,000\,\mathrm{cm^2\,V^{-1}\,s^{-1}}$ to $\sim 54\,000\,\mathrm{cm^2\,V^{-1}\,s^{-1}}$ when Δz is increased from 0 to 0.6 mm. At the same time the residual doping drops gradually from $\sim 2.7 \times 10^{10}\,\mathrm{cm^{-2}}$ ($\Delta z = 0$) to $\sim 1.6 \times 10^{10}\,\mathrm{cm^{-2}}$ ($\Delta z = 0.6\,\mathrm{mm}$). The ($\mu$, n_0) pairs are plotted as $1/\mu$ versus

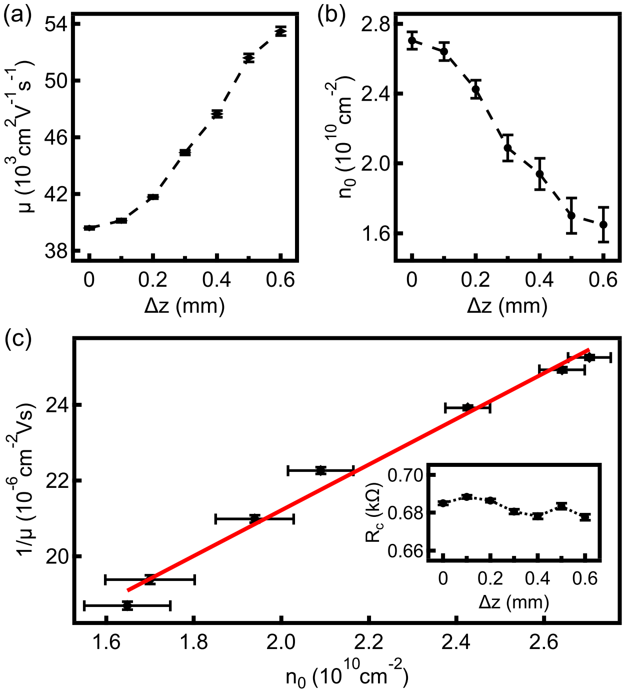

Figure 6.3. Fitting results. **(a)** Extracted field effect mobility μ and **(b)** residual doping n_0 values from fitting plotted as a function of Δz on the electron side. The error bars are the standard errors from fits. The mobility μ shows an increase with increasing Δz while n_0 shows a decrease. **(c)** Data of **(a)** and **(b)** plotted as $1/\mu$ versus n_0, showing a clear linear relation. The red line is a linear fit to the data with $1/\mu = (0.146 \pm 0.007) \times (h/e)n_0 + 1/\mu_0$ and $\mu_0 \approx 110\,000\,\text{cm}^2\,\text{V}^{-1}\,\text{s}^{-1}$. The inset shows the extracted contact resistance R_c (including $\sim$350 Ω line resistance) for different Δz.

n_0 in Fig. 6.3(c), clearly demonstrating the proportionality between $1/\mu$ and n_0. The same analysis is performed for the hole side and similar results are obtained with a larger contact resistance (see appendix C), which is consistent with the interpretation that the p-n junction makes the effect less pronounced on the hole side.

Since the graphene is encapsulated with hBN, it is very unlikely that the small applied average strain changes the charged impurities at the graphene-hBN interfaces, ruling them out as dominant mechanism for the observed mobility increase. An artificial effect due to the change of the gate capacitance with strain is also ruled out [166], because the CNP appears at the same gate voltage for all Δz values.

RSFs have been identified theoretically as a possible source of disorder limiting charge carrier mobility [66]. Strong evidence of this mechanism has been found in a statistical study involving many devices, where a clear linear relation between $1/\mu$ and n_0 was observed, with $1/\mu \approx 0.118 \times (h/e) n_0$ [67]. Moreover, a detailed microscopic mechanism was proposed in which the variation of n_0 was attributed to RSFs-induced scalar potentials, while the limitation in μ was attributed to randomly varying pseudomagnetic fields [67]. Fitting our data linearly in Fig. 6.3(c) yields $1/\mu = (0.146 \pm 0.007) \times (h/e) n_0 + 1/\mu_0$ and $\mu_0 \approx 110\,000\,\mathrm{cm^2\,V^{-1}\,s^{-1}}$. It shows a similar slope ($\sim 0.146 \times (h/e)$), allowing us to draw two conclusions. First, the charge carrier mobility is limited by RSFs and second, the control of the average strain allows us to control the RSFs and hence the mobility. The offset $1/\mu_0$ might imply another mobility limiting mechanism when RSFs are not dominating anymore. The value $\mu_0 \approx 110\,000\,\mathrm{cm^2\,V^{-1}\,s^{-1}}$ nearly coincides with the mobility of the devices, in which no mobility enhancement due to increasing average strain is observed (see section 6.7).

Theoretically both, in-plane and out-of-plane, strain fluctuations can contribute to this effect [67]. In a previous study of weak localization on SiO_2-supported graphene devices [198], a reduction of the phase coherence time τ_ϕ was found for an increasing in-plane magnetic field. It has been attributed to an enhanced dephasing rate due to a random vector potential generated by the in-plane magnetic field penetrating out-of-plane corrugations in the graphene layer. Similar effects have been observed in encapsulated devices [200, 201], strongly suggesting that out-of-plane corrugations are also present in encapsulated graphene. We therefore attribute the mobility increase in our experiment to the reducing of out-of-plane strain fluctuations, as illustrated in Fig. 6.1(a).

6.5. Raman measurements

To further substantiate our findings, we use spatially resolved Raman spectroscopy to directly probe the RSFs at room temperature. For small uniaxial

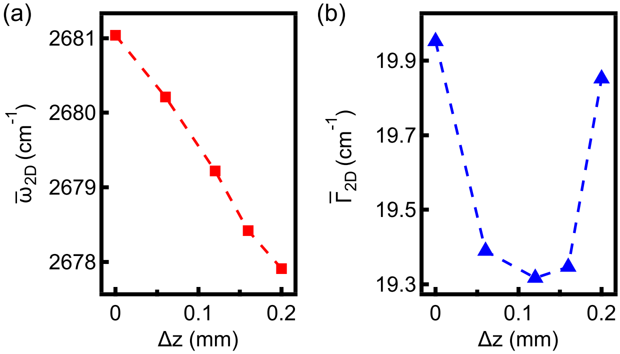

Figure 6.4. Raman measurements. **(a)** Spatially averaged center frequency $\bar{\omega}_{2D}$ of the Raman 2D peak for different Δz, showing a linear decrease with increasing Δz, which suggests an increasing average strain. **(b)** Spatially averaged linewidth $\bar{\Gamma}_{2D}$ of the Raman 2D peak as a function of Δz, exhibiting a nonmonotonic characteristics with a minimum of $\sim$19.3 cm^{-1}.

strain, which is the case in our experiment, the graphene Raman 2D peak can be fitted by a single Lorentzian [115], with a center frequency ω_{2D} and linewidth Γ_{2D}. As introduced in section 2.3.3, the center frequency ω_{2D} redshifts with increasing strain, while the linewidth Γ_{2D} broadens due to the splitting of the 2D peak [89, 118]. It has been shown that nanometer-scale strain inhomogeneities within the laser spot ($\sim$500 nm) also broadens the 2D peak [176], originating from averaging over regions with different local strain and hence different ω_{2D}. Therefore, Γ_{2D} can be used to probe the RSFs. We perform spatially resolved Raman spectroscopy and extract maps of ω_{2D} and Γ_{2D} for different Δz. The mean value of the center frequency $\bar{\omega}_{2D}$ averaged over the whole device is plotted as a function of Δz in Fig. 6.4(a). It shifts linearly to lower values with increasing Δz, indicating an increasing average strain in the graphene sheet [115]. The $\sim$3 cm^{-1} shift at $\Delta z = 0.2$ mm corresponds to an externally induced average strain of $\sim 0.06\%$ [166]. In Fig. 6.4(b) the averaged value of the 2D peak linewidth $\bar{\Gamma}_{2D}$ is plotted as a function of Δz, showing nonmonotonic characteristics with a minimum of $\sim$19.3 cm^{-1} at $\Delta z = 0.12$ mm. It first decreases with increasing Δz before increasing again, which can be explained by the competition between the two broadening mechanisms. The initial value of $\bar{\Gamma}_{2D}$ ($\sim$20 cm^{-1}) is larger than the intrinsic linewidth ($\sim$17 cm^{-1}) of the 2D peak [176], indicating that RSFs are present in our graphene. We attribute the decrease of $\bar{\Gamma}_{2D}$ to a reduction of the RSFs due to the externally applied strain, as illustrated in Fig. 6.1(a). When the broadening of the 2D peak induced by the increasing average strain dominates, $\bar{\Gamma}_{\mathrm{2D}}$ increases again with increasing Δz.

6.6. Weak localization measurements

To investigate the characteristic scattering times on this device, we performed weak localization measurements. Figure 6.5(a) shows the low-field magnetoconductivity for different V_{g} around $V_{\mathrm{g}} = 1\,\mathrm{V}$ for $\Delta z = 0$. A narrow dip in conductivity is observed around $B = 0$, which is a signature of weak localization. Conductance fluctuations induced by random interference are also visible, which are suppressed by ensemble-averaging over a small V_{g} range around the target V_{g} value [67, 200]. The averaged curve obtained in this way

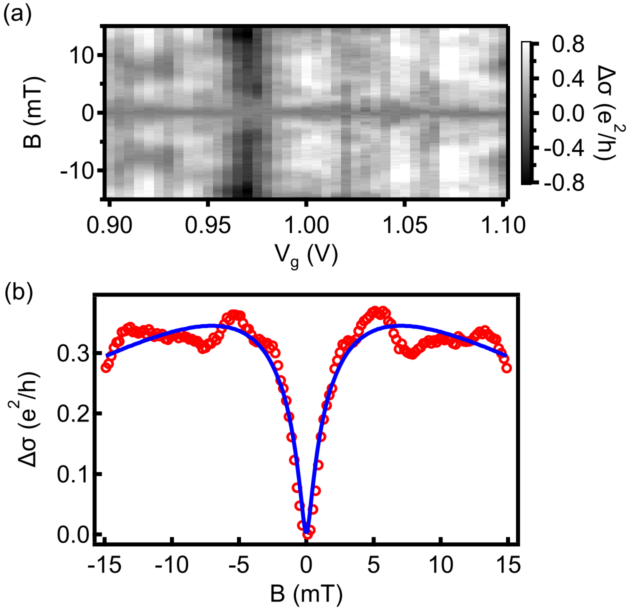

Figure 6.5. Weak localization measurements. (a) Magnetoconductivity as a function of out-of-plane magnetic field B and gate voltage V_{g} measured at $T = 4.2\,\mathrm{K}$ for $\Delta z = 0$. A clear feature is observed around $B = 0$. **(b)** Magnetoconductivity averaged over all traces at different V_{g}. The red circles represent data that have been ensemble-averaged and the blue line is the fit to the theory of weak localization in graphene.

is shown in Fig. 6.5(b) as red circles. We fit the data with the equation from the weak localization theory for graphene [58]:

$$\Delta\sigma(B) = \frac{e^2}{\pi h}\left[F\left(\frac{\tau_{\mathrm{B}}^{-1}}{\tau_\phi^{-1}}\right) - F\left(\frac{\tau_{\mathrm{B}}^{-1}}{\tau_\phi^{-1}+2\tau_{\mathrm{iv}}^{-1}}\right) - 2F\left(\frac{\tau_{\mathrm{B}}^{-1}}{\tau_\phi^{-1}+\tau_{\mathrm{iv}}^{-1}+\tau_*^{-1}}\right)\right], \tag{6.2}$$

where $F(z) = \ln(z) + \Psi(0.5 + 1/z)$, with $\Psi(x)$ the digamma function, $\tau_{\mathrm{B}}^{-1} = 4eDB/\hbar$ and $D = v_F^2\tau/2$. The fitting parameters are the phase coherence time τ_ϕ, the intervalley scattering time τ_{iv} and the intravalley scattering time τ_*. The elastic scattering time $\tau = {\sim}2.6 \times 10^{-13}\,\mathrm{s}$ is determined from the carrier mobility and is not a fitting parameter here. The fitted curve is plotted as blue solid line in Figure 6.5(b) with the results $\tau_\phi = (9.9 \pm 0.5) \times 10^{-12}\,\mathrm{s}$, $\tau_{\mathrm{iv}} = (5.8 \pm 0.6) \times 10^{-12}\,\mathrm{s}$ and $\tau_* = (2.8 \pm 0.2) \times 10^{-13}\,\mathrm{s}$.

The intervalley scattering time τ_{iv} is much longer than the elastic scattering time τ, implying that the mobility is not limited by intervalley scattering processes (scattering on short-range potentials, e.g. defects, edges). In contrast, the intravalley scattering time τ_* (the time needed to break the effective single-valley time-reversal symmetry) is nearly identical to τ, pointing to RSFs-induced random pseudomagnetic fields as the main factors limiting the mobility [67]. For charged impurities, it has been argued that $\tau_* \gg \tau$ [67], which is not the case here.

6.7. Device without mobility enhancement

We have observed a clear increase in the mobility with increasing average strain in more than 5 devices. Their mobility values varies from ~30 000 $\mathrm{cm^2\,V^{-1}\,s^{-1}}$ to ~80 000 $\mathrm{cm^2\,V^{-1}\,s^{-1}}$. Another example is presented in the appendix C. In Fig. 6.3(a), there is also an indication that the mobility starts to saturate when it approaches higher values. For the devices with a mobility larger than ~80 000 $\mathrm{cm^2\,V^{-1}\,s^{-1}}$, the mobility-increase effect is absent. One example is shown in Fig. 6.6, where the mobility does not increase with increasing Δz. The mobility value is above 100 000 $\mathrm{cm^2\,V^{-1}\,s^{-1}}$, which is beyond the highest value of the studied range in Ref. [67]. The absence of the mobility-increase effect in this device suggests that either the strain fluctuations cannot be fully reduced by increasing the average strain or another scattering mechanism becomes relevant for ultra high mobility devices.

6.8. Conclusion and outlook

In conclusion, we have demonstrated an in situ reduction of the RSFs in individual encapsulated graphene devices by increasing the average strain. In

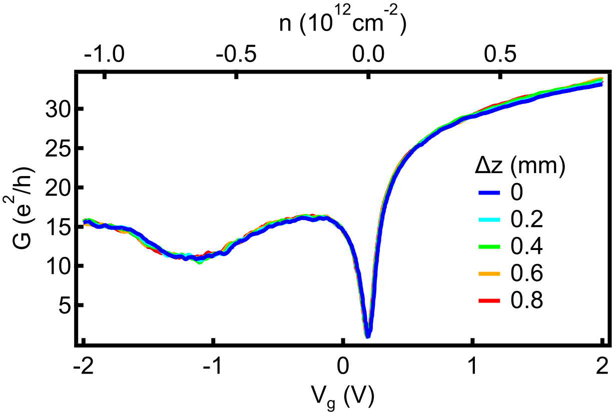

Figure 6.6. Device without mobility enhancement. Two-terminal differential conductance G measured as a function of gate voltage V_g for different Δz. The corresponding carrier density is shown on the top axis.

low-temperature transport measurements, an enhancement of the carrier mobility by $\sim 35\%$ is observed while the residual doping reduces by $\sim 39\%$ when $\sim 0.2\%$ of average strain is applied to the graphene. The linear correlation between $1/\mu$ and n_0 reveals that RSFs are the dominant scattering mechanism. These findings are further substantiated by Raman spectroscopy, in which the 2D peak linewidth Γ_{2D}, first decreases with increasing average strain before the average strain induced broadening dominates. The in situ straining allows us to directly compare results on individual devices and to avoid statistics over different devices. Using this technique we have directly confirmed that RSFs are the dominant scattering mechanism limiting the mobility in most hBN-supported graphene devices. For devices with even higher mobilities, either the reduction of RSFs is not possible, or another scattering mechanism becomes dominant.

7 Strain effects in transport experiments [1]

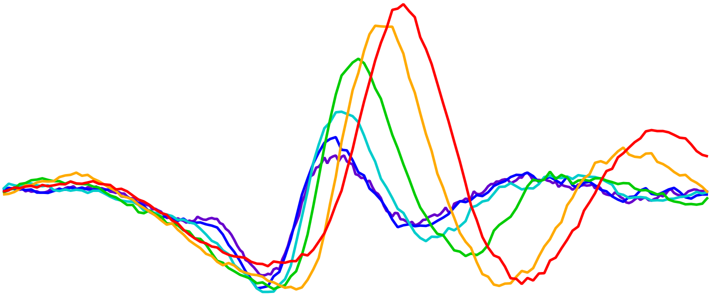

In this chapter, we present strain effects in various transport experiments of high-quality encapsulated graphene devices and discuss possible interpretations. First, the strain setup and the design of device geometries are briefly recapitulated. Second, the strain-induced scalar potential is demonstrated in experiments, followed by conductance fluctuations measurements, where evidence of pseudomagnetic field is found. Then, the stain effects in transverse magnetic focusing is discussed, where Fermi velocity renormalization might be involved for explanation. Furthermore, strain effects in quantum Hall regime are shown, where the device geometry makes a big difference. Further experimental and theoretical investigations are required to fully understand the strain effects there.

---

[1] Parts of this chapter are in preparation for publication.

7.1. Introduction

Due to the mechanical flexibility of graphene, strain can be used to alter its electronic properties [7, 21, 43, 87]. A scalar potential [44, 92], and/or a vector potential/pseudomagnetic field (PMF) [44–46, 86, 202] can be induced by different strain fields, as introduced in section 2.3.1. Various STM studies of strain effects in graphene have been reported [172, 173, 203–207]. However, such strain effects have not been so much explored in transport experiments due to several challenges, such as the limitation of sample quality or the lack of in situ tunability of the strain [171, 173, 208]. Formation of ripples in the graphene or changes of the gate capacitance during straining also hinders the observation of strain effects [170, 209]. We have developed a straining method that not only resolves all the challenges mentioned above, but also enables engineering of different strain fields [166], the details of which can be found in chapter 5. The key innovation of our method is the combination of in situ straining with the full hBN encapsulation of graphene, which preserves the exceptional graphene quality for transport experiments.

In this chapter we present various transport experiments while the strain in the graphene is in situ tuned. First, we briefly recapitulate the straining method and the device designs for different strain fields. Then the conductance measurements as a function of gate voltage at zero magnetic field are presented, where a shift of the CNP in gate voltage with increasing strain is observed. This shift can be quantitatively explained by a global strain-induced scalar potential. After that, experiments in small magnetic fields are shown, where systematic strain effects are found and discussions on possible interpretations are given. Furthermore, strain effects in the quantum Hall regime are presented and discussed.

7.2. Strain setup and device geometries

The mechanism of generating strain in encapsulated graphene is shown schematically in Fig. 7.1(a,b), where a three-point bending setup is used to bend a flexible substrate. The induced strain in graphene is controlled by the bending of the substrate, which is determined by the displacement Δz of the pushing-wedge relative to the mounting position. The edge contacts to graphene act as clamps for strain generation and at the same time as electrodes for transport measurements. It has been shown in chapter 5 that the edge contacts work reliably up to a strain value of $\sim 1\,\%$ and different strain fields can be achieved by modifying the device geometry. In this chapter we study strain effects on two types of devices, as shown in Fig. 7.1(c,d). Device type A has a square geometry, which is intended for generating a homogeneous strain field, while device type B is trapezoidal, where a strain gradient in y-direction is expected, as indicated by grayscale with higher strain on the shorter side. The strain gradient is required for generating PMF.

All transport measurements were performed at liquid helium temperature ($T \approx 4.2\,\mathrm{K}$) using standard low-frequency lock-in techniques.

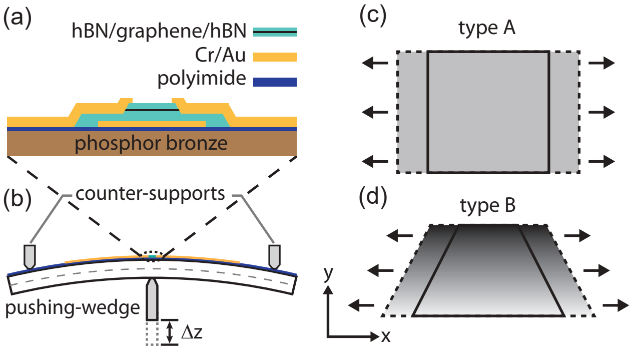

Figure 7.1. Strain setup and device geometries. Schematic cross section of **(a)** the device and **(b)** the bending setup. The displacement Δz of the pushing-wedge controls the bending of the substrate and thus the induced strain in graphene. **(c,d)** Illustration of device geometries designed for generating different strain fields, with the square for a homogeneous strain field and the trapezoid for a strain gradient in y-direction. The solid lines stand for unstrained devices while the dashed lines represent devices with strain. The elongation of the devices is indicated by the arrows along the contacts and the strain magnitude is shown in grayscale.

7.3. Strain-induced scalar potential

The two-terminal differential conductance G of a square device (Sample1 A) is measured as a function of gate voltage V_g for different Δz, as shown in Fig. 7.2(a). No significant strain effects can be seen on this scale. With a linear fit around the CNP, a charge-carrier mobility of $\sim 100\,000\,\mathrm{cm}^2\,\mathrm{V}^{-1}\,\mathrm{s}^{-1}$ is extracted, suggesting a high device quality. The mobility enhancement effect discussed in chapter 6 is absent, because in such high mobility devices the carrier mobility is not limited by random strain fluctuations. The additional conductance minimum at $V_\mathrm{g} \approx 1.2\,\mathrm{V}$ originates from a super-superlattice effect in encapsulated graphene when both the top and the bottom hBN layers are aligned to the graphene lattice [180]. More discussions on this effect can be found in chapter 8.

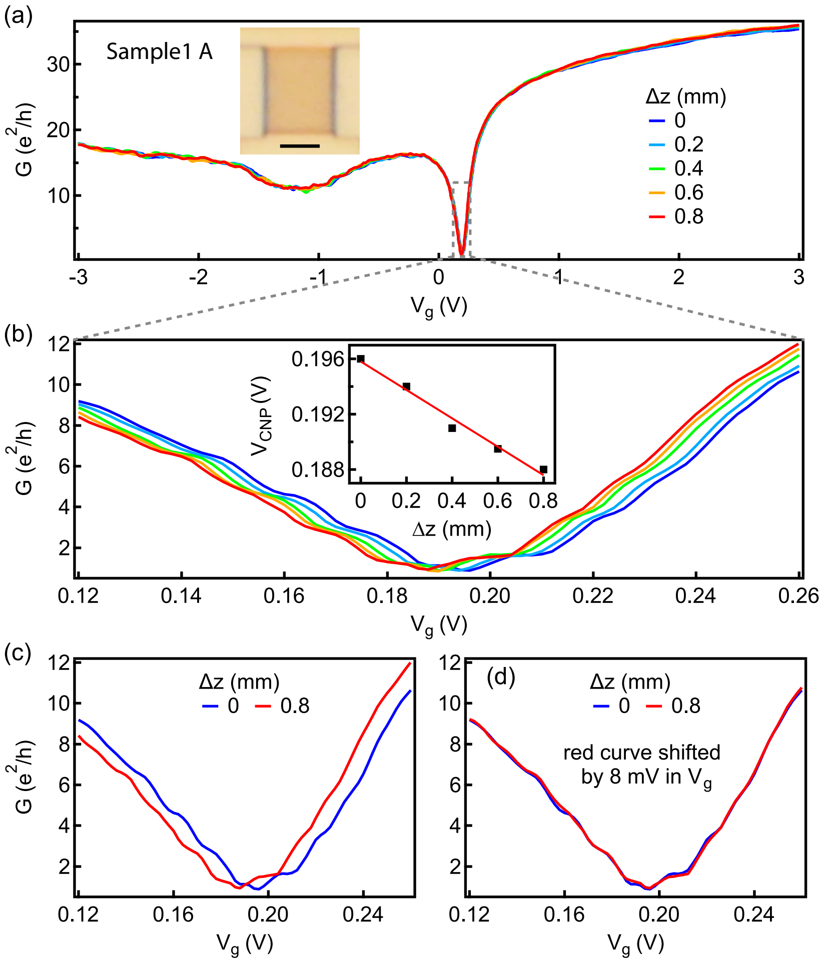

Figure 7.2. Strain-induced scalar potential. (a) Two-terminal differential conductance G plotted as a function of gate voltage V_g for different Δz. Inset: optical image of the measured device, scale bar corresponds to 2 µm. **(b)** Zoom-in to the CNP. Inset: position of the CNP (V_CNP) plotted as a function of Δz. The values of V_CNP are extracted by reading out the minimum conductance point. Red line is a linear fit with a slope of ∼10 mV/mm. **(c)** Zoom-in to the CNP for $\Delta z = 0$ and $\Delta z = 0.8$ mm. **(d)** The same as in **(c)** with the $\Delta z = 0.8$ mm curve shifted by 8 mV in V_g.

A zoom-in to the CNP is shown in Fig. 7.2(b), where very regular oscillations in conductance are observed. These features are reminiscent of quantized conductance originated from quantum point contacts [68, 210]. However, the corresponding Fermi wavelengths at the carrier densities of these oscillations are on the order of a few hundred nm[2], which are an order of magnitude smaller than the device width (∼4.4 µm). Therefore, this possibility is ruled out. Another possibility could be the Fabry-Pérot resonances due to a region near each contact that has a different doping from the bulk [13, 72, 141, 211]. The electrical contacts to the graphene are below the metallic leads and are ∼400 nm away from the two vertical dark interfaces seen in the optical image of the device shown in the inset of Fig. 7.2(a). This design is intended for mechanical reinforcement of the contacts, see appendix B.1. A cavity length of ∼450 nm[3] is extracted from the oscillations, which matches well the ∼400 nm overlap near the contacts. We therefore tentatively attribute these oscillations to Fabry-Pérot resonances.

Apart from these strain-independent conductance oscillations, a systematic shift of the CNP in V_g is observed with increasing Δz, see Fig. 7.2(b). This effect is reversible with decreasing Δz. The CNP of each curve at gate voltage V_CNP is extracted by reading out the minimum conductance point and is plotted as a function of Δz in the inset of Fig. 7.2(b). The plot shows a clear down-shift of V_CNP with increasing Δz. A linear fit to the data yields a slope of ∼10 mV/mm. The shift of the CNP is better seen in Fig. 7.2(c), where only the curves with the lowest ($\Delta z = 0$) and the highest strain ($\Delta z = 0.8\,\mathrm{mm}$) are plotted. Shifting the curve at $\Delta z = 0.8\,\mathrm{mm}$ by 8 mV in V_g, all the features fall onto that of the curve at $\Delta z = 0$, as can be seen in Fig. 7.2(d). This effect is different from the bending-induced gating effect due to gate capacitance change in suspended samples, where the gate-voltage axis is rescaled by a multiplication factor instead of a constant shift (see section 5.4.6). We attribute this shift to a strain-induced scalar potential in graphene. With a lever arm of $\sim 4.92 \times 10^{15}\,\mathrm{m}^{-2}\,\mathrm{V}^{-1}$, extracted from quantum Hall measurements, and the relation $E_\mathrm{F} = \hbar v_\mathrm{F}\sqrt{\pi n}$, where n is the charge carrier density, a down-shift of $\Delta V_\mathrm{CNP} = 8\,\mathrm{mV}$ can be converted to a Fermi level up-shift of $\Delta E_\mathrm{F} = \sim 7.3\,\mathrm{meV}$. The lever arm is a constant used to convert the gate voltage to the carrier density, which is determined by the gate capacitance of the device. As introduced in section 2.3.1, the strain-induced scalar potential can be written as [44, 90, 93]

$$V(x,y) = V_0 \cdot (\varepsilon_\mathrm{xx} + \varepsilon_\mathrm{yy}), \tag{7.1}$$

where ε_xx and ε_yy are the diagonal components of the strain tensor, and V_0 is a constant. It is worth noting that the value of V_0 is not well known [44,

---

[2] Estimated with $\lambda_\mathrm{F} = 2\pi/k_\mathrm{F} = 2\pi/\sqrt{\pi n}$.

[3] Estimated with $L = \sqrt{\pi}/(\sqrt{n_\mathrm{j+1}} - \sqrt{n_\mathrm{j}})$, where L is the cavity length, $\sqrt{n_\mathrm{j+1}}$ and $\sqrt{n_\mathrm{j}}$ are the corresponding carrier densities of two consecutive oscillations [211]

90, 93, 212, 213] and here we use $V_0 \approx 2.5\,\mathrm{eV}$, which is estimated from a work function study of graphene [90]. The scalar potential acts effectively as a shift of the graphene Fermi level. Assuming a homogeneous uniaxial strain along the x-direction, with the Poisson's ratio $\nu = 0.165$ of graphene [42], the strain induced by bending in the graphene at $\Delta z = 0.8\,\mathrm{mm}$ can then be calculated with $\Delta E_\mathrm{F} = V_0(1-\nu)\varepsilon_\mathrm{xx}$, yielding $\varepsilon_\mathrm{xx} \approx 0.35\,\%$. This value matches very well the strain that can be achieved in our setup at such bending of the substrate [166], as shown by the Raman studies in chapter 5. The consistency of the transport and Raman measurements confirms the scalar potential origin of the observed strain effect.

The strain-induced scalar potential has been observed in all our devices (more than 10) of both geometry types. In some devices this effect is complicated by conductance fluctuations at the CNP, making the quantitative analysis difficult.

7.4. Strain effects in conductance fluctuations

Apart from the scalar potential, strain can also generate a vector potential in graphene, which, for example, gives rise to a PMF for non-uniform strain fields [44, 45, 86, 202]. A strain field with a constant gradient is a simple form of non-uniform strain fields, which can be realized with a trapezoidal device geometry as shown by Raman measurements in chapter 5. Experimental phenomena that are sensitive to magnetic fields, such as conductance fluctuations (CF), can be used to detect such strain-induced PMFs.

The gate voltage dependence of two-terminal differential conductance of two devices with different geometries are presented for different Δz in Fig. 7.3(a,b), respectively. No significant strain effects are observed in these measurements except a similar scalar potential (not shown) as for Sample1 A. A field-effect mobility of $\sim 110\,000\,\mathrm{cm}^2\,\mathrm{V}^{-1}\,\mathrm{s}^{-1}$ ($\sim 140\,000\,\mathrm{cm}^2\,\mathrm{V}^{-1}\,\mathrm{s}^{-1}$) is extracted for Sample2 A (Sample2 B). The additional conductance minimum near $V_\mathrm{g} = 1\,\mathrm{V}$ for both devices is again the super-superlattice effect [180].

To study strain effects in CF, we measure two-terminal differential conductance as a function of small out-of-plane magnetic field B at $V_\mathrm{g} = 0$ with smaller steps in Δz. A smoothed background in B is subtracted from each curve in order to extract the CF. The conductance after subtraction of both devices are shown in Fig. 7.3(c) and (d), respectively. Fluctuations of the conductance as a function of magnetic field are observed. When Δz is increased, the fluctuations start to evolve. For the first $\sim 0.15\,\mathrm{mm}$ of Δz (shaded area), the features stay unchanged, which we attribute to a mechanical hysteresis of the bending setup. For the square device (Sample2 A) the CF change in a rather random manner with Δz, while a more clear trend is observed for the trapezoidal device (Sample2 B), as indicated by dashed lines in Fig. 7.3(d).

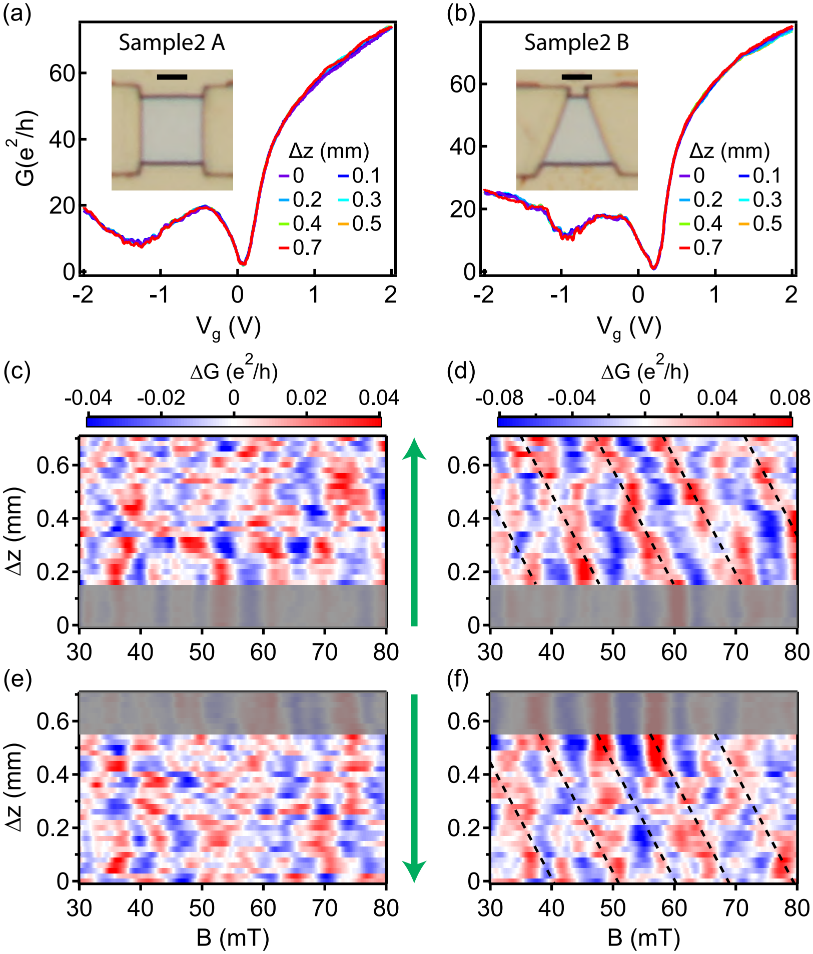

Figure 7.3. Strain effects in conductance fluctuations. (a,b) Two-terminal differential conductance G measured as a function of gate voltage V_g at different Δz for two devices with different geometries, respectively. Insets: optical images of the measured devices, scale bars correspond to 2 µm. **(c,d)** Conductance fluctuations measured in magnetic field B with increasing Δz for sample2 A and B, respectively. A smooth background in B is subtracted for each Δz. **(e,f)** The same as **(c,d)** for decreasing Δz. The mechanical hysteresis of the bending setup is indicated with filled gray boxes. The green arrows show the bending direction. Parallel dashed lines are guide to the eye.

Similar results are found for decreasing Δz, as shown in Fig. 7.3(e,f), where the mechanical hysteresis can also be seen.

As introduced in section 2.2.4, the CF originate from quantum interference between different trajectories of the charge carriers. The interference can be tuned by different means, such as by changing the charge carrier wavelength, by altering the trajectories, or by adding a phase. In graphene, the charge carrier wavelength can be tuned by shifting the Fermi level with an electric gate. A strain-induced scalar potential can also shift the Fermi level in graphene [44, 86, 92], therefore strain can in principle tune the CF via the mechanism of changing the charge carrier wavelength. However, the scalar potential here is so small that its effect on the CF is negligible, as can be seen in the measurements of CF in V_g shown in the appendix D. The period of the CF in V_g is on the order of 100 mV, while the achieved scalar potential corresponds to the order of 10 mV. Therefore, the large change of CF in B cannot be attributed to strain-induced scalar potential.

Another way to tune the CF is to change the trajectories of the charge carriers, which can be realized by changing the disorder in graphene or by applying a perpendicular magnetic field that bends the trajectories of the charge carriers. Strain can induce a PMF that acts on the orbital motion of the charge carriers [44–46, 86, 202]. In Sample2 A, however, a uniform strain field is expected which does not result in a global PMF. It has been shown in chapter 6 that local random strain fluctuations are present even in encapsulated graphene devices and such strain fluctuations can be tuned by the global strain. Although the mobility value extracted from the global transport is not limited by strain fluctuations in such high mobility devices, local effects of changing strain fluctuations can still be present, such as altering the scattering paths. With this mechanism, the CF are expected to change in a random manner. We therefore tentatively attribute the strain-tuning of the CF in Sample2 A (see Fig. 7.3(c,e)) to the modification of local strain fluctuations which is effectively like changing the disorder in graphene.

For Sample2 B, a clear directional shift of all the CF features is observed with increasing Δz instead of a random change, as shown in Fig. 7.3(d). The parallel dashed lines are guides to the eye. The trapezoidal geometry of this device is designed for generating a strain gradient which leads to a fairly homogeneous global PMF [44]. From the total shift of the CF features in Fig. 7.3(d), a global PMF of $\sim$10 mT could be extracted, which matches very well the value estimated from Raman measurements for a similar device in chapter 5. Before we attribute the CF shift to a strain-induced PMF, there is one problem to be solved. If the phase coherent paths of the charge carriers would be valley degenerate, one would expect a splitting of the CF features instead of a single shift because the PMF has an opposite sign for the two valleys [21, 44, 93, 214]. Here we argue with the local strain fluctuations which generates small PMFs locally [197]. Due to the opposite sign for the two valleys, the local

PMFs should lead to a separation of charge carriers with different valleys during the scattering process, making the possible trajectories for each charge carrier valley polarized. The preservation of the valley degree of freedom is a fair assumption here, because the intervalley scattering time in high mobility devices is much longer than the elastic scattering time [67]. The CF shown in Fig. 7.3(d) is very regular in B, which might originate from a single dominating Aharonov-Bohm like scattering loop in the simplest picture. From the CF period $B_0 \approx 15\,\mathrm{mT}$ in an external magnetic field, a characteristic loop size of $l = \sqrt{\Phi_0/B_0} \approx 500\,\mathrm{nm}$ can be extracted, where $\Phi_0 = h/e$ is the magnetic flux quantum. A mean free path of $l_{\mathrm{mfp}} \approx 100\,\mathrm{nm}$ is calculated with $l_{\mathrm{mfp}} = 2D/v_{\mathrm{F}}$, where $D \approx 0.05\,\mathrm{m}^2\,\mathrm{s}^{-1}$ is the diffusion constant[4] at the density the CF are measured and $v_{\mathrm{F}} \approx 1 \times 10^6\,\mathrm{m\,s}^{-1}$ is the Fermi velocity. A phase coherence time of $\tau_\phi \approx 13\,\mathrm{ps}$ is extracted from the autocorrelation of the CF [215], leading to a phase coherence length of $l_\phi = \sqrt{D\tau_\phi} \approx 800\,\mathrm{nm}$, which makes our interpretation with a single Aharonov-Bohm like loop plausible. The strain gradient induced global PMF induces an additional phase to the valley polarized Aharonov-Bohm loop, which shifts the CF in one direction. For decreasing Δz the CF shift is reversible, as shown in Fig. 7.3(f). We find the features become less regular, the exact reason for that is not clear. We speculate that it might be caused by the distortion of the single Aharonov-Bohm like loop during the reversed process.

7.5. Strain effects in transverse magnetic focusing

Transverse magnetic focusing (TMF) has been used to study the Fermi surface of metals [74], semiconductor heterostructures [216], mono-, bi-and tri-layer graphene [69], as well as graphene superlattice [70]. Here, we use TMF as a spectroscopy tool to investigate in situ strain-induced changes in the band structure of graphene.

To study TMF, we fabricated multi-terminal encapsulated graphene devices. The four-terminal resistance of the investigated device as a function of gate voltage is shown in Fig. 7.4. The resistance peak around the CNP becomes sharper with increasing Δz, suggesting a carrier mobility enhancement with strain, which is discussed in chapter 6. The field-effect mobility of this device is $\sim 60\,000\,\mathrm{cm}^2\,\mathrm{V}^{-1}\,\mathrm{s}^{-1}$. A shift of the CNP due to the strain-induced scalar potential is also observed, as shown in the right inset of Fig. 7.4.

The measurement configuration for TMF is shown in the left inset of Fig. 7.4, where a current is injected from contact C_4 while contact C_2 is on ground. A non-local resistance R_{NL} is calculated by normalizing the probed voltage $V_{C_3C_1}$ between contact C_3 and C_1 by the injected current $I_{C_4C_2}$. The maps of R_{NL}

---

[4] Estimated using the Einstein relation $\sigma = e^2\rho(E_{\mathrm{F}})D$, where $\rho(E_{\mathrm{F}}) = 2\sqrt{n}/(\sqrt{\pi}\hbar v_{\mathrm{F}})$ is the density of states for monolayer graphene

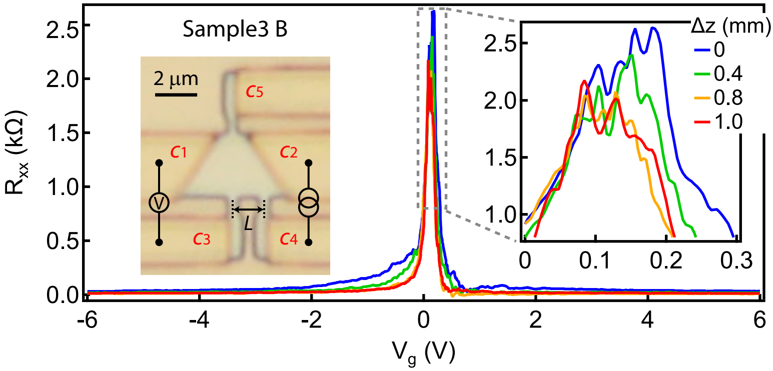

Figure 7.4. Four-terminal resistance and device scheme. Four-terminal resistance R_{xx} measured as $V_{C_3C_4}/I_{C_1C_2}$ for different Δz. The inset on the right shows the zoom-in to the CNP, where the strain induced scalar potential is observed. The inset on the left shows the measurement scheme for TMF, where current $I_{C_4C_2}$ is injected from contact C_4 into graphene and the non-local voltage $V_{C_3C_1}$ is measured. $L = 1.5\,\mu\text{m}$ and the width of the side contacts is ~500 nm.

as a function of V_{g} and B for different Δz are shown in Fig. 7.5. The top insets show representative trajectories for each TMF mode. The first mode (middle inset) originates from charge carriers propagating directly from the injector to the collector and for the second mode (right inset) charge carriers reflect once at the edge before reaching the collector. There is another mode (left inset) in the region with opposite magnetic field, which corresponds to a small portion of the charge carriers reflecting once at the big tilted contact C_2 on the right before reaching the collector. For electrons (n-doping), the first and second TMF modes occur in positive B region, while for holes (p-doping) they appear in negative B region due to the opposite sign of the charge carriers.

For charge carriers in a system with a circular Fermi surface, the magnetic field, B_{f}, required to focus them at a distance of L is given by [74]

$$B_{\text{f}}^{(N)} = \left(\frac{2\hbar k_{\text{F}}}{eL}\right) N, \tag{7.2}$$

where $N = 1, 2, 3...$ is the mode number, $\hbar$ is the reduced Planck constant, e is the elementary charge and k_{F} is the Fermi wave vector. This relation also holds for graphene [69], where $k_{\text{F}} = \sqrt{4\pi n/g_{\text{s}}g_{\text{v}}}$ with n being the carrier density and $g_{\text{s}} = g_{\text{v}} = 2$ being the spin and valley degeneracies respectively. The carrier density n can be tuned by the gate voltage V_{g} with the relation

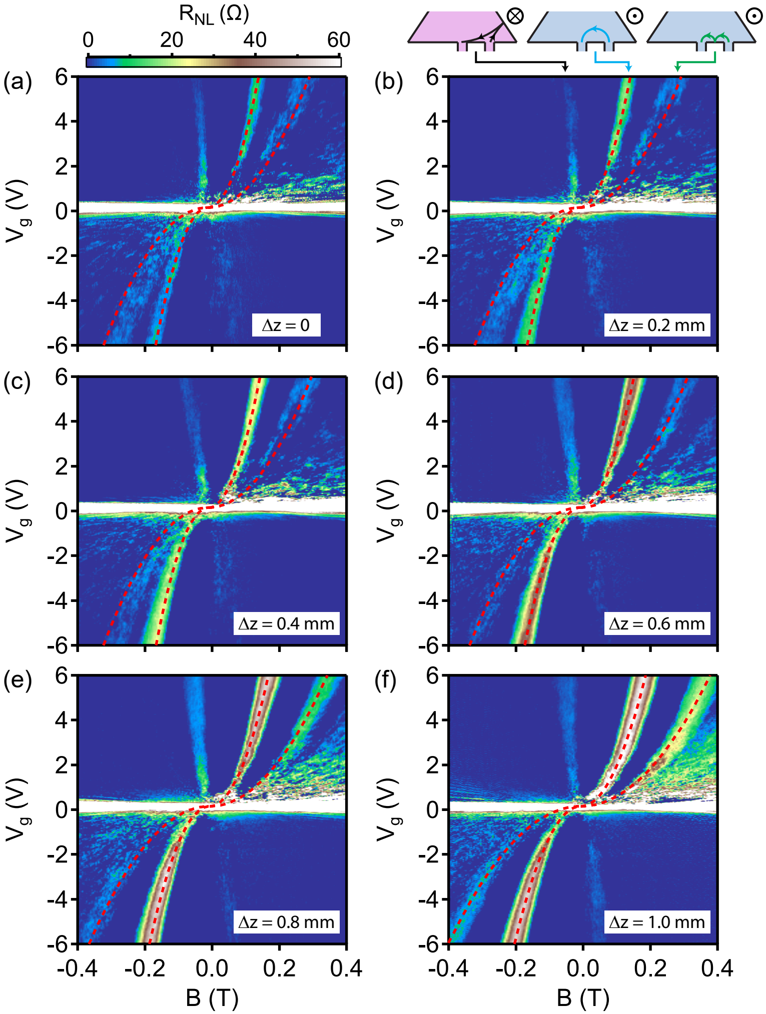

Figure 7.5. TMF maps for different strain. Non-local resistance $R_{\mathrm{NL}} = V_{C_3C_1}/I_{C_4C_2}$ is measured as a function of gate voltage V_{g} and out-of-plane magnetic field B for different Δz. TMF peaks from different modes can be observed, with the top insets showing representative trajectories for each mode. Dashed lines for the first mode are fits according to Eq. 7.3 and dashed lines for the second mode are calculated from the first mode.

$n = \alpha(V_\mathrm{g} - V_\mathrm{CNP})$, where α is the lever arm and V_CNP is the position of the CNP. We can then fit the position of the first TMF mode in the maps shown in Fig. 7.5 with

$$B_\mathrm{f} = \frac{2\hbar\sqrt{\pi\alpha(V_\mathrm{g} - V_\mathrm{CNP})}}{eL} + B_0, \tag{7.3}$$

where B_0 is an offset in magnetic field that might, for example, arise from trapped flux in the magnet.

As can be seen in the maps, the TMF features change substantially with increasing Δz. First, the overall amplitude of the signal increases with Δz. A line cut for each map at $V_\mathrm{g} = 6\,\mathrm{V}$ is shown in Fig. 7.6(a), where a clear shift of the TMF peaks with increasing Δz is also observed in addition to the amplitude increase. The amplitude value R_peak and the position B_peak in magnetic field of the first TMF peak are plotted as a function of Δz in Fig. 7.6(b) and (c), respectively. The amplitude increase can be understood with the mobility enhancement, which makes the system more ballistic and therefore enables more charge carriers to reach the collector, leading to an increase of the focusing amplitude. However, the shift of the focusing peaks in magnetic field cannot be explained by this mechanism. In the following we analyze the peak shift in detail by fitting the peak position of the first TMF mode with Eq. 7.3. The peak position of the second TMF mode can be calculated with Eq. 7.2 using the same parameters.

We consider different possibilities how strain could change Eq. 7.3. First, strain can induce a scalar potential that shifts the CNP. From Fig. 7.4, V_CNP is estimated to be ~0.15 V and ~0.11 V for $\Delta z = 0$ and 1.0 mm, respectively. We fitted with both values and found the effect of such a small shift in V_CNP to be negligible, therefore in the following we fix $V_\mathrm{CNP} = 0.15\,\mathrm{V}$ for the fitting. The second quantity that strain could change is the distance L. We then use a fixed lever arm $\alpha = 2.73 \times 10^{15}\,\mathrm{m}^{-2}\,\mathrm{V}^{-1}$ and fit the peaks for different Δz with L and B_0 as fitting parameters. This lever arm is extracted from a plate capacitor model, which matches very well the one extracted from quantum Hall measurements in a nearby square device from the same hBN/graphene/hBN stack. The third possibility could be that strain changes the lever arm α instead of the distance L. For this possibility, we fix $L = 1.5\,\mu\mathrm{m}$ and fit the peaks with α and B_0 as fitting parameters for different Δz. This distance $L = 1.5\,\mu\mathrm{m}$ is the center-to-center distance between the injector and collector contacts by design.

The fitting results for L and α are presented as a function of Δz in Fig. 7.6(d). For fixed α, the fitted distance L decreases from ~1.95 µm to ~1.53 µm when Δz is increased from 0 to 1.0 mm (red data points). Such a change in L is impossible in the experiments, because that would corresponds to a compressive strain of ~21.5 % which is in stark contradiction to the Raman measurements discussed in chapter 5. Therefore, this possibility is ruled out. For fixed

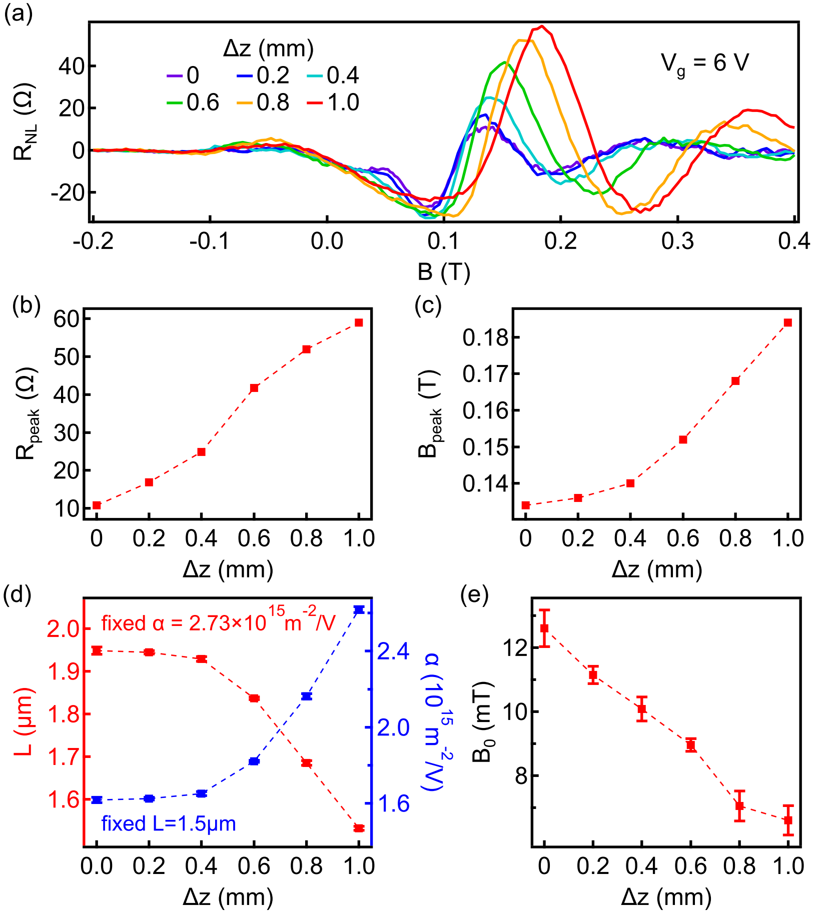

Figure 7.6. Analysis of strain effects in TMF. (a) Cuts at $V_\mathrm{g} = 6\,\mathrm{V}$ of the maps shown in Fig. 7.5. **(b,c)** Peak value of R_NL and peak position in B for the first TMF mode in **(a)** as a function of Δz. **(d)** Fitting results for L with a fixed lever arm $\alpha = 2.73 \times 10^{15}\,\mathrm{m}^{-2}\,\mathrm{V}^{-1}$ (red) or for α with a fixed $L = 1.5\,\mu\mathrm{m}$ (blue) as a function of Δz. **(e)** Fitting results for offset magnetic filed B_0 as a function of Δz. Error bars are the standard error from fitting.

L, the fitted lever arm α increases from $1.62 \times 10^{15}\,\mathrm{m^{-2}\,V^{-1}}$ at $\Delta z = 0$ to $2.62 \times 10^{15}\,\mathrm{m^{-2}\,V^{-1}}$ at $\Delta z = 1.0\,\mathrm{mm}$ (blue data points). We could not find any mechanism accounting for such a large change in the lever arm. It has been shown in section 5.4.6 that the gate capacitance does not change with Δz, clearly in contrast to the extracted values. Therefore the possibility of lever arm change is also ruled out.

Equation 7.3 is based on $k_\mathrm{F} = \sqrt{\pi n}$, which only holds for a circular Fermi surface. It has been shown theoretically that strain can make the Fermi velocity anisotropic and deforms the Fermi surface from a circle in graphene [90, 97], and a position-dependent Fermi velocity induced by strain can affect local probe experiments [94]. Therefore, one possible explanation of the strain-induced position change of the TMF peaks could be the strain-induced modification of the Fermi velocity and thus of the relation $k_\mathrm{F} = \sqrt{\pi n}$. A theoretical model is needed to analyze this possibility quantitatively.

The fitting results for the offset magnetic field B_0 are the same for either fixed α or fixed L, which surprisingly shows a systematic decrease with Δz, as shown in Fig. 7.6(e). The shift of B_0 is on the same order as the PMF extracted from CF experiments in Fig. 7.3(d). However, different from CF, we cannot argue for valley polarized charge carries here because Eq. 7.3 for TMF includes valley degeneracy. An interpretation invoking PMF here would be inconsistent with theoretical predictions that the PMF has opposite sign for different valleys [21, 44, 93, 214].

All the above mentioned strain effects in TMF experiments are reversible with decreasing Δz. Similar effects are observed for a second device. Further theoretical investigations are needed to fully understand the position change of the TMF peaks with strain.

7.6. Strain effects in quantum Hall regime

After studying strain effects in measurements with small magnetic fields, we increase the magnetic field and investigate strain effects in the quantum Hall regime. Devices of both geometry types are studied and distinct strain effects are observed. For square devices, only strain-induced scalar potential is observed while peculiar strain effects are observed for trapezoidal devices.

7.6.1. Square devices

The two-terminal differential conductance of a square device (Sample1 A) as a function of gate voltage at three different quantizing magnetic fields are presented in Fig. 7.7(a) for different Δz. Various quantum Hall plateaus are observed but no significant strain effects can be seen on this scale. The plateaus on the hole side are not well developed (not shown) due to the p-n junction near the contacts or the double moiré effect. On the electron side, the $\nu = 1$ plateau

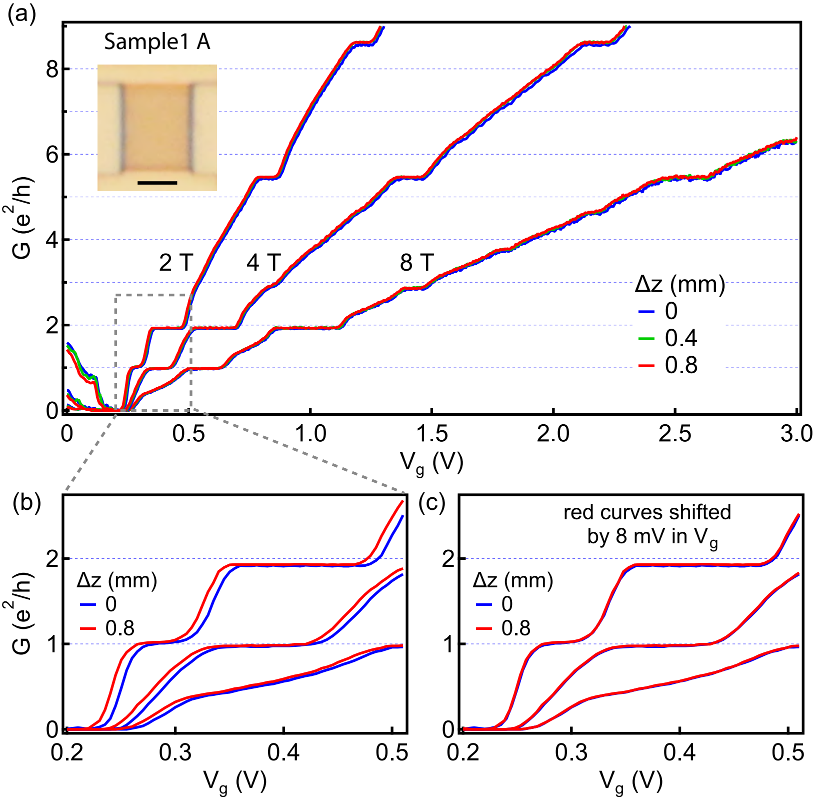

Figure 7.7. Square device in quantum Hall regime. **(a)** Two-terminal differential conductance of Sample1 A as a function of gate voltage at different magnetic fields for different Δz. **(b)** Zoom-in to a small region for $\Delta z = 0$ and $\Delta z = 0.8\,\mathrm{mm}$. **(c)** The same as in **(b)** with the $\Delta z = 0.8\,\mathrm{mm}$ curves shifted by $8\,\mathrm{mV}$ in V_g. Scale bar: $2\,\mu\mathrm{m}$.

is already well developed at $B = 2\,\mathrm{T}$, suggesting a very high device quality. At $B = 8\,\mathrm{T}$, even $\nu = 2/5, 4/3, 7/3...$ fractional states are observed [185–187, 217, 218]. The exact fraction of these states can be determined from the measurement of longitudinal magnetoresistance R_{xx}, where a Hall bar or a Corbino geometry is needed [187, 217, 218].

A zoom-in to a small region is shown in Fig. 7.7(b), where a shift of the plateaus in V_{g} is observed with increasing Δz. In Fig. 7.7(c), the curves at $\Delta z = 0.8\,\mathrm{mm}$ (red) are shifted by $8\,\mathrm{mV}$ in V_{g}, which are then identical to the curves at $\Delta z = 0$ (blue). This effect matches very well the one observed at zero magnetic field shown in section 7.3, and is attributed to the development of a strain-induced scalar potential. Similar results are observed on two other square devices fabricated from different stacks.

7.6.2. Two-terminal trapezoidal devices

In Fig. 7.8, the two-terminal differential conductance of two trapezoidal devices in different magnetic fields is plotted as a function of gate voltage for different Δz. The hole side is not shown because the conductance is suppressed due to contact doping induced p-n junction and no well developed quantum Hall plateaus are observed. Curves of smaller magnetic fields are shifted upwards sequentially by e^2/h for clarity. Both devices show surprisingly large effect of strain on the conductance that cannot be explained by a global scalar potential.

The field-effect mobility of Sample2 B2 is $\sim 65\,000\,\mathrm{cm^2\,V^{-1}\,s^{-1}}$, which does not show a significant enhancement with increasing Δz (not shown). A strain-induced scalar potential is observed at zero magnetic field (not shown) and is comparable to that observed for square devices. In Fig. 7.8(a), all plateau values do not change with Δz, suggesting that the contact resistance does not change with strain. At $B = 2\,\mathrm{T}$, strain does not affect the plateaus while at higher magnetic field the situation starts to change. At $B = 4\,\mathrm{T}$, the $\nu = 2$ and $\nu = 6$ plateaus become shorter with increasing Δz, but their onsets stay unchanged. Strain changes the transition between these two plateaus significantly and helps the broken symmetry states to develop. The $\nu = 3$ plateau becomes more visible with increasing Δz. When the magnetic field is increased to higher values, the strain effects become more pronounced, and the $\nu = 0$ and $\nu = 1$ plateaus appear but do not show strain dependence. Apparently, the strain-induced scalar potential, which would cause a shift of the whole curve in V_{g}, cannot explain the observed effects. For the quantum Hall effect, it is commonly believed that localized states induced by disorder in the bulk can pin the Fermi level between two Landau levels [219, 220], and thus affect the length of the quantum Hall plateaus in gate voltage. In our device, disorder due to random strain fluctuations can be reduced by increasing the global strain, as discussed in chapter 6. Reduced disorder would give less localized states in the bulk and thus reduce the pinning of the Fermi level

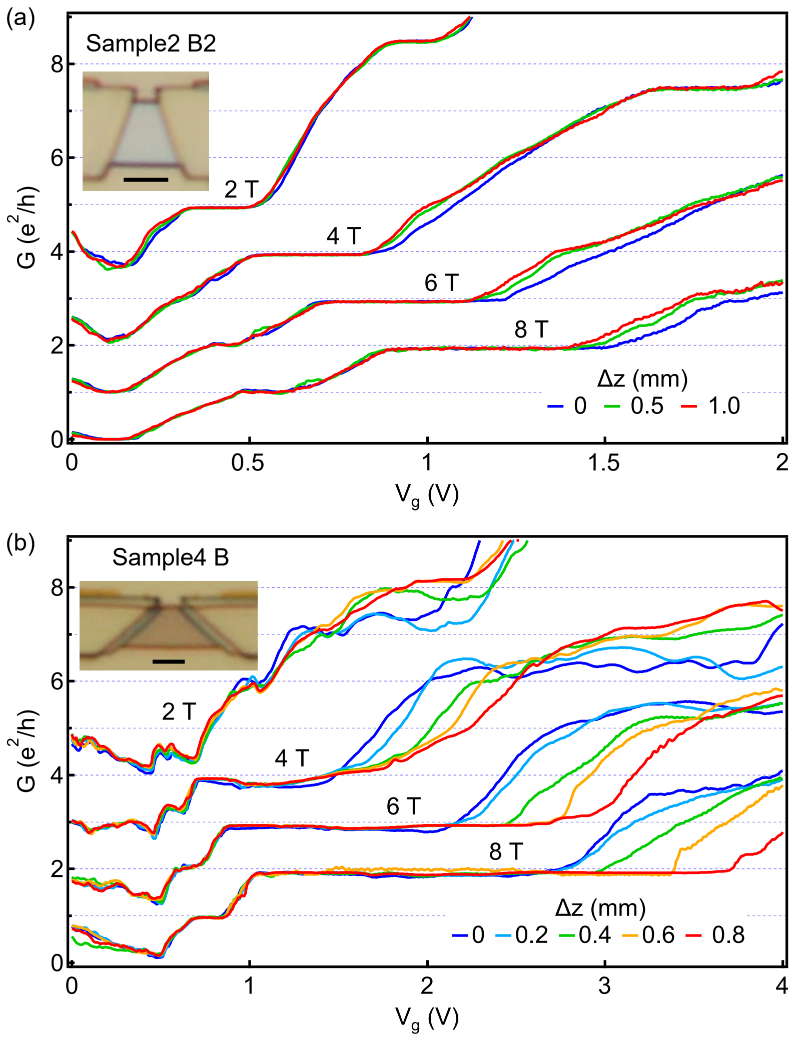

Figure 7.8. Two-terminal trapezoidal devices in quantum Hall regime. (a) Two-terminal differential conductance of Sample2 B2 as a function of gate voltage at different magnetic fields for different Δz. **(b)** The same as **(a)** for Sample4 B. Curves of smaller magnetic fields are shifted sequentially by e^2/h for clarity. Scale bars: 2 µm.

and lead to a shorter quantum Hall plateau in V_g at a fixed magnetic field, in agreement with our observations for the $\nu = 2$ and $\nu = 6$ plateaus shown in Fig. 7.8(a). However, this mechanism should affect all plateaus the same way, which is not the case in the experiments.

Another possible interpretation could be the strain-induced PMF (B_ps), which acts on the two valleys with opposite sign. In the presence of an external magnetic field B, charge carriers of one valley, say the K valley, would experience an effective magnetic field of $B+B_\mathrm{ps}$ while those of the other valley would experience $B-B_\mathrm{ps}$. Since the Landau level (LL) degeneracy is proportional to the magnetic field as introduced in section 2.2.5, a strain-induced PMF would then lead to a different number of states in the LLs with different valley indices. A change in the LL degeneracy at a fixed external magnetic field may manifest as a change of the quantum Hall plateau length in V_g, in agreement with our observations in the measurements shown in Fig. 7.8 qualitatively. However, there are several problems that make the quantitative analysis difficult. First, disorder can also affect the plateau length as discussed above, which cannot be fully ruled out. Second, in the broken symmetry regime, where the spin and valley degeneracies are lifted by interactions [221–223], the valley index of each state is not yet clear. In a recent spin-wave measurements [224], a valley sequence different from that determined from earlier tilted field magnetotransport measurements [81] and selective equilibration measurements [225] was invoked to explain their findings. Third, different devices show different strain effects in our experiments, as can be seen later for Sample4 B and Sample3 B. Furthermore, compared to the quantizing external magnetic field, the global PMF can be achieved in our devices is rather negligible (on the order of 10 mT) as discussed previously, which is unlikely to be responsible for such big changes on the quantum Hall plateaus.

The quality of Sample4 B is not very high with a field-effect mobility of $\sim 15\,000\,\mathrm{cm^2\,V^{-1}\,s^{-1}}$, which shows an enhancement with increasing Δz (not shown here). The strain effect in the quantum Hall regime is shown in Fig. 7.8(b), where the plateaus are not as regular as those in Sample2 B2. The $\nu = 1$ plateau does not show any strain dependence, the same as in Sample2 B2. The $\nu = 2$ state shows an extremely long plateau in V_g, which becomes even longer with increasing Δz, in stark contrast to that in Sample2 B2. A closer inspection of the curves at $B = 8\,\mathrm{T}$ shows that a new plateau appears after the $\nu = 2$ plateau at higher Δz. Although a mobility enhancement with strain is observed for this device, the strain effects on the quantum Hall plateaus cannot be attributed to this mechanism because the $\nu = 2$ plateau becomes longer, instead of shorter, with increasing Δz.

All the strain effects presented above are reversible for decreasing Δz. In the following we present quantum Hall measurements on a multi-terminal device, which provides more information, and more discussion is given there.

7.6.3. Multi-terminal trapezoidal devices

The multi-terminal device studied here is the one used for TMF studies in section 7.5. In Fig. 7.9(a,b), the two-terminal differential conductance G and the Hall conductance G_{xy} at $B = 2\,\mathrm{T}$ are plotted as a function of gate voltage for different Δz, respectively. Better defined quantum Hall plateaus are observed on the electron side for G while G_{xy} shows more pronounced plateaus on the hole side. The values of the well developed quantum Hall plateaus match very well the theoretical values for graphene, especially for G_{xy} at $\Delta z = 1.0\,\mathrm{mm}$. The strain effects here are really remarkable and are different from those observed in Sample2 B2 and Sample4 B. It is really surprising that more quantum Hall plateaus appear with increasing Δz for both cases, as if the curves were rescaled on the V_{g} axis. The plateaus in G become shorter and the plateaus in G_{xy} become better defined for larger Δz, which can be understood with the mobility enhancement shown in Fig. 7.4.

The classical Hall effect at small magnetic fields for different Δz is shown in the appendix D, which is usually used to extract the carrier density and the gate lever arm [10]. Relying on that, it seems the lever arm increases by a factor of three when Δz is increased from 0 to 1.0 mm, which can also be seen approximately from the slope of the curves in Fig. 7.9(b). However, such a large increase of the lever arm with Δz is not physical, as discussed previously in the TMF experiments. Furthermore, this effect is not observed in the two-terminal differential conductance, see appendix D. More discussion on the lever arm is also presented there.

We speculate that the trapezoidal geometry complicates the Hall measurements. It has been shown in a numerical study that a tilted graphene p-n junction can make the charge and current density larger along one side of the graphene sheet due to Klein tunneling [226], generating an artificial Hall effect. As discussed in section 7.3, p-n junctions do exist near the contacts in our devices. The tilted contacts of the trapezoidal devices construct exactly the scenario described in Ref. [226]. The irregular features in the G_{xy} measurements shown in Fig. 7.9(b) might be related to this mechanism, especially for small Δz. Although this complication makes the analysis more difficult, it cannot explain the huge strain effects observed here because it is unlikely that the p-n junctions vanish with the small applied strain in our devices.

In Fig. 7.10, the measurements at $B = 9\,\mathrm{T}$ are shown. Apart from the strain effects similar to those at $B = 2\,\mathrm{T}$, there is one more finding. The $\nu = 1$ plateau length in V_{g} shown in Fig. 7.10(a) first becomes shorter with increasing Δz and vanishes at $\Delta z = 0.8\,\mathrm{mm}$, and then reappears at $\Delta z = 1.0\,\mathrm{mm}$, which is in stark contrast to the constant $\nu = 1$ plateau for the devices shown in Fig. 7.8. At a fixed external magnetic field, strain-induced PMF can modify the Landau level energies. As discussed before, however, the small PMF alone might not be possible to explain the large effect here. Since the $\nu = 1$ plateau

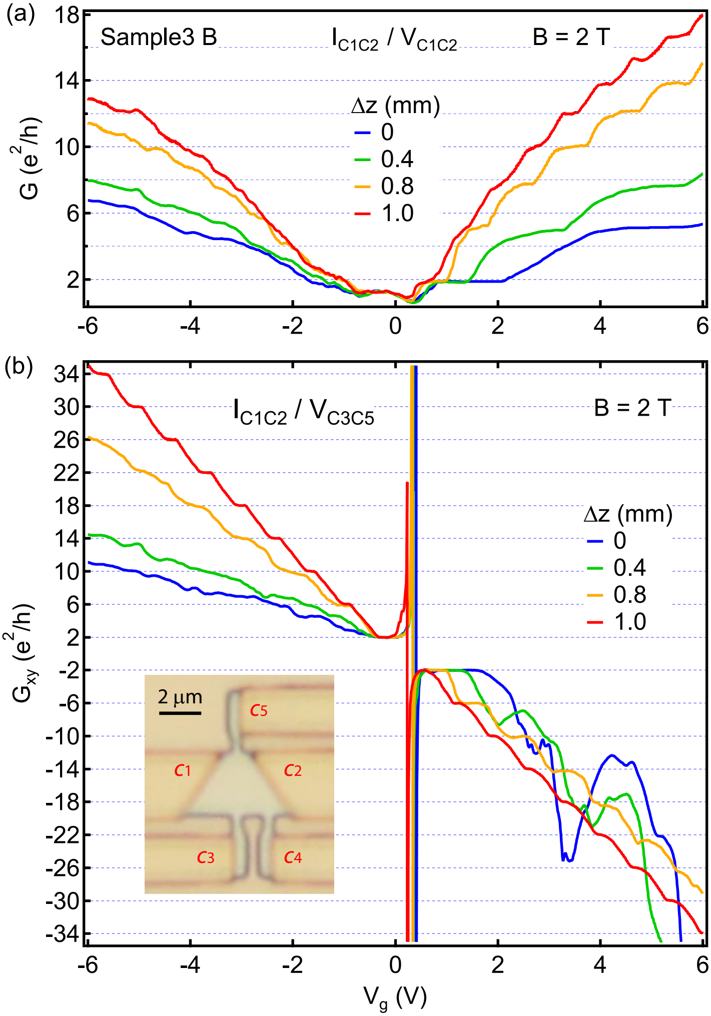

Figure 7.9. Quantum Hall effect of Sample3 B at $B = 2\,\mathrm{T}$. (a) Two-terminal differential conductance $G = I_{C_1C_2}/V_{C_1C_2}$ of Sample3 B as a function of gate voltage at $B = 2\,\mathrm{T}$ for different Δz. **(b)** $G_{\mathrm{xy}} = I_{C_1C_2}/V_{C_3C_5}$ measured at the same time.

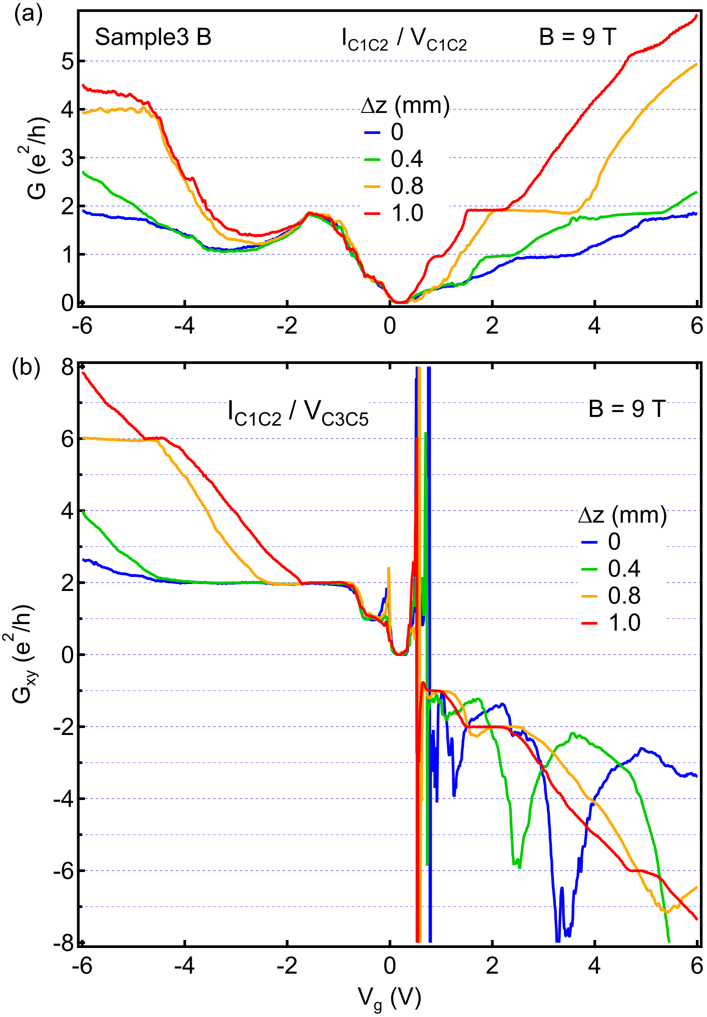

Figure 7.10. Quantum Hall effect of Sample3 B at $B = 9\,\mathrm{T}$. The same as Fig. 7.9 for $B = 9\,\mathrm{T}$.

arise from the strong Coulomb interactions [81], to fully understand the strain effect on this plateau might need to include the strain effect on the interactions, where further theoretical investigations are required.

All the above strain effects are reversible for decreasing Δz. Similar results are found for a second multi-terminal device.

7.7. Conclusion and outlook

In conclusion, we have shown strain effects in various transport experiments, some of which are understood and some need further experimental and theoretical investigations for a thorough understanding. A strain-induced constant shift of the conductance curves in V_g is attributed to a scalar potential, from which an extracted strain value matches very well the Raman measurements. A comparison of conductance fluctuations measurements between a square device and a trapezoidal device gives hints for a strain-induced PMF, the magnitude of which is consistent with the one estimated from Raman measurements and FEM analysis. In the TMF measurements, several strain effects are observed. First, the magnitude increase of the focusing peaks with strain we tentatively attribute to a mobility enhancement by reducing strain fluctuations. Second, the systematic shift of the offset magnetic field B_0 with strain might be related to PMF. Furthermore, a strain-induced position change of the focusing peaks in magnetic field is observed, which might has to do with the Fermi velocity renormalization in strained graphene. In the quantum Hall regime, a clear difference between the square devices and the trapezoidal devices is found. For square devices, no further strain effects are observed except for the scalar potential. In contrast, surprisingly large and complex strain effects are found for trapezoidal devices, where the data are still under discussion.

For future experiments, multi-terminal square/rectangular devices would provide more information about the strain effects in TMF measurements and also help to understand the strain effects in quantum Hall regime. Low-temperature Raman spectroscopy measurements would be useful to determine the actual strain in the devices. A scanning technique to map the charge carrier distribution in the devices would be helpful to understand the implication of the geometries. Furthermore, theoretical studies of strain effects on interactions in graphene would also help to interpret the observed strain effects.

8 Super-superlattice in doubly aligned hBN/graphene/hBN heterostructures[1]

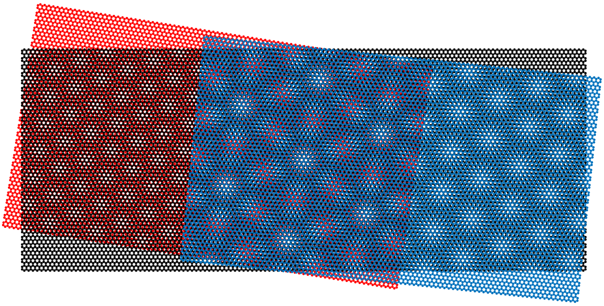

The specific rotational alignment of two-dimensional lattices results in a moiré superlattice with a larger period than the original lattices and allows one to engineer the electronic band structure of such materials. So far, transport signatures of such superlattices have been reported for graphene/hBN and graphene/graphene systems. In this chapter, we report moiré superlattices in fully hBN encapsulated graphene with both the top and the bottom hBN aligned to the graphene. In the graphene, two different moiré superlattices form with the top and the bottom hBN, respectively. The overlay of the two superlattices can result in a third superlattice with a period larger than the maximum period (14 nm) in the graphene/hBN system, which we explain in a simple model. This new type of band structure engineering allows one to artificially create an even wider spectrum of electronic properties in two-dimensional materials.[2]

---

[1] This chapter has been published in a similar form in Ref. [180]. © 2019 American Chemical Society

[2] Illustration of multiple moiré superlattices, prepared by Ming-Hao Liu.

8.1. Introduction

Superlattice (SL) structures have been used to engineer electronic properties of two-dimensional electron systems for decades [227–234]. Due to the peculiar electronic properties of graphene [21], SLs in graphene are of particular interest [126, 235–240] and have been investigated extensively utilizing different approaches, such as electrostatic gating [241–243], chemical doping [244], etching [245–247], lattice deformation [248] and surface dielectric patterning [249]. Since the introduction of hBN as a substrate for graphene electronics [136], moiré superlattices (MSLs) originating from the rotational alignment of the two lattices have been first observed and studied by STM [122, 124, 125]. It then triggered many theoretical [123, 127, 250, 251] and experimental studies, where secondary Dirac points [35–37], the Hofstadter Butterfly [35–39], Brown-Zak oscillations [35, 252], the formation of valley polarized currents [99] and many other novel electronic device characteristics [70, 211, 253–257] have been observed.

Recently, another interesting graphene MSL system has drawn considerable attention – twisted bilayer graphene, where two monolayer graphene sheets are stacked on top of each other with a controlled twist angle. For small twist angles, insulating states [258], strong correlations [259] and a network of topological channels [260] have been reported experimentally. More strikingly, superconductivity [40, 261] and Mott-like insulator states [41, 261] have been achieved, when the twist angle is tuned to the so-called “magic angle”, where the electronic band structure near zero Fermi energy becomes flat, due to the strong interlayer coupling.

So far, MSL engineering in graphene has concentrated mostly on MSLs based on two relevant layers (2L-MSLs). The formation of graphene/hBN 2L-MSLs has been introduced in section 2.4, where the modification of graphene band structure and the signature of such MSLs in transport measurements are also discussed. In fully encapsulated graphene, there are two graphene/hBN interfaces, namely at the top and at the bottom, which can result in a much richer and more flexible tailoring of the graphene band structure. Due to the 1.8% larger lattice constant of hBN, the largest possible moiré period that can be achieved in graphene/hBN systems is limited to about 14 nm [122], which occurs when the two layers are fully aligned. This situation changes when both hBN layers are aligned to the graphene layer. Here, we report for the first time the observation of a new MSL which can be understood by the overlay of two 2L-MSLs that form between the graphene monolayer and the top and bottom hBN layers of the encapsulation stack, respectively. In the transport measurements, we demonstrate that MSL with a period longer than 14 nm can indeed be obtained in doubly aligned hBN/graphene/hBN heterostructures, coexisting with the graphene/hBN 2L-MSLs. These experiments are in good agreement with a simple model for the moiré periods for doubly aligned hBN/graphene/hBN devices.

8.2. Moiré superlattices illustration

The formation of multiple MSLs is shown schematically in Fig. 8.1, when both hBN layers are considered . On the right side of the illustration, only the top hBN (blue) and the graphene (black) are present, which form the top 2L-MSL with period λ_1. The bottom hBN (red) forms the bottom 2L-MSL with graphene, shown on the left with period λ_2. In the middle of the illustration all three layers are present and a new MSL (3L-MSL) forms with a longer period, indicated with λ_3. The influence of the MSL can be modeled as an effective periodic potential with the same symmetry. The periodic potentials for the top 2L-MSL and the bottom 2L-MSL are calculated following the model introduced in Ref. [122], shown as insets in Fig. 8.1. To calculate the potentials for the 3L-MSL, we sum over the periodic potentials of the top 2L-MSL and the bottom 2L-MSL. The period of the 3L-MSL from the potential calculation matches very well the one of the lattice structure in the illustration.

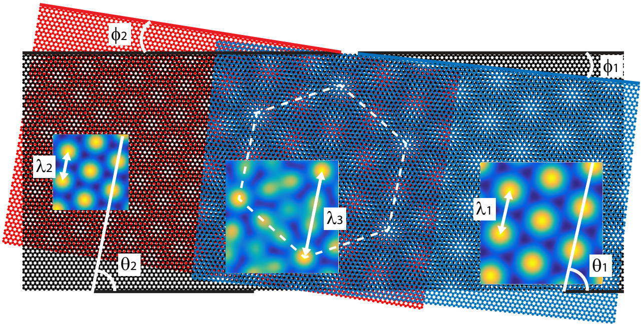

Figure 8.1. Multiple moiré superlattices. Illustration of three different MSLs formed in a hBN/graphene/hBN heterostructure. Blue, black and red hexagonal lattices represent top hBN, graphene and bottom hBN lattices, respectively. ϕ_1 (ϕ_2) is the twist angle between top (bottom) hBN and graphene. θ_1 (θ_2) indicates the orientation of the corresponding MSL with respect to graphene. The resulting moiré periods are indicated with $\lambda_{1,2,3}$. The 3L-MSL (middle part) has a larger period than both 2L-MSLs (left and right parts). Insets: moiré potential calculations.

8.3. Transport experiments and results

Transport measurements with and without magnetic field were performed at 4.2 K using standard low-frequency lock-in techniques.

8.3.1. Device fabrication

We fabricated fully encapsulated graphene devices with both the top and the bottom hBN layers aligned to the graphene, as described in section 3.1. We estimate an alignment precision of ∼1°. The schematic cross section of the devices is shown in Fig. 8.2(a). A global metallic bottom gate is used to tune the charge carrier density n, and one-dimensional Cr/Au edge contacts are used to contact the graphene [138]. An optical image of one device and the measurement scheme is shown Fig. 8.2(b).

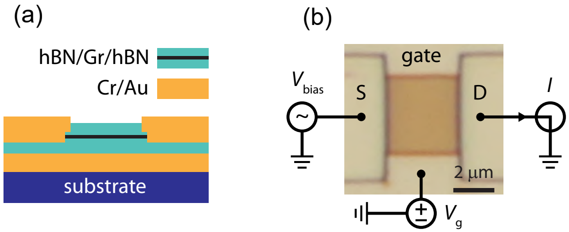

Figure 8.2. Device and measurement scheme. (a) Schematic cross section of the device. **(b)** Optical image of one measured device and sketch of experimental setup. ‘S’ and ‘D’ are the source and drain contacts, respectively.

8.3.2. Zero magnetic field measurements

The two-terminal differential conductance, G, of one device is plotted as a function of n in Fig. 8.3. The charge carrier density n is calculated from the gate voltage using a parallel plate capacitor model. The average conductance is lower on the hole side ($n < 0$) than on the electron side ($n > 0$), which we attribute to n-type contact doping resulting in a p-n junction near the contacts. The sharp dip in conductance at $n = 0$ is the main Dirac point (MDP) of the pristine graphene. Our device shows a large field-effect mobility of $\sim 90\,000\,\mathrm{cm^2\,V^{-1}\,s^{-1}}$, extracted from a linear fit around the MDP. The residual doping is of the order $\delta n \approx 1 \times 10^{10}\,\mathrm{cm^{-2}}$, extracted from the width of the MDP. In addition to the MDP, we find two pairs of conductance minima symmetrically around the MDP at higher doping, labeled A and C, which we attribute to two MSLs. The minima on the hole side are more pronounced than their counterparts on the electron side, similar to previously reported MSLs [35–37, 122].

Based on the simple model of periodic potential modulation [122, 126, 127], superlattice Dirac points (SDPs) are expected to form at the superlattice Brillouin zone boundaries at $\mathbf{k} = \mathbf{G}/2$, where $|\mathbf{G}| = 4\pi/(\sqrt{3}\lambda)$ is the length of the superlattice wavevector and λ the moiré period. For graphene, k is related to n by $k = \sqrt{\pi n}$. The position of the SDPs in charge carrier density for a given period λ is then $n_s = 4\pi/(3\lambda^2)$. The pair of conductance minima at $n_{s_A} \approx \pm 2.4 \times 10^{12}\,\mathrm{cm}^{-2}$ can be explained by a graphene/hBN 2L-MSL with a period of about 13.2 nm. However, the pair of conductance minima at $n_{s_C} \approx \pm 1.4 \times 10^{12}\,\mathrm{cm}^{-2}$ cannot be explained by a single graphene/hBN 2L-MSL, since it corresponds to a superlattice period of about 17.3 nm, clearly larger than the maximum period of ~14 nm in a graphene/hBN moiré system. We attribute the presence of the conductance dips at n_{s_C} to a new MSL that is formed by the three layers together: top hBN, graphene and bottom hBN. This 3L-MSL can have a period considerably larger than 14 nm.

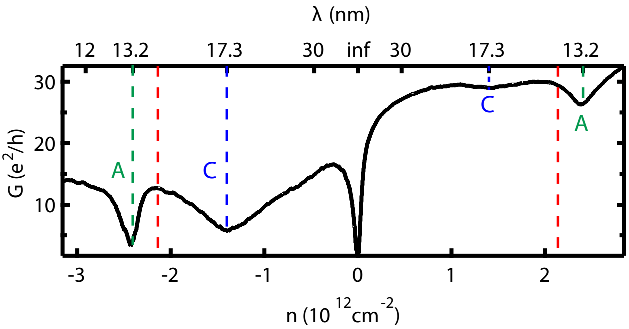

Figure 8.3. Two-terminal differential conductance. G plotted as a function of charge carrier density n. In addition to the MDP, there are 4 other conductance minima at $n_{s_A} \approx \pm 2.4 \times 10^{12}\,\mathrm{cm}^{-2}$ (green dashed lines) and $n_{s_C} \approx \pm 1.4 \times 10^{12}\,\mathrm{cm}^{-2}$ (blue dashed lines), respectively. The top axis shows the moiré periods $\lambda = \sqrt{4\pi/3n_s}$. The red dashed lines indicate the longest period (lowest density) for a graphene/hBN MSL.

8.3.3. Quantum Hall measurements

To substantiate this claim, we now analyse the data obtained in the quantum Hall regime. Figure 8.4(a) shows the Landau fan of the same device, where the numerical derivative of the conductance with respect to n is plotted as a function of n and the out-of-plane magnetic field B. Near the MDP, we observe the standard quantum Hall effect for graphene with plateaus at filling factors $\nu \equiv nh/(eB) = \pm 2, \pm 6, \pm 10, \ldots$, with h the Planck constant and e the electron charge. This spectrum shows the basic Dirac nature of the charge carriers in graphene. The broken symmetry states occur for $B \geqslant 2\,\mathrm{T}$, suggesting a high device quality. Around the SDPs at $n_{s_A} \approx \pm 2.4 \times 10^{12}\,\mathrm{cm}^{-2}$, the plot also shows filling factors $\nu \equiv (n - n_{s_A})h/(eB) = \pm 2, \pm 6, \ldots$, consistent with previous graphene/hBN MSL studies [35]. Around the SDPs at $n_{s_C} \approx \pm 1.4 \times 10^{12}\,\mathrm{cm}^{-2}$, there are also clear filling factors fanning out on the hole side with $\nu \equiv (n - n_{s_C})h/(eB) = \pm 2$, which is consistent with a Dirac spectrum at n_{s_C}, while on the electron side the corresponding features are too weak to be observed. In addition, lines fanning out from a SDP located at density $n <$

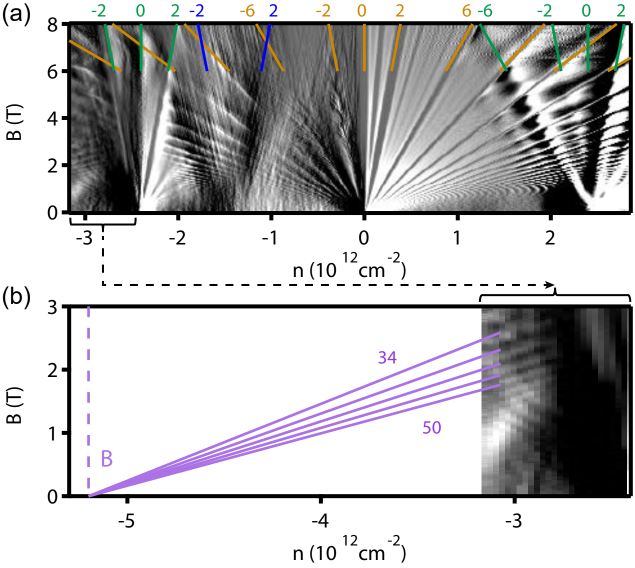

Figure 8.4. Landau fan diagram. (a) dG/dn as a function of n and B of the same device. Filling factors fan out from all DPs, except for the blue one on the electron side, and are indicated on top of the diagram, calculated as $\nu \equiv nh/(eB)$, where n is counted from each DP. **(b)** Zoom-in on the left side of **(a)**. There are additional lines fanning out from an even higher density $n_{s_B} \approx 5.2 \times 10^{12}\,\mathrm{cm}^{-2}$, labeled B. The filling factors of these lines are 34, 38, 42, 46 and 50, respectively.

$-3 \times 10^{12}\,\mathrm{cm}^{-2}$ are observed. A zoom-in is plotted in Fig. 8.4(b). The lines extrapolate to a density of about $-5.2 \times 10^{12}\,\mathrm{cm}^{-2}$, denoted n_{s_B}, with filling factors $\nu = 34, 38, 42, 46, ...$ This density cannot be explained by the “tertiary" Dirac point occuring at the density of about $1.65 n_{s_A}$, which comes from a Kekulé superstructure on top of the graphene/hBN MSL [262]. However, n_{s_B} matches the SDP from a MSL with a period of about 9 nm. We therefore attribute it to a 2L-MSL originating from the alignment of the second hBN layer to the graphene layer.

8.4. Geometrical analysis

As derived in Ref. [122, 123] and also introduced in section 2.4, the period λ for a graphene/hBN MSL is given by

$$\lambda = \frac{(1+\delta)a}{\sqrt{2(1+\delta)(1-\cos\phi)+\delta^2}}, \tag{8.1}$$

where a (2.46 Å) is the graphene lattice constant, δ (1.8%) is the lattice mismatch between hBN and graphene and ϕ (defined for -30° to 30°) is the twist angle of hBN with respect to graphene. The moiré period is maximum at $\phi = 0$ with a value of $\lambda \approx 14\,\mathrm{nm}$. This corresponds to the lowest carrier density of $n_{min} \approx \pm 2.2 \times 10^{12}\,\mathrm{cm}^{-2}$ for the position of the SDPs (red dashed lines in Fig. 8.3). The orientation of the MSL is described by the angle θ relative to the graphene lattice,

$$\tan\theta = \frac{-\sin\phi}{(1+\delta)-\cos\phi}. \tag{8.2}$$

For the graphene/hBN system, one finds $|\theta| \lesssim 80^\circ$ [122]. These two equations describe the top 2L-MSL and the bottom 2L-MSL, as shown schematically in Fig. 8.1. The functional dependence of λ and θ on ϕ is shown in section 2.4.

8.4.1. Geometrical analysis for super-superlattice

In a fully encapsulated graphene device, not only one, but both hBN layers can be aligned to the graphene layer so that two graphene/hBN 2L-MSLs can form. In this case, the potential modulations of the two 2L-MSLs are superimposed and form a MSL with a third periodicity. The values of the resulting periods can be understood based on Fig. 8.5. The vectors $\vec{g}$, $\vec{b}_1$ and $\vec{b}_2$ denote one of the reciprocal lattice vectors for the graphene, the top hBN and the bottom hBN layers, respectively. The twist angle between the top (bottom) hBN and graphene is denoted ϕ_1 (ϕ_2). Following the derivations in Ref. [122, 123], one of the top 2L-MSL (bottom 2L-MSL) reciprocal lattice vectors $\vec{k}_1$ ($\vec{k}_2$) is given by the vector connecting $\vec{g}$ to $\vec{b}_1$ ($\vec{b}_2$). The moiré period $\lambda_{1,2}$ is then given by

$\lambda_{1,2} = 4\pi/\sqrt{3}\left|\vec{k}_{1,2}\right|$, which is explicitly described by Eq. (8.1) as a function of the twist angle $\phi_{1,2}$. Since the reciprocal lattices of the top 2L-MSL and the bottom 2L-MSL are triangular, the same as those for graphene and hBN, we can use the same approach to derive the 3L-MSL, which is described by the vector connecting $\vec{k_2}$ to $\vec{k_1}$, denoted $\vec{k_3}$. The 3L-MSL period is then given by $\lambda_3 = 4\pi/\sqrt{3}\left|\vec{k}_3\right|$.

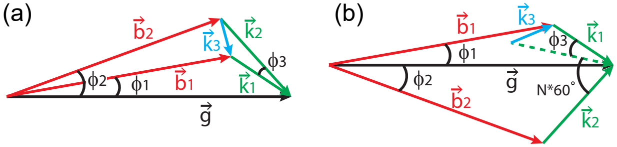

Figure 8.5. Geometrical analysis. **(a)** Schematics in reciprocal space for the formation of different MSLs, where $\vec{g}, \vec{b}_1, \vec{b}_2, \vec{k}_1, \vec{k}_2$ and $\vec{k}_3$ are one of the reciprocal lattice vectors for graphene, top hBN, bottom hBN, top 2L-MSL, bottom 2L-MSL and 3L-MSL, respectively. **(b)** For the case of twist angle larger than 30°. N is an integer, which can be 1, 2, or 3.

In order to calculate λ_3 using Eq. (8.1), we first need to find the new a, δ and ϕ. Due to symmetry, we only consider $\phi_1 < \phi_2$, so λ_2, the smaller period of the two graphene/hBN 2L-MSLs, becomes the new a and the new δ will then be given by $(\lambda_1 - \lambda_2)/\lambda_2$. The new ϕ, denoted ϕ_3, is determined by $|\theta_1 - \theta_2|$, where θ_1 (θ_2) is the relative orientation of the top 2L-MSL (bottom 2L-MSL) with respect to the graphene lattice, described by Eq. (8.2). Different cases occur for ϕ_3 due to the 60° rotational symmetry of the lattices. Since ϕ in Eq. (8.1) is defined for −30° to 30°, we subtract multiples of 60° to bring ϕ_3 to this range if it is larger than 30°, given as

$$\phi_3 = \begin{cases} |\theta_1 - \theta_2| & \text{if } 0 < |\theta_1 - \theta_2| \leqslant 30^\circ \\ |\theta_1 - \theta_2| - 60^\circ & \text{if } 30^\circ < |\theta_1 - \theta_2| \leqslant 90^\circ \\ |\theta_1 - \theta_2| - 120^\circ & \text{if } 90^\circ < |\theta_1 - \theta_2| \leqslant 150^\circ \\ |\theta_1 - \theta_2| - 180^\circ & \text{if } 150^\circ < |\theta_1 - \theta_2| \leqslant 180^\circ. \end{cases}$$

For the first case, the 3L-MSL is effectively the MSL formed by the two hBN layers, as illustrated in Fig. 8.5(a). Another case is shown in Fig. 8.5(b), where multiples of 60° are subtracted, which is equivalent to choosing another reciprocal lattice vector for $\vec{k}_2$ so that it makes an angle within ±30° with $\vec{k}_1$.

8.4.2. Period for super-superlattice

All possible values for λ_3 are plotted in Fig. 8.6(a), as a function of ϕ_1 and ϕ_2, by using Eq. (8.1) with the new parameters. Theoretically λ_3 varies from below 1 nm to infinity, but one finds values larger than 14 nm only for small twist angles, as shown in Fig. 8.6(b). For most angles λ_3 is very small, which explains why MSLs with periods larger than 14 nm have not been reported in previous studies, where only one hBN layer was aligned intentionally to the graphene layer.

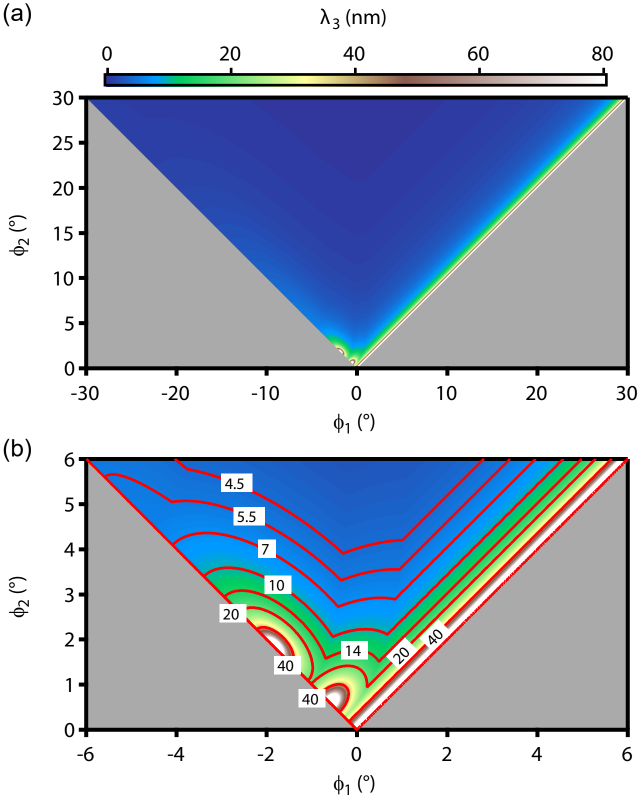

Figure 8.6. **(a)** λ_3 plotted as a function of ϕ_1 and ϕ_2 for all possible twist angles. **(b)** Zoom-in of **(a)** for small twist angles. Numbers on the contour lines indicate the values of λ_3 in nm.

Most of Fig. 8.6(b) can be understood intuitively. On the line of the right diagonal with $\phi_1 \equiv \phi_2$, we have $\lambda_1 = \lambda_2$ and $\theta_1 = \theta_2$, therefore $\phi_3 = 0$, which results in $\lambda_3 = \infty$. This case is similar to the twisted bilayer graphene with a twist angle of 0, which does not form a MSL (or a MSL with infinitely large period). On the diagonal line in the left part with $\phi_1 \equiv -\phi_2$, one has $\lambda_1 = \lambda_2$, but $\theta_1 = -\theta_2$. As $|\phi_1| = |\phi_2|$ increases, $\theta_1 = -\theta_2$ evolves. Therefore ϕ_3 can have non-zero values, resulting in different λ_3 values. This case is again similar to the twisted bilayer graphene, but with a tunable twist angle. Whenever the difference of the orientation of the top 2L-MSL and the bottom 2L-MSL becomes multiples of 60° (i.e. $\theta_1 = -\theta_2 = 30^\circ$ or 60°), the arrangement is equivalent to the full alignment of the two 2L-MSL due to the 60° rotational symmetry of the MSLs. In this case, ϕ_3 is reset to 0, therefore λ_3 diverges, giving rise to the two maxima, which is equivalent to the diagonal on the right part. The kinks on the contour lines come from the 60° rotational symmetry of the lattices, where $|\phi_3| = 30^\circ$.

8.4.3. Comparison to measurements

We now compare this simple model to our experiments. From the SDPs at $n_{s_A} \approx \pm 2.4 \times 10^{12}\,\mathrm{cm}^{-2}$, we calculate the corresponding moiré period $\lambda_1 \approx 13.2\,\mathrm{nm}$ and the twist angle $|\phi_1| \approx 0.34^\circ$. Similarly, for the extrapolated SDP at $n_{s_B} \approx -5.2 \times 10^{12}\,\mathrm{cm}^{-2}$, we obtain $\lambda_2 \approx 9\,\mathrm{nm}$ and $|\phi_2| \approx 1.2^\circ$. The two twist angles give us two points in the map in Fig. 8.6(b): ∼17.2 nm for (0.34°, 1.2°) and ∼27.1 nm for (−0.34°, 1.2°). The ∼17.2 nm matches very well the value ∼17.3 nm extracted from the new-generation SDPs at $n_{s_C} \approx \pm 1.4 \times 10^{12}\,\mathrm{cm}^{-2}$ in the transport measurement, which confirms that the new-generation SDPs come from the 3L-MSL.

8.5. Measurements on a second sample

We fabricated five hBN/graphene/hBN heterostructures in total, two of which exhibit 3L-MSL features. The fabrication details are given in the appendix E. Further data from other devices of the first heterostructure and devices of the second heterostructure, including bilayer graphene devices, are also presented in the appendix E, which all show similar characteristics. Here, we show the measurements of a device on the second sample as an example, which has a 3L-MSL with $\lambda_3 \approx 29.6\,\mathrm{nm}$.

The two-terminal differential conductance of a second device is plotted as a function of n in Fig. 8.7(a). In addition to the MDP, one pair of SDPs appear symmetrically at $n \approx \pm 2.9 \times 10^{12}\,\mathrm{cm}^{-2}$, resulting from a graphene/hBN MSL with $\lambda \approx 12\,\mathrm{nm}$ and $\phi \approx 0.6^\circ$. Another SDP appears at $n \approx -0.48 \times 10^{12}\,\mathrm{cm}^{-2}$. There are also filling factors fanning out from this SDP as shown in Fig.8.7(b).

This density corresponds to a superlattice with $\lambda \approx 29.6\,\text{nm}$, which we attribute to the 3L-MSL. With these parameters and Fig. 8.6(b), we can deduce back the parameters of the other graphene/hBN MSL to be $\phi \approx 1.1^\circ$ or -1.1° and $\lambda \approx 9.5\,\text{nm}$, corresponding to a density of $n \approx \pm 4.6 \times 10^{12}\,\text{cm}^{-2}$. This twist angle is in good agreement with our alignment precision.

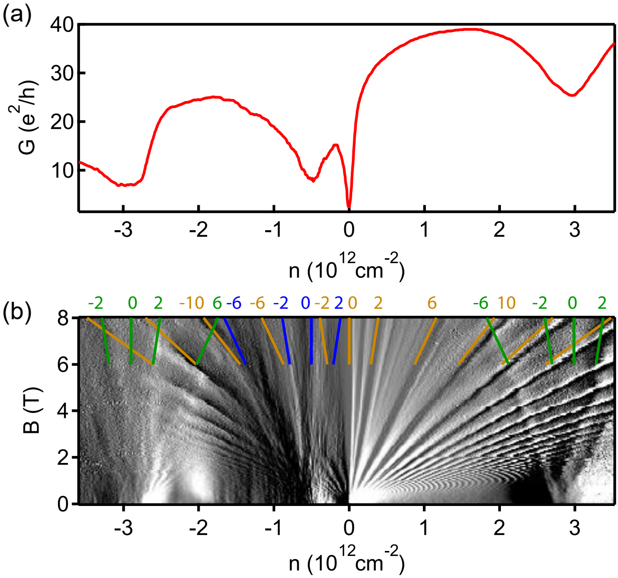

Figure 8.7. Measurements of a second device. (a) Two-terminal differential conductance G as a function of n. **(b)** $\mathrm{d}G/\mathrm{d}n$ as a function of n and B of the same device. Filling factors are indicated on top of the diagram. The bending and instability/noise of the filling factors at higher densities is due to the gate leak.

8.6. Conclusion and outlook

In conclusion, we have demonstrated the emergence of a new generation of MSLs in fully encapsulated graphene devices with aligned top and bottom hBN layers. In these devices we find three different superlattice periods, one of which is larger than the maximum graphene/hBN moiré period, which we attribute to the combined top and bottom hBN potential modulation. Whereas our model describes qualitatively the densities where these 3L-MSL features occur, the precise nature of the band structure distortions is unknown. The alignment of both hBN layers to graphene opens new possibilities for graphene band structure engineering, therefore providing motivation for further studies. Our new approach of MSL engineering is not limited to graphene with hBN, but applies to two-dimensional materials in general, such as twisted trilayer graphene, graphene with transition metal dichalcogenides, etc., which might open a new direction in “twistronics” [263, 264].

Recently, the 3L-MSL feature was reported in another experimental study as well [265], and was also studied theoretically [266], which agrees well with our findings.

9 Summary and Outlook

To summarize, we have successfully developed routes to engineer the electronic properties of graphene, either by controllable strain or by double moiré superlattices. A new platform that combines in situ strain tuning and transport experiments was developed. With this platform, various strain effects were found in different transport measurements at low temperatures. In addition, we discovered a new generation of moiré superlattices in double aligned hBN/graphene/hBN heterostructures.

In chapter 5 and Ref. [166], we demonstrated deterministic and reproducible in situ strain tuning in hBN-encapsulated graphene. Different strain fields can be achieved by varying the device geometries. Spatially resolved Raman spectroscopy was used to demonstrate that a fairly homogeneous strain field was achieved in a rectangular device while a strain gradient was realized with a trapezoidal device geometry. In first transport experiments, it was shown that the on-substrate approach avoided the bending-induced gate capacitance change, which is crucial for studying strain effects in transport experiments.

Although the hBN-encapsulation improves the sample quality significantly, it does not always result in an exceptionally high carrier mobility. In chapter 6 and Ref. [184], we investigated the influence of random strain fluctuations on carrier mobility of graphene. We demonstrated an in situ reduction of the random strain fluctuations in individual encapsulated graphene devices by increasing the average strain. In low-temperature transport measurements, a substantial enhancement of the carrier mobility was observed while the residual doping reduced significantly when the average strain was increased in the graphene. The unambiguous linear correlation between $1/\mu$ and n_0 reveals that random strain fluctuations are the dominant scattering mechanism limiting the mobility in most hBN-supported graphene devices. These findings were further substantiated by Raman spectroscopy, where a decrease of the 2D peak linewidth with increasing average strain was observed before the average strain induced broadening dominated. The absence of mobility enhancement in devices with ultra higher mobilities implies that either the reduction of random strain fluctuations is not possible in such devices, or another scattering mechanism becomes dominant.

In chapter 7, different strain effects in various transport experiments were presented and discussed. First, a strain-induced scalar potential was observed, which manifested as a constant shift of the conductance curves in gate voltage. The extracted strain value from this shift is consistent with the Raman measurements. In conductance fluctuations measurements, a clear systematic shift of the fluctuation features in magnetic field was found in a trapezoidal device, which might be related to a strain-induced pseudomagnetic field. In transverse magnetic focusing experiments on a trapezoidal device, the mobility enhancement with strain manifested as a magnitude increase of the focusing peaks because of the enhanced ballistic transport. A systematic shift of the whole focusing features in magnetic field with strain was also observed, which might be associated with the pseudomagnetic field as well. Furthermore, a significant position change of the focusing peaks in the magnetic field/gate voltage map with strain was observed, where the Fermi velocity renormalization might play a role. So far, a thorough understanding of these effects is still lacking. Further magnetic focusing experiments with square/rectangular devices might help to resolve the puzzles. In the quantum Hall regime, the trapezoidal devices showed a completely different behavior with strain from that of the square devices. No further strain effects except the scalar potential were observed for square devices, while dramatic changes of the quantum Hall plateaus with strain were found for trapezoidal devices. These findings are not compatible with the simple picture one would expect for pseudomagnetic field that acts on the two valleys with opposite signs. For future experiments, a scanning technique that maps the charge carrier distribution in the devices might help to understand the implication of the geometries. Furthermore, theoretical investigations of strain effects on electron-electron interactions in graphene might provide useful information for interpreting the strain effects on the quantum Hall plateaus.

In fully hBN-encapsulated graphene devices, a new generation of moiré superlattices emerges when both the top and the bottom hBN layers are aligned to the graphene lattice, which was demonstrated with transport experiments in chapter 8 and Ref. [180]. Three different superlattice periods were found in these devices, two of which originates from the alignment of each hBN layer. The third one has a period larger than the maximum graphene/hBN moiré period ($\sim$14 nm), which was attributed to the super-superlattice formed by the other two moiré superlattices. A simple model based on geometrical analysis was provided to describe the densities where such super-superlattice occur. The alignment of both hBN layers to graphene allows one to artificially create an even wider spectrum of electronic properties in graphene.

Outlook

First, our new approach of band structure engineering with super-superlattice is not limited to graphene with hBN, but applies to 2D materials in general, which might open a new direction in “twistronics” [263, 264]. Doubly aligned heterostructures, such as twisted trilayer graphene or graphene with transition metal dichalcogenides, might give rise to new physical phenomena.

Second, microscopic corrugations are most likely present in other 2D materials as well, which leads to random strain fluctuations. If such strain fluctuations limit the carrier mobility in those materials the same way as in graphene, our method of increasing the mobility by in situ straining might also be applicable in this case.

The Lifshitz transition in bilayer graphene is a transition of the Fermi surface topology from a single circle to four disconnected circles near the charge neutrality point [84]. It has been predicted that strain can tune the Lifshitz transition in bilayer graphene [57]. A uniaxial strain of 1% would be enough to induce observable strain effects [267], which is within the capability of our straining method.

Furthermore, interesting strain effects have been predicted for graphene devices with superconducting contacts. It has been shown in a theoretical study that strain can induce a $0-\pi$ transition in a zigzag graphene nanoribbon Josephson junction [268]. The supercurrent at the charge neutrality point has been demonstrated theoretically to be strain tunable [269]. The supercurrent can even be turned on/off with a cutoff strain, depending on the strain direction with respect to the crystallographic direction of graphene [270].

Last but certainly not least, our in situ straining method is not limited to graphene, but also suitable for studying strain effects in other 2D materials and complex vdW heterostructures.

Bibliography

[1] R. Peierls, Annales de l'institut Henri Poincaré **5**, 177 (1935).

[2] L. D. Landau, Phys. Z. Sowjetunion **11**, 26 (1937).

[3] K. S. Novoselov, Science **306**, 666 (2004).

[4] A. K. Geim and K. S. Novoselov, Nature Materials **6**, 183 (2007).

[5] R. R. Nair, P. Blake, A. N. Grigorenko, K. S. Novoselov, T. J. Booth, T. Stauber, N. M. R. Peres, and A. K. Geim, Science **320**, 1308 (2008).

[6] J. S. Bunch, S. S. Verbridge, J. S. Alden, A. M. van der Zande, J. M. Parpia, H. G. Craighead, and P. L. McEuen, Nano Lett. **8**, 2458 (2008).

[7] A. K. Geim, Science **324**, 1530 (2009).

[8] A. A. Balandin, Nature Materials **10**, 569 (2011).

[9] P. R. Wallace, Phys. Rev. **71**, 622 (1947).

[10] K. S. Novoselov, A. K. Geim, S. V. Morozov, D. Jiang, M. I. Katsnelson, I. V. Grigorieva, S. V. Dubonos, and A. A. Firsov, Nature **438**, 197 (2005).

[11] Y. Zhang, Y.-W. Tan, H. L. Stormer, and P. Kim, Nature **438**, 201 (2005).

[12] M. I. Katsnelson, K. S. Novoselov, and A. K. Geim, Nature Physics **2**, 620 (2006).

[13] A. F. Young and P. Kim, Nature Physics **5**, 222 (2009).

[14] N. Stander, B. Huard, and D. Goldhaber-Gordon, Phys. Rev. Lett. **102**, 026807 (2009).

[15] F. V. Tikhonenko, D. W. Horsell, R. V. Gorbachev, and A. K. Savchenko, Phys. Rev. Lett. **100**, 056802 (2008).

[16] F. V. Tikhonenko, A. A. Kozikov, A. K. Savchenko, and R. V. Gorbachev, Phys. Rev. Lett. **103**, 226801 (2009).

[17] S. V. Morozov, K. S. Novoselov, M. I. Katsnelson, F. Schedin, D. C. Elias, J. A. Jaszczak, and A. K. Geim, Phys. Rev. Lett. **100**, 016602 (2008).

[18] A. S. Mayorov, R. V. Gorbachev, S. V. Morozov, L. Britnell, R. Jalil, L. A. Ponomarenko, P. Blake, K. S. Novoselov, K. Watanabe, T. Taniguchi, and A. K. Geim, Nano Lett. **11**, 2396 (2011).

[19] F. Schwierz, Nature Nanotechnology **5**, 487 (2010).

[20] S. Konschuh, M. Gmitra, and J. Fabian, Phys. Rev. B **82**, 245412 (2010).

[21] A. H. Castro Neto, F. Guinea, N. M. R. Peres, K. S. Novoselov, and A. K. Geim, Rev. Mod. Phys. **81**, 109 (2009).

[22] L. Britnell, R. V. Gorbachev, R. Jalil, B. D. Belle, F. Schedin, M. I. Katsnelson, L. Eaves, S. V. Morozov, A. S. Mayorov, N. M. R. Peres, A. H. C. Neto, J. Leist, A. K. Geim, L. A. Ponomarenko, and K. S. Novoselov, Nano Letters **12**, 1707 (2012).

[23] K. F. Mak, C. Lee, J. Hone, J. Shan, and T. F. Heinz, Phys. Rev. Lett. **105**, 136805 (2010).

[24] X. Xi, Z. Wang, W. Zhao, J.-H. Park, K. T. Law, H. Berger, L. Forró, J. Shan, and K. F. Mak, Nature Physics **12**, 139 (2015).

[25] S. Tang, C. Zhang, D. Wong, Z. Pedramrazi, H.-Z. Tsai, C. Jia, B. Moritz, M. Claassen, H. Ryu, S. Kahn, J. Jiang, H. Yan, M. Hashimoto, D. Lu, R. G. Moore, C.-C. Hwang, C. Hwang, Z. Hussain, Y. Chen, M. M. Ugeda, Z. Liu, X. Xie, T. P. Devereaux, M. F. Crommie, S.-K. Mo, and Z.-X. Shen, Nature Physics **13**, 683 (2017).

[26] Z. Fei, T. Palomaki, S. Wu, W. Zhao, X. Cai, B. Sun, P. Nguyen, J. Finney, X. Xu, and D. H. Cobden, Nature Physics **13**, 677 (2017).

[27] S. Wu, V. Fatemi, Q. D. Gibson, K. Watanabe, T. Taniguchi, R. J. Cava, and P. Jarillo-Herrero, Science **359**, 76 (2018).

[28] B. Huang, G. Clark, E. Navarro-Moratalla, D. R. Klein, R. Cheng, K. L. Seyler, D. Zhong, E. Schmidgall, M. A. McGuire, D. H. Cobden, W. Yao, D. Xiao, P. Jarillo-Herrero, and X. Xu, Nature **546**, 270 (2017).

[29] Z. Wang, C. Tang, R. Sachs, Y. Barlas, and J. Shi, Phys. Rev. Lett. **114**, 016603 (2015).

[30] J. C. Leutenantsmeyer, A. A. Kaverzin, M. Wojtaszek, and B. J. van Wees, 2D Materials **4**, 014001 (2016).

[31] D. K. Efetov, L. Wang, C. Handschin, K. B. Efetov, J. Shuang, R. Cava, T. Taniguchi, K. Watanabe, J. Hone, C. R. Dean, and P. Kim, Nature Physics **12**, 328 (2015).

[32] L. Bretheau, J. I.-J. Wang, R. Pisoni, K. Watanabe, T. Taniguchi, and P. Jarillo-Herrero, Nature Physics **13**, 756 (2017).

[33] Z. Wang, D. Ki, H. Chen, H. Berger, A. H. MacDonald, and A. F. Morpurgo, Nature Communications **6** (2015).

[34] Z. Wang, D.-K. Ki, J. Y. Khoo, D. Mauro, H. Berger, L. S. Levitov, and A. F. Morpurgo, Phys. Rev. X **6**, 041020 (2016).

[35] L. A. Ponomarenko, R. V. Gorbachev, G. L. Yu, D. C. Elias, R. Jalil, A. A. Patel, A. Mishchenko, A. S. Mayorov, C. R. Woods, J. R. Wallbank, M. Mucha-Kruczynski, B. A. Piot, M. Potemski, I. V. Grigorieva, K. S. Novoselov, F. Guinea, V. I. Fal'ko, and A. K. Geim, Nature **497**, 594 (2013).

[36] C. R. Dean, L. Wang, P. Maher, C. Forsythe, F. Ghahari, Y. Gao, J. Katoch, M. Ishigami, P. Moon, M. Koshino, T. Taniguchi, K. Watanabe, K. L. Shepard, J. Hone, and P. Kim, Nature **497**, 598 (2013).

[37] B. Hunt, J. D. Sanchez-Yamagishi, A. F. Young, M. Yankowitz, B. J. LeRoy, K. Watanabe, T. Taniguchi, P. Moon, M. Koshino, P. Jarillo-Herrero, and R. C. Ashoori, Science **340**, 1427 (2013).

[38] G. L. Yu, R. V. Gorbachev, J. S. Tu, A. V. Kretinin, Y. Cao, R. Jalil, F. Withers, L. A. Ponomarenko, B. A. Piot, M. Potemski, D. C. Elias, X. Chen, K. Watanabe, T. Taniguchi, I. V. Grigorieva, K. S. Novoselov, V. I. Fal'ko, A. K. Geim, and A. Mishchenko, Nature Physics **10**, 525 (2014).

[39] L. Wang, Y. Gao, B. Wen, Z. Han, T. Taniguchi, K. Watanabe, M. Koshino, J. Hone, and C. R. Dean, Science **350**, 1231 (2015).

[40] Y. Cao, V. Fatemi, S. Fang, K. Watanabe, T. Taniguchi, E. Kaxiras, and P. Jarillo-Herrero, Nature **556**, 43 (2018).

[41] Y. Cao, V. Fatemi, A. Demir, S. Fang, S. L. Tomarken, J. Y. Luo, J. D. Sanchez-Yamagishi, K. Watanabe, T. Taniguchi, E. Kaxiras, R. C. Ashoori, and P. Jarillo-Herrero, Nature **556**, 80 (2018).

[42] C. Lee, X. Wei, J. W. Kysar, and J. Hone, Science **321**, 385 (2008).

[43] V. M. Pereira, A. H. Castro Neto, and N. M. R. Peres, Phys. Rev. B **80**, 045401 (2009).

[44] F. Guinea, A. K. Geim, M. I. Katsnelson, and K. S. Novoselov, Phys. Rev. B **81**, 035408 (2010).

[45] F. Guinea, M. I. Katsnelson, and A. K. Geim, Nature Physics **6**, 30 (2009).

[46] S. Zhu, J. A. Stroscio, and T. Li, Phys. Rev. Lett. **115**, 245501 (2015).

[47] S. P. Milovanović and F. M. Peeters, Applied Physics Letters **109**, 203108 (2016).

[48] C. Yesilyurt, S. Ghee Tan, G. Liang, and M. B. A. Jalil, AIP Advances **6**, 056303 (2016).

[49] B. Uchoa and Y. Barlas, Phys. Rev. Lett. **111**, 046604 (2013).

[50] S. Das Sarma, S. Adam, E. H. Hwang, and E. Rossi, Rev. Mod. Phys. **83**, 407 (2011).

[51] M. O. Goerbig, Rev. Mod. Phys. **83**, 1193 (2011).

[52] T. Ihn, *Semiconductor Nanostructures* (Oxford University Press, 2010).

[53] H. Raza, ed., *Graphene Nanoelectronics* (Springer Berlin Heidelberg, 2012).

[54] R. Beams, L. G. Cançado, and L. Novotny, Journal of Physics: Condensed Matter **27**, 083002 (2015).

[55] C. Handschin, *Quantum transport in encapsulated graphene p-n junctions*, Ph.D. thesis, University of Basel (2017).

[56] M. S. Dresselhaus and G. Dresselhaus, Advances in Physics **51**, 1 (2002).

[57] A. Varlet, M. Mucha-Kruczyński, D. Bischoff, P. Simonet, T. Taniguchi, K. Watanabe, V. Fal'ko, T. Ihn, and K. Ensslin, Synthetic Metals **210**, 19 (2015).

[58] E. McCann, K. Kechedzhi, V. I. Fal'ko, H. Suzuura, T. Ando, and B. L. Altshuler, Phys. Rev. Lett. **97**, 146805 (2006).

[59] T. Ando, J. Phys. Soc. Jpn. **75**, 074716 (2006).

[60] K. Nomura and A. H. MacDonald, Phys. Rev. Lett. **98**, 076602 (2007).

[61] E. H. Hwang, S. Adam, and S. Das Sarma, Phys. Rev. Lett. **98**, 186806 (2007).

[62] S. Adam, E. H. Hwang, V. M. Galitski, and S. DasSarma, Proc. Natl. Acad. Sci. U.S.A. **104**, 18392 (2007).

[63] J.-H. Chen, C. Jang, S. Adam, M. S. Fuhrer, E. D. Williams, and M. Ishigami, Nature Physics **4**, 377 (2008).

[64] J.-H. Chen, C. Jang, S. Xiao, M. Ishigami, and M. S. Fuhrer, Nature Nanotechnology **3**, 206 (2008).

[65] X. Hong, K. Zou, and J. Zhu, Phys. Rev. B **80**, 241415(R) (2009).

[66] M. Katsnelson and A. Geim, Phil. Trans. R. Soc. A **366**, 195 (2008).

[67] N. J. G. Couto, D. Costanzo, S. Engels, D.-K. Ki, K. Watanabe, T. Taniguchi, C. Stampfer, F. Guinea, and A. F. Morpurgo, Phys. Rev. X **4**, 041019 (2014).

[68] B. Terrés, L. A. Chizhova, F. Libisch, J. Peiro, D. Jörger, S. Engels, A. Girschik, K. Watanabe, T. Taniguchi, S. V. Rotkin, J. Burgdörfer, and C. Stampfer, Nature Communications **7** (2016).

[69] T. Taychatanapat, K. Watanabe, T. Taniguchi, and P. Jarillo-Herrero, Nature Physics **9**, 225 (2013).

[70] M. Lee, J. R. Wallbank, P. Gallagher, K. Watanabe, T. Taniguchi, V. I. Fal'ko, and D. Goldhaber-Gordon, Science **353**, 1526 (2016).

[71] P. Rickhaus, P. Makk, M.-H. Liu, E. Tóvári, M. Weiss, R. Maurand, K. Richter, and C. Schönenberger, Nature Communications **6** (2015).

[72] A. L. Grushina, D.-K. Ki, and A. F. Morpurgo, Applied Physics Letters **102**, 223102 (2013).

[73] T. Taychatanapat, J. Y. Tan, Y. Yeo, K. Watanabe, T. Taniguchi, and B. Özyilmaz, Nature Communications **6** (2015).

[74] V. S. Tsoi, J. Bass, and P. Wyder, Rev. Mod. Phys. **71**, 1641 (1999).

[75] C. Beenakker and H. van Houten, in *Semiconductor Heterostructures and Nanostructures* (Elsevier, 1991) pp. 1–228.

[76] S. Zihlmann, *Spin and charge relaxation in graphene*, Ph.D. thesis, University of Basel (2018).

[77] E. H. Hall, American Journal of Mathematics **2**, 287 (1879).

[78] J. ichi Wakabayashi and S. Kawaji, Journal of the Physical Society of Japan **44**, 1839 (1978).

[79] K. v. Klitzing, G. Dorda, and M. Pepper, Phys. Rev. Lett. **45**, 494 (1980).

[80] K. S. Novoselov, Z. Jiang, Y. Zhang, S. V. Morozov, H. L. Stormer, U. Zeitler, J. C. Maan, G. S. Boebinger, P. Kim, and A. K. Geim, Science **315**, 1379 (2007).

[81] A. F. Young, C. R. Dean, L. Wang, H. Ren, P. Cadden-Zimansky, K. Watanabe, T. Taniguchi, J. Hone, K. L. Shepard, and P. Kim, Nature Physics **8**, 550 (2012).

[82] D. A. Abanin and L. S. Levitov, Phys. Rev. B **78**, 035416 (2008).

[83] J. R. Williams, D. A. Abanin, L. DiCarlo, L. S. Levitov, and C. M. Marcus, Physical Review B **80** (2009).

[84] E. McCann and V. I. Fal'ko, Phys. Rev. Lett. **96**, 086805 (2006).

[85] P. L. de Andres and J. A. Vergés, Applied Physics Letters **93**, 171915 (2008).

[86] M. M. Fogler, F. Guinea, and M. I. Katsnelson, Phys. Rev. Lett. **101**, 226804 (2008).

[87] V. M. Pereira and A. H. Castro Neto, Phys. Rev. Lett. **103**, 046801 (2009).

[88] R. M. Ribeiro, V. M. Pereira, N. M. R. Peres, P. R. Briddon, and A. H. C. Neto, New Journal of Physics **11**, 115002 (2009).

[89] M. Mohr, K. Papagelis, J. Maultzsch, and C. Thomsen, Phys. Rev. B **80**, 205410 (2009).

[90] S.-M. Choi, S.-H. Jhi, and Y.-W. Son, Phys. Rev. B **81**, 081407 (2010).

[91] L. Landau and E. Lifshitz, *Theory of elasticity – course of theoretical physics, Vol 7.* (Springer, Berlin, 1986).

[92] F. Guinea, Solid State Communications **152**, 1437 (2012).

[93] H. Suzuura and T. Ando, Phys. Rev. B **65**, 235412 (2002).

[94] F. de Juan, M. Sturla, and M. A. H. Vozmediano, Phys. Rev. Lett. **108**, 227205 (2012).

[95] M. Oliva-Leyva and G. G. Naumis, Phys. Rev. B **88**, 085430 (2013).

[96] M. Oliva-Leyva and G. G. Naumis, Journal of Physics: Condensed Matter **26**, 125302 (2014).

[97] M. Oliva-Leyva and G. G. Naumis, Physics Letters A **379**, 2645 (2015).

[98] Y. Shimazaki, M. Yamamoto, I. V. Borzenets, K. Watanabe, T. Taniguchi, and S. Tarucha, Nature Physics **11**, 1032 (2015).

[99] R. V. Gorbachev, J. C. W. Song, G. L. Yu, A. V. Kretinin, F. Withers, Y. Cao, A. Mishchenko, I. V. Grigorieva, K. S. Novoselov, L. S. Levitov, and A. K. Geim, Science **346**, 448 (2014).

[100] M. Sui, G. Chen, L. Ma, W.-Y. Shan, D. Tian, K. Watanabe, T. Taniguchi, X. Jin, W. Yao, D. Xiao, and Y. Zhang, Nature Physics **11**, 1027 (2015).

[101] D. A. Abanin, A. V. Shytov, L. S. Levitov, and B. I. Halperin, Phys. Rev. B **79**, 035304 (2009).

[102] X.-P. Zhang, C. Huang, and M. A. Cazalilla, 2D Materials **4**, 024007 (2017).

[103] F. Cerdeira and M. Cardona, Phys. Rev. B **5**, 1440 (1972).

[104] M. Chandrasekhar, J. B. Renucci, and M. Cardona, Phys. Rev. B **17**, 1623 (1978).

[105] D. Olego and M. Cardona, Phys. Rev. B **24**, 7217 (1981).

[106] L. Malard, M. Pimenta, G. Dresselhaus, and M. Dresselhaus, Physics Reports **473**, 51 (2009).

[107] A. C. Ferrari and D. M. Basko, Nature Nanotechnology **8**, 235 (2013).

[108] M. Lazzeri, C. Attaccalite, L. Wirtz, and F. Mauri, Phys. Rev. B **78**, 081406 (2008).

[109] W. Kohn, Phys. Rev. Lett. **2**, 393 (1959).

[110] S. Piscanec, M. Lazzeri, F. Mauri, A. C. Ferrari, and J. Robertson, Phys. Rev. Lett. **93**, 185503 (2004).

[111] A. C. Ferrari, J. C. Meyer, V. Scardaci, C. Casiraghi, M. Lazzeri, F. Mauri, S. Piscanec, D. Jiang, K. S. Novoselov, S. Roth, and A. K. Geim, Phys. Rev. Lett. **97**, 187401 (2006).

[112] C. Thomsen and S. Reich, Phys. Rev. Lett. **85**, 5214 (2000).

[113] R. Saito, A. Jorio, A. G. Souza Filho, G. Dresselhaus, M. S. Dresselhaus, and M. A. Pimenta, Phys. Rev. Lett. **88**, 027401 (2001).

[114] M. A. Pimenta, G. Dresselhaus, M. S. Dresselhaus, L. G. Cançado, A. Jorio, and R. Saito, Phys. Chem. Chem. Phys. **9**, 1276 (2007).

[115] T. M. G. Mohiuddin, A. Lombardo, R. R. Nair, A. Bonetti, G. Savini, R. Jalil, N. Bonini, D. M. Basko, C. Galiotis, N. Marzari, K. S. Novoselov, A. K. Geim, and A. C. Ferrari, Phys. Rev. B **79**, 205433 (2009).

[116] D. Yoon, Y.-W. Son, and H. Cheong, Phys. Rev. Lett. **106**, 155502 (2011).

[117] O. Frank, M. Mohr, J. Maultzsch, C. Thomsen, I. Riaz, R. Jalil, K. S. Novoselov, G. Tsoukleri, J. Parthenios, K. Papagelis, L. Kavan, and C. Galiotis, ACS Nano **5**, 2231 (2011).

[118] M. Huang, H. Yan, T. F. Heinz, and J. Hone, Nano Lett. **10**, 4074 (2010).

[119] I. Polyzos, M. Bianchi, L. Rizzi, E. N. Koukaras, J. Parthenios, K. Papagelis, R. Sordan, and C. Galiotis, Nanoscale **7**, 13033 (2015).

[120] F. Colangelo, A. Pitanti, V. Mišeikis, C. Coletti, P. Pingue, D. Pisignano, F. Beltram, A. Tredicucci, and S. Roddaro, 2D Materials **5**, 045032 (2018).

[121] C. H. Johansson and J. O. Linde, Annalen der Physik **383**, 439 (1925).

[122] M. Yankowitz, J. Xue, D. Cormode, J. D. Sanchez-Yamagishi, K. Watanabe, T. Taniguchi, P. Jarillo-Herrero, P. Jacquod, and B. J. LeRoy, Nature Physics **8**, 382 (2012).

[123] P. Moon and M. Koshino, Phys. Rev. B **90**, 155406 (2014).

[124] R. Decker, Y. Wang, V. W. Brar, W. Regan, H.-Z. Tsai, Q. Wu, W. Gannett, A. Zettl, and M. F. Crommie, Nano Lett. **11**, 2291 (2011).

[125] J. Xue, J. Sanchez-Yamagishi, D. Bulmash, P. Jacquod, A. Deshpande, K. Watanabe, T. Taniguchi, P. Jarillo-Herrero, and B. J. LeRoy, Nature Materials **10**, 282 (2011).

[126] C.-H. Park, L. Yang, Y.-W. Son, M. L. Cohen, and S. G. Louie, Phys. Rev. Lett. **101**, 126804 (2008).

[127] J. R. Wallbank, A. A. Patel, M. Mucha-Kruczyński, A. K. Geim, and V. I. Fal'ko, Phys. Rev. B **87**, 245408 (2013).

[128] P. Wang, B. Cheng, O. Martynov, T. Miao, L. Jing, T. Taniguchi, K. Watanabe, V. Aji, C. N. Lau, and M. Bockrath, Nano Letters **15**, 6395 (2015).

[129] M. T. Greenaway, E. E. Vdovin, A. Mishchenko, O. Makarovsky, A. Patanè, J. R. Wallbank, Y. Cao, A. V. Kretinin, M. J. Zhu, S. V. Morozov, V. I. Fal'ko, K. S. Novoselov, A. K. Geim, T. M. Fromhold, and L. Eaves, Nature Physics **11**, 1057 (2015).

[130] C. Kumar, M. Kuiri, J. Jung, T. Das, and A. Das, Nano Letters **16**, 1042 (2016).

[131] K. Bolotin, K. Sikes, Z. Jiang, M. Klima, G. Fudenberg, J. Hone, P. Kim, and H. Stormer, Solid State Communications **146**, 351 (2008).

[132] X. Du, I. Skachko, A. Barker, and E. Y. Andrei, Nature Nanotechnology **3**, 491 (2008).

[133] K. I. Bolotin, K. J. Sikes, J. Hone, H. L. Stormer, and P. Kim, Phys. Rev. Lett. **101**, 096802 (2008).

[134] N. Tombros, A. Veligura, J. Junesch, J. Jasper van den Berg, P. J. Zomer, M. Wojtaszek, I. J. Vera Marun, H. T. Jonkman, and B. J. van Wees, Journal of Applied Physics **109**, 093702 (2011).

[135] R. Maurand, P. Rickhaus, P. Makk, S. Hess, E. Tóvári, C. Handschin, M. Weiss, and C. Schönenberger, Carbon **79**, 486 (2014).

[136] C. R. Dean, A. F. Young, I. Meric, C. Lee, L. Wang, S. Sorgenfrei, K. Watanabe, T. Taniguchi, P. Kim, K. L. Shepard, and J. Hone, Nature Nanotechnology **5**, 722 (2010).

[137] P. J. Zomer, S. P. Dash, N. Tombros, and B. J. van Wees, Applied Physics Letters **99**, 232104 (2011).

[138] L. Wang, I. Meric, P. Y. Huang, Q. Gao, Y. Gao, H. Tran, T. Taniguchi, K. Watanabe, L. M. Campos, D. A. Muller, J. Guo, P. Kim, J. Hone, K. L. Shepard, and C. R. Dean, Science **342**, 614 (2013).

[139] T. Taniguchi and K. Watanabe, Journal of Crystal Growth **303**, 525 (2007).

[140] Y. D. Kim, H. Kim, Y. Cho, J. H. Ryoo, C.-H. Park, P. Kim, Y. S. Kim, S. Lee, Y. Li, S.-N. Park, Y. S. Yoo, D. Yoon, V. E. Dorgan, E. Pop, T. F. Heinz, J. Hone, S.-H. Chun, H. Cheong, S. W. Lee, M.-H. Bae, and Y. D. Park, Nature Nanotechnology **10**, 676 (2015).

[141] P. Rickhaus, R. Maurand, M.-H. Liu, M. Weiss, K. Richter, and C. Schönenberger, Nature Communications **4** (2013).

[142] P. Rickhaus, *Electron optics in ballistic graphene*, Ph.D. thesis, University of Basel (2015).

[143] P. J. Zomer, M. H. D. Guimarães, J. C. Brant, N. Tombros, and B. J. van Wees, Applied Physics Letters **105**, 013101 (2014).

[144] J. Moreland and J. W. Ekin, Journal of Applied Physics **58**, 3888 (1985).

[145] C. J. Muller, J. M. van Ruitenbeek, and L. J. de Jongh, Phys. Rev. Lett. **69**, 140 (1992).

[146] J. M. van Ruitenbeek, A. Alvarez, I. Piñeyro, C. Grahmann, P. Joyez, M. H. Devoret, D. Esteve, and C. Urbina, Review of Scientific Instruments **67**, 108 (1996).

[147] S. A. G. Vrouwe, E. van der Giessen, S. J. van der Molen, D. Dulic, M. L. Trouwborst, and B. J. van Wees, Phys. Rev. B **71**, 035313 (2005).

[148] J. Gramich, *Andreev and spin transport in carbon nanotube quantum dot hybrid devices*, Ph.D. thesis, University of Basel (2016).

[149] I. Žutić, J. Fabian, and S. Das Sarma, Rev. Mod. Phys. **76**, 323 (2004).

[150] F. Freitag, M. Weiss, R. Maurand, J. Trbovic, and C. Schönenberger, Solid State Communications **152**, 2053 (2012).

[151] D.-K. Ki and A. F. Morpurgo, Nano Lett. **13**, 5165 (2013).

[152] D. A. Abanin, S. V. Morozov, L. A. Ponomarenko, R. V. Gorbachev, A. S. Mayorov, M. I. Katsnelson, K. Watanabe, T. Taniguchi, K. S. Novoselov, L. S. Levitov, and A. K. Geim, Science **332**, 328 (2011).

[153] D. Xiao, W. Yao, and Q. Niu, Phys. Rev. Lett. **99**, 236809 (2007).

[154] D. Xiao, M.-C. Chang, and Q. Niu, Rev. Mod. Phys. **82**, 1959 (2010).

[155] A. McRae, G. Wei, and A. Champagne, Phys. Rev. Applied **11**, 054019 (2019).

[156] E. McCann, Phys. Rev. B **74**, 161403 (2006).

[157] F. Freitag, J. Trbovic, M. Weiss, and C. Schönenberger, Phys. Rev. Lett. **108**, 076602 (2012).

[158] B. E. Feldman, J. Martin, and A. Yacoby, Nature Physics **5**, 889 (2009).

[159] J. Velasco, L. Jing, W. Bao, Y. Lee, P. Kratz, V. Aji, M. Bockrath, C. N. Lau, C. Varma, R. Stillwell, D. Smirnov, F. Zhang, J. Jung, and A. H. MacDonald, Nature Nanotechnology **7**, 156 (2012).

[160] W. Bao, J. Velasco, F. Zhang, L. Jing, B. Standley, D. Smirnov, M. Bockrath, A. H. MacDonald, and C. N. Lau, Proc. Natl. Acad. Sci. U.S.A. **109**, 10802 (2012).

[161] J. N. Leaw, H.-K. Tang, P. Sengupta, F. F. Assaad, I. F. Herbut, and S. Adam, Phys. Rev. B **100**, 125116 (2019).

[162] M. Jung, P. Rickhaus, S. Zihlmann, A. Eichler, P. Makk, and C. Schönenberger, Nanoscale **11**, 4355 (2019).

[163] M. T. Allen, O. Shtanko, I. C. Fulga, A. R. Akhmerov, K. Watanabe, T. Taniguchi, P. Jarillo-Herrero, L. S. Levitov, and A. Yacoby, Nature Physics **12**, 128 (2015).

[164] Y.-T. Cui, B. Wen, E. Y. Ma, G. Diankov, Z. Han, F. Amet, T. Taniguchi, K. Watanabe, D. Goldhaber-Gordon, C. R. Dean, and Z.-X. Shen, Phys. Rev. Lett. **117**, 186601 (2016).

[165] M. J. Zhu, A. V. Kretinin, M. D. Thompson, D. A. Bandurin, S. Hu, G. L. Yu, J. Birkbeck, A. Mishchenko, I. J. Vera-Marun, K. Watanabe, T. Taniguchi, M. Polini, J. R. Prance, K. S. Novoselov, A. K. Geim, and M. B. Shalom, Nature Communications **8** (2017).

[166] L. Wang, S. Zihlmann, A. Baumgartner, J. Overbeck, K. Watanabe, T. Taniguchi, P. Makk, and C. Schönenberger, Nano Lett. **19**, 4097 (2019).

[167] H. H. Pérez Garza, E. W. Kievit, G. F. Schneider, and U. Staufer, Nano Lett. **14**, 4107 (2014).

[168] C. S. C. Downs, A. Usher, and J. Martin, Journal of Applied Physics **119**, 194305 (2016).

[169] M. Goldsche, J. Sonntag, T. Khodkov, G. J. Verbiest, S. Reichardt, C. Neumann, T. Ouaj, N. von den Driesch, D. Buca, and C. Stampfer, Nano Lett. **18**, 1707 (2018).

[170] F. Guan and X. Du, Nano Lett. **17**, 7009 (2017).

[171] H. Shioya, S. Russo, M. Yamamoto, M. F. Craciun, and S. Tarucha, Nano Lett. **15**, 7943 (2015).

[172] Y. Jiang, J. Mao, J. Duan, X. Lai, K. Watanabe, T. Taniguchi, and E. Y. Andrei, Nano Lett. **17**, 2839 (2017).

[173] Y. Liu, J. N. B. Rodrigues, Y. Z. Luo, L. Li, A. Carvalho, M. Yang, E. Laksono, J. Lu, Y. Bao, H. Xu, S. J. R. Tan, Z. Qiu, C. H. Sow, Y. P. Feng, A. H. C. Neto, S. Adam, J. Lu, and K. P. Loh, Nature Nanotechnology **13**, 828 (2018).

[174] Y. Zhang, M. Heiranian, B. Janicek, Z. Budrikis, S. Zapperi, P. Y. Huang, H. T. Johnson, N. R. Aluru, J. W. Lyding, and N. Mason, Nano Lett. **18**, 2098 (2018).

[175] J. E. Lee, G. Ahn, J. Shim, Y. S. Lee, and S. Ryu, Nature Communications **3**, 1024 (2012).

[176] C. Neumann, S. Reichardt, P. Venezuela, M. Drögeler, L. Banszerus, M. Schmitz, K. Watanabe, T. Taniguchi, F. Mauri, B. Beschoten, S. V. Rotkin, and C. Stampfer, Nature Communications **6**, 8429 (2015).

[177] N. S. Mueller, S. Heeg, M. P. Alvarez, P. Kusch, S. Wasserroth, N. Clark, F. Schedin, J. Parthenios, K. Papagelis, C. Galiotis, M. Kalbáč, A. Vijayaraghavan, U. Huebner, R. Gorbachev, O. Frank, and S. Reich, 2D Materials **5**, 015016 (2017).

[178] G. Froehlicher and S. Berciaud, Phys. Rev. B **91**, 205413 (2015).

[179] C. Androulidakis, E. N. Koukaras, M. Poss, K. Papagelis, C. Galiotis, and S. Tawfick, Phys. Rev. B **97**, 241414 (2018).

[180] L. Wang, S. Zihlmann, M.-H. Liu, P. Makk, K. Watanabe, T. Taniguchi, A. Baumgartner, and C. Schönenberger, Nano Lett. **19**, 2371 (2019).

[181] H. J. Conley, B. Wang, J. I. Ziegler, R. F. Haglund, S. T. Pantelides, and K. I. Bolotin, Nano Lett. **13**, 3626 (2013).

[182] K. He, C. Poole, K. F. Mak, and J. Shan, Nano Lett. **13**, 2931 (2013).

[183] C. R. Zhu, G. Wang, B. L. Liu, X. Marie, X. F. Qiao, X. Zhang, X. X. Wu, H. Fan, P. H. Tan, T. Amand, and B. Urbaszek, Phys. Rev. B **88**, 121301 (2013).

[184] L. Wang, P. Makk, S. Zihlmann, A. Baumgartner, D. I. Indolese, K. Watanabe, T. Taniguchi, and C. Schönenberger, Phys. Rev. Lett. **124**, 157701 (2020).

[185] K. I. Bolotin, F. Ghahari, M. D. Shulman, H. L. Stormer, and P. Kim, Nature **462**, 196 (2009).

[186] X. Du, I. Skachko, F. Duerr, A. Luican, and E. Y. Andrei, Nature **462**, 192 (2009).

[187] C. R. Dean, A. F. Young, P. Cadden-Zimansky, L. Wang, H. Ren, K. Watanabe, T. Taniguchi, P. Kim, J. Hone, and K. L. Shepard, Nature Physics **7**, 693 (2011).

[188] S. Chen, Z. Han, M. M. Elahi, K. M. M. Habib, L. Wang, B. Wen, Y. Gao, T. Taniguchi, K. Watanabe, J. Hone, A. W. Ghosh, and C. R. Dean, Science **353**, 1522 (2016).

[189] S. Engels, B. Terrés, A. Epping, T. Khodkov, K. Watanabe, T. Taniguchi, B. Beschoten, and C. Stampfer, Phys. Rev. Lett. **113**, 126801 (2014).

[190] J. C. Meyer, A. K. Geim, M. I. Katsnelson, K. S. Novoselov, T. J. Booth, and S. Roth, Nature **446**, 60 (2007).

[191] N. Abedpour, M. Neek-Amal, R. Asgari, F. Shahbazi, N. Nafari, and M. R. R. Tabar, Phys. Rev. B **76**, 195407 (2007).

[192] A. Fasolino, J. H. Los, and M. I. Katsnelson, Nature Materials **6**, 858 (2007).

[193] M. Ishigami, J. H. Chen, W. G. Cullen, M. S. Fuhrer, and E. D. Williams, Nano Lett. **7**, 1643 (2007).

[194] E. Stolyarova, K. T. Rim, S. Ryu, J. Maultzsch, P. Kim, L. E. Brus, T. F. Heinz, M. S. Hybertsen, and G. W. Flynn, Proc. Natl. Acad. Sci. U.S.A. **104**, 9209 (2007).

[195] V. Geringer, M. Liebmann, T. Echtermeyer, S. Runte, M. Schmidt, R. Rückamp, M. C. Lemme, and M. Morgenstern, Phys. Rev. Lett. **102**, 076102 (2009).

[196] W. G. Cullen, M. Yamamoto, K. M. Burson, J. H. Chen, C. Jang, L. Li, M. S. Fuhrer, and E. D. Williams, Phys. Rev. Lett. **105**, 215504 (2010).

[197] S. V. Morozov, K. S. Novoselov, M. I. Katsnelson, F. Schedin, L. A. Ponomarenko, D. Jiang, and A. K. Geim, Phys. Rev. Lett. **97**, 016801 (2006).

[198] M. B. Lundeberg and J. A. Folk, Phys. Rev. Lett. **105**, 146804 (2010).

[199] L. Banszerus, H. Janssen, M. Otto, A. Epping, T. Taniguchi, K. Watanabe, B. Beschoten, D. Neumaier, and C. Stampfer, 2D Materials **4**, 025030 (2017).

[200] S. Zihlmann, A. W. Cummings, J. H. Garcia, M. Kedves, K. Watanabe, T. Taniguchi, C. Schönenberger, and P. Makk, Phys. Rev. B **97**, 075434 (2018).

[201] S. Zihlmann, P. Makk, M. K. Rehmann, L. Wang, M. Kedves, D. I. Indolese, K. Watanabe, T. Taniguchi, D. M. Zumbühl, and C. Schönenberger, in preparation .

[202] T. Low and F. Guinea, Nano Lett. **10**, 3551 (2010).

[203] N. Levy, S. A. Burke, K. L. Meaker, M. Panlasigui, A. Zettl, F. Guinea, A. H. C. Neto, and M. F. Crommie, Science **329**, 544 (2010).

[204] N. N. Klimov, S. Jung, S. Zhu, T. Li, C. A. Wright, S. D. Solares, D. B. Newell, N. B. Zhitenev, and J. A. Stroscio, Science **336**, 1557 (2012).

[205] H. Yan, Y. Sun, L. He, J.-C. Nie, and M. H. W. Chan, Phys. Rev. B **85**, 035422 (2012).

[206] D. Guo, T. Kondo, T. Machida, K. Iwatake, S. Okada, and J. Nakamura, Nature Communications **3** (2012).

[207] J. Lu, A. H. C. Neto, and K. P. Loh, Nature Communications **3**, 823 (2012).

[208] Y. Wu, D. Zhai, C. Pan, B. Cheng, T. Taniguchi, K. Watanabe, N. Sandler, and M. Bockrath, Nano Lett. **18**, 64 (2018).

[209] M. Huang, T. A. Pascal, H. Kim, W. A. Goddard, and J. R. Greer, Nano Lett. **11**, 1241 (2011).

[210] B. J. van Wees, H. van Houten, C. W. J. Beenakker, J. G. Williamson, L. P. Kouwenhoven, D. van der Marel, and C. T. Foxon, Phys. Rev. Lett. **60**, 848 (1988).

[211] C. Handschin, P. Makk, P. Rickhaus, M.-H. Liu, K. Watanabe, T. Taniguchi, K. Richter, and C. Schönenberger, Nano Lett. **17**, 328 (2017).

[212] S. Ono and K. Sugihara, Journal of the Physical Society of Japan **21**, 861 (1966).

[213] M. Gibertini, A. Tomadin, F. Guinea, M. I. Katsnelson, and M. Polini, Phys. Rev. B **85**, 201405 (2012).

[214] J. L. Mañes, Phys. Rev. B **76**, 045430 (2007).

[215] M. B. Lundeberg, J. Renard, and J. A. Folk, Phys. Rev. B **86**, 205413 (2012).

[216] H. van Houten, C. W. J. Beenakker, J. G. Williamson, M. E. I. Broekaart, P. H. M. van Loosdrecht, B. J. van Wees, J. E. Mooij, C. T. Foxon, and J. J. Harris, Phys. Rev. B **39**, 8556 (1989).

[217] H. Polshyn, H. Zhou, E. M. Spanton, T. Taniguchi, K. Watanabe, and A. F. Young, Phys. Rev. Lett. **121**, 226801 (2018).

[218] Y. Zeng, J. I. A. Li, S. A. Dietrich, O. M. Ghosh, K. Watanabe, T. Taniguchi, J. Hone, and C. R. Dean, Phys. Rev. Lett. **122**, 137701 (2019).

[219] R. B. Laughlin, Phys. Rev. B **23**, 5632 (1981).

[220] B. Huckestein, Rev. Mod. Phys. **67**, 357 (1995).

[221] Y. Zhang, Z. Jiang, J. P. Small, M. S. Purewal, Y.-W. Tan, M. Fazlollahi, J. D. Chudow, J. A. Jaszczak, H. L. Stormer, and P. Kim, Phys. Rev. Lett. **96**, 136806 (2006).

[222] Z. Jiang, Y. Zhang, H. L. Stormer, and P. Kim, Phys. Rev. Lett. **99**, 106802 (2007).

[223] J. G. Checkelsky, L. Li, and N. P. Ong, Phys. Rev. Lett. **100**, 206801 (2008).

[224] D. S. Wei, T. van der Sar, S. H. Lee, K. Watanabe, T. Taniguchi, B. I. Halperin, and A. Yacoby, Science **362**, 229 (2018).

[225] F. Amet, J. R. Williams, K. Watanabe, T. Taniguchi, and D. Goldhaber-Gordon, Phys. Rev. Lett. **112**, 196601 (2014).

[226] T. Low and J. Appenzeller, Phys. Rev. B **80**, 155406 (2009).

[227] D. Weiss, K. V. Klitzing, K. Ploog, and G. Weimann, Europhys. Lett. **8**, 179 (1989).

[228] D. Weiss, M. L. Roukes, A. Menschig, P. Grambow, K. von Klitzing, and G. Weimann, Phys. Rev. Lett. **66**, 2790 (1991).

[229] D. Pfannkuche and R. R. Gerhardts, Phys. Rev. B **46**, 12606 (1992).

[230] D. Ferry, Prog. Quantum Electron. **16**, 251 (1992).

[231] T. Schlösser, K. Ensslin, J. P. Kotthaus, and M. Holland, Europhys. Lett. **33**, 683 (1996).

[232] C. Albrecht, J. H. Smet, D. Weiss, K. von Klitzing, R. Hennig, M. Langenbuch, M. Suhrke, U. Rössler, V. Umansky, and H. Schweizer, Phys. Rev. Lett. **83**, 2234 (1999).

[233] C. Albrecht, J. H. Smet, K. von Klitzing, D. Weiss, V. Umansky, and H. Schweizer, Phys. Rev. Lett. **86**, 147 (2001).

[234] M. C. Geisler, J. H. Smet, V. Umansky, K. von Klitzing, B. Naundorf, R. Ketzmerick, and H. Schweizer, Phys. Rev. Lett. **92**, 256801 (2004).

[235] C.-H. Park, L. Yang, Y.-W. Son, M. L. Cohen, and S. G. Louie, Nature Physics **4**, 213 (2008).

[236] M. Barbier, F. M. Peeters, P. Vasilopoulos, and J. M. Pereira, Phys. Rev. B **77**, 115446 (2008).

[237] L. Brey and H. A. Fertig, Phys. Rev. Lett. **103**, 046809 (2009).

[238] J. Sun, H. A. Fertig, and L. Brey, Phys. Rev. Lett. **105**, 156801 (2010).

[239] P. Burset, A. L. Yeyati, L. Brey, and H. A. Fertig, Phys. Rev. B **83**, 195434 (2011).

[240] C. Ortix, L. Yang, and J. van den Brink, Phys. Rev. B **86**, 081405 (2012).

[241] S. Dubey, V. Singh, A. K. Bhat, P. Parikh, S. Grover, R. Sensarma, V. Tripathi, K. Sengupta, and M. M. Deshmukh, Nano Lett. **13**, 3990 (2013).

[242] M. Drienovsky, F.-X. Schrettenbrunner, A. Sandner, D. Weiss, J. Eroms, M.-H. Liu, F. Tkatschenko, and K. Richter, Phys. Rev. B **89**, 115421 (2014).

[243] M. Drienovsky, J. Joachimsmeyer, A. Sandner, M.-H. Liu, T. Taniguchi, K. Watanabe, K. Richter, D. Weiss, and J. Eroms, Phys. Rev. Lett. **121**, 026806 (2018).

[244] Z. Sun, C. L. Pint, D. C. Marcano, C. Zhang, J. Yao, G. Ruan, Z. Yan, Y. Zhu, R. H. Hauge, and J. M. Tour, Nature Communications **2**, 559 (2011).

[245] J. Bai, X. Zhong, S. Jiang, Y. Huang, and X. Duan, Nature Nanotechnology **5**, 190 (2010).

[246] A. Sandner, T. Preis, C. Schell, P. Giudici, K. Watanabe, T. Taniguchi, D. Weiss, and J. Eroms, Nano Lett. **15**, 8402 (2015).

[247] R. Yagi, R. Sakakibara, R. Ebisuoka, J. Onishi, K. Watanabe, T. Taniguchi, and Y. Iye, Phys. Rev. B **92**, 195406 (2015).

[248] Y. Zhang, Y. Kim, M. J. Gilbert, and N. Mason, npj 2D Materials and Applications **2**, 31 (2018).

[249] C. Forsythe, X. Zhou, K. Watanabe, T. Taniguchi, A. Pasupathy, P. Moon, M. Koshino, P. Kim, and C. R. Dean, Nature Nanotechnology **13**, 566 (2018).

[250] M. Kindermann, B. Uchoa, and D. L. Miller, Phys. Rev. B **86**, 115415 (2012).

[251] J. C. W. Song, A. V. Shytov, and L. S. Levitov, Phys. Rev. Lett. **111**, 266801 (2013).

[252] R. Krishna Kumar, X. Chen, G. H. Auton, A. Mishchenko, D. A. Bandurin, S. V. Morozov, Y. Cao, E. Khestanova, M. Ben Shalom, A. V. Kretinin, K. S. Novoselov, L. Eaves, I. V. Grigorieva, L. A. Ponomarenko, V. I. Fal'ko, and A. K. Geim, Science **357**, 181 (2017).

[253] C. R. Woods, L. Britnell, A. Eckmann, R. S. Ma, J. C. Lu, H. M. Guo, X. Lin, G. L. Yu, Y. Cao, R. Gorbachev, A. V. Kretinin, J. Park, L. A. Ponomarenko, M. I. Katsnelson, Y. Gornostyrev, K. Watanabe, T. Taniguchi, C. Casiraghi, H.-J. Gao, A. K. Geim, and K. Novoselov, Nature Physics **10**, 451 (2014).

[254] Z. Shi, C. Jin, W. Yang, L. Ju, J. Horng, X. Lu, H. A. Bechtel, M. C. Martin, D. Fu, J. Wu, K. Watanabe, T. Taniguchi, Y. Zhang, X. Bai, E. Wang, G. Zhang, and F. Wang, Nature Physics **10**, 743 (2014).

[255] E. Wang, X. Lu, S. Ding, W. Yao, M. Yan, G. Wan, K. Deng, S. Wang, G. Chen, L. Ma, J. Jung, A. V. Fedorov, Y. Zhang, G. Zhang, and S. Zhou, Nature Physics **12**, 1111 (2016).

[256] E. M. Spanton, A. A. Zibrov, H. Zhou, T. Taniguchi, K. Watanabe, M. P. Zaletel, and A. F. Young, Science **360**, 62 (2018).

[257] D. I. Indolese, R. Delagrange, P. Makk, J. R. Wallbank, K. Watanabe, T. Taniguchi, and C. Schönenberger, Phys. Rev. Lett. **121**, 137701 (2018).

[258] Y. Cao, J. Y. Luo, V. Fatemi, S. Fang, J. D. Sanchez-Yamagishi, K. Watanabe, T. Taniguchi, E. Kaxiras, and P. Jarillo-Herrero, Phys. Rev. Lett. **117**, 116804 (2016).

[259] K. Kim, A. DaSilva, S. Huang, B. Fallahazad, S. Larentis, T. Taniguchi, K. Watanabe, B. J. LeRoy, A. H. MacDonald, and E. Tutuc, Proc. Natl. Acad. Sci. U.S.A. **114**, 3364 (2017).

[260] P. Rickhaus, J. Wallbank, S. Slizovskiy, R. Pisoni, H. Overweg, Y. Lee, M. Eich, M.-H. Liu, K. Watanabe, T. Taniguchi, T. Ihn, and K. Ensslin, Nano Lett. **18**, 6725 (2018).

[261] M. Yankowitz, S. Chen, H. Polshyn, Y. Zhang, K. Watanabe, T. Taniguchi, D. Graf, A. F. Young, and C. R. Dean, Science **363**, 1059 (2019).

[262] G. Chen, M. Sui, D. Wang, S. Wang, J. Jung, P. Moon, S. Adam, K. Watanabe, T. Taniguchi, S. Zhou, M. Koshino, G. Zhang, and Y. Zhang, Nano Lett. **17**, 3576 (2017).

[263] S. Carr, D. Massatt, S. Fang, P. Cazeaux, M. Luskin, and E. Kaxiras, Phys. Rev. B **95**, 075420 (2017).

[264] R. Ribeiro-Palau, C. Zhang, K. Watanabe, T. Taniguchi, J. Hone, and C. R. Dean, Science **361**, 690 (2018).

[265] N. R. Finney, M. Yankowitz, L. Muraleetharan, K. Watanabe, T. Taniguchi, C. R. Dean, and J. Hone, Nature Nanotechnology (2019), 10.1038/s41565-019-0547-2.

[266] M. Anđelković, S. P. Milovanović, L. Covaci, and F. M. Peeters, arXiv e-prints , arXiv:1910.00345 (2019).

[267] M. Mucha-Kruczyński, I. L. Aleiner, and V. I. Fal'ko, Phys. Rev. B **84**, 041404 (2011).

[268] J. Zou and G. Jin, Applied Physics Letters **98**, 122106 (2011).

[269] M. Alidoust and J. Linder, Phys. Rev. B **84**, 035407 (2011).

[270] Y. Wang, Y. Liu, and B. Wang, Applied Physics Letters **103**, 182603 (2013).

[271] O. L. Blakslee, D. G. Proctor, E. J. Seldin, G. B. Spence, and T. Weng, Journal of Applied Physics **41**, 3373 (1970).

[272] D. Yoon, H. Moon, Y.-W. Son, G. Samsonidze, B. H. Park, J. B. Kim, Y. Lee, and H. Cheong, Nano Lett. **8**, 4270 (2008).

[273] A. Eckmann, J. Park, H. Yang, D. Elias, A. S. Mayorov, G. Yu, R. Jalil, K. S. Novoselov, R. V. Gorbachev, M. Lazzeri, A. K. Geim, and C. Casiraghi, Nano Lett. **13**, 5242 (2013).

A Fabrication Recipes

The fabrication techniques used in this thesis are discussed in chapter 3. This appendix provides details of the fabrication recipes.

A.1. Fabrication of LOR-based suspended graphene samples

A.1.1. Bottom gate structures

1. Pattern PMMA mask with E-beam (see section A.4.1).
2. Short oxygen plasma to remove resist residues.
3. Evaporation of 5 nm Ti and 40 nm Au.
4. Lift-off in xylene at 80 °C, rinse with hexane.
5. Repeat above procedures for deposition of 100 nm MgO as dielectric on gate structures to avoid gate leaks.

A.1.2. LOR coating and opening for bonding pads

Since wire bonding cannot be done on LOR, the bonding pads need to be deposited on SiO_2. In order to avoid disconnections between the leads (on LOR) and the bonding pads (on SiO_2), a "stair"-structure needs to be developed in LOR (See Ref. [142] for more details).

1. Spin coat 600 nm LOR 5A (2200 rpm, 45 s) and bake at 200 °C for 15 min.
2. Expose bonding pads with a base dose of $600\,\mu C\,cm^{-2}$ and a stepwise decrease (steps of $40\,\mu C\,cm^{-2}$) along the direction where the leads are expected to be.
3. Develop in ethyl-lactate for 2 min, wash thoroughly in xylene at 80 °C using a syringe, rinse in hexane.

A.1.3. Lithography on LOR

PMMA based E-beam patterning can be performed on top of the LOR with xylene as the developer and lift-off solvent and hexane as a rinsing solvent. E-gun evaporation of metallic leads (e.g. Ti/Au) is not suitable on LOR, as it exposes the LOR during evaporation. Therefore, thermal evaporation of Pd is used (see section A.6.1).

A.1.4. Suspension of graphene

- Expose LOR below graphene with 1100 µC cm^{-2}. This also leads to the suspension of the contacts.
- Develop in ethyl-lactate for 2 min, rinse in hexane, blow-dry with N$_2$.

A.2. Preparation of flexible substrate

1. Cut the 0.3 mm thick phosphor bronze plate into pieces of 5 cm × 5 cm.
2. Polish the surface with a lapping machine.
3. Spin coat polyimide with a two-step procedure:
   500 rpm/1 s/10 s
   2500 rpm/5 s/60 s.
4. Soft bake at 170 °C for 3 min.
5. Repeat spin coating and soft baking for two more times in order to get ticker film.
6. Polyimide curing: increase the temperature from 170 °C to 350 °C with rate 4 °C min^{-1}, bake at 350 °C for 30 min then switch off the hot plate, let it cool to room temperature.
7. Spin coat a thick PMMA layer (∼1 µm) to protect the polyimide surface before cutting into smaller pieces using a diamond wire saw.

A.3. Fabrication of encapsulated graphene

A.3.1. Wafer preparation and exfoliation

1. Dicing the fresh Si (with ∼285 nm) wafer into appropriate sizes (∼1 cm × 1 cm).
2. Blow with N$_2$.

3. Exfoliate graphene or hBN on the wafer and identify them with an optical microscopy.

4. UVO and heating treatment can be used to increase the exfoliation yield.

A.3.2. Assembly of hBN/graphene/hBN stacks

1. PC film preparation: drop caste PC solution (dissolved in chloroform with 9 wt%) on a glass slide. Use a second glass slide to press and slide against the first glass slide immediately. Let them dry in a fume hood.

2. Use a piece of scotch tape with a widow (~1 cm × 1 cm) cut in the center to transfer the dried PC film onto a PDMS stamp ~0.5 cm × 0.5 cm, which is mounted on a glass slide.

3. Pick up top hBN layer with the PC film at ~80 °C.

4. Pick up the graphene and the bottom hBN sequentially in the same way.

5. Place down the assembled stack onto the target substrate by heating to 150 °C to release the PC layer from the PDMS.

6. Remove PC film with chloroform (~1 h).

A.4. E-beam lithography and development

A.4.1. PMMA resist with xylene as developer

1. Spin-coat 420 nm PMMA and bake at 180 °C for 3 min.

2. Expose with E-beam ($V = 20\,\mathrm{keV}$, Dose $= 180\,\mu\mathrm{C/cm^2}$).

3. Develop in xylene for 2 min, rinse in hexane, blow-dry.

A.4.2. PMMA resist with cold-development

1. Spin-coat 420 nm PMMA and bake at 180 °C for 3 min.

2. Expose with E-beam ($V = 20\,\mathrm{keV}$; Dose $= 450\,\mu\mathrm{C/cm^2}$).

3. Cold-development in IPA:H_2O (ratio 7:3) at ~5 °C for 60 s, blow-dry.

A.5. Reactive ion etching

A.5.1. CHF_3:O_2 plasma

1. Parameters: CHF_3:O_2 (80 sccm/4 sccm), P =60 W, p =60 mTorr. This plasma is used to cut the stack with a controlled etching time for evaporating edge contacts.

2. Etching rates:

   hBN: ∼20 nm/min

   PMMA: <10 nm/min

   Polyimide: negligible

A.5.2. SF_6:Ar:O_2 plasma

1. Parameters: SF_6:Ar:O_2 (76 sccm/3.6 sccm/5 sccm), $P = 50$ W, $p = 25$ mTorr. This plasma is used to shape the stack.

2. Etching rates:

   hBN: >300 nm/min

   SiO_2: ∼30 nm/min

   PMMA: ∼80 nm/min

It is important to do a short O_2 plasma etching after each SF_6 plasma etching step to remove the cross-linked PMMA layer due to SF_6 plasma.

A.5.3. O_2 plasma

1. Parameters: O_2 (20 sccm), P =60 W, p =40 mTorr. This plasma is used to remove PMMA or to shape the graphene for suspended samples.

2. Etching rates:

   hBN: ∼20 nm/min

   PMMA: ∼100 nm/min

   graphene: several layers per minute

A.6. Metal evaporation

A.6.1. Pd leads

1. Type: Thermal evaporation

2. Pumping to base-pressure of $<2 \times 10^{-7}$ Pa
3. Heat the Pd source slowly to 1510 °C
4. Open shutter
5. Evaporate 60 nm (~0.06 Å/s)

A.6.2. Cr/Au leads

1. Type: E-beam evaporation
2. Pumping to base-pressure of $<2 \times 10^{-7}$ Pa
3. Evaporate away ~30 nm of Cr before opening the shutter, since the Cr-target oxidizes in ambient condition, where it is stored.
4. Open shutter
5. Evaporate 5 nm of Cr (0.7 Å/s to 1.2 Å/s)
6. Evaporate 110 nm of Au (0.7 Å/s to 1.2 Å/s)

B Further data and discussions of strain tuning in graphene

The aim of this appendix is to provide further fabrication details, data and discussions of strain tuning in graphene presented in chapter 5. First, the edge contact reinforcement is introduced. Second, the correlation between $\omega_{2\mathrm{D}}$ and ω_{G} is presented and discussed, followed by the FEM simulations. Furthermore, the transport measurements of the suspended encapsulated device is discussed in more detail.

B.1. Edge contact reinforcement

Since the strain is generated via the edge contacts, we use a small overlap to mechanically reinforce the contacts, as schematically shown in Fig. B.1. First, one EBL step is used to etch the top hBN down to ∼10 nm above the graphene, see Fig. B.1(b). In the second EBL step we open the mask ∼400 nm more so that it overlaps with the unetched top hBN and etch another ∼15 nm to cut the graphene for making the edge contacts (Cr/Au, 10 nm/110 nm), as depicted in Fig. B.1(c-d).

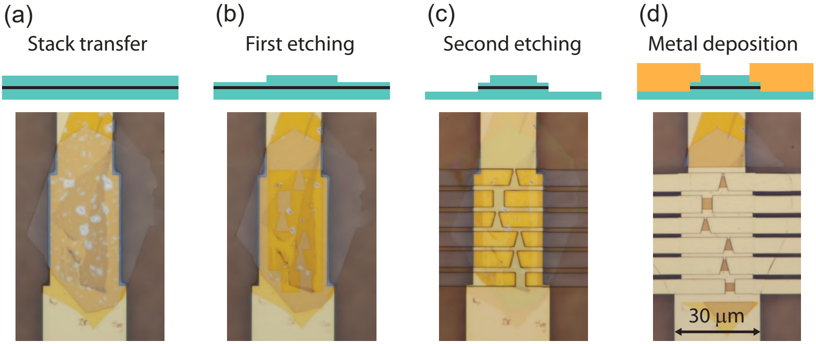

Figure B.1. Edge contact reinforcement. Schematics and corresponding micrographs of different fabrication steps. The overlaps near the edge contacts are designed for mechanical reinforcement.

B.2. Scatter plot of ω_{2D} versus ω_G

Here we discuss the inhomogeneity in the maps of Fig. 5.6 in section 5.4 by analyzing the scatter plots of ω_{2D} versus ω_G. Both strain and charge doping can induce a shift of the 2D and G peaks. For strain, the data points are expected to lie along the line with a slope of $\Delta\omega_{2D}/\Delta\omega_G \approx 2.2$ [169, 175–177] while the slope is expected to be around 0.55 for hole doping [178]. Our on-substrate encapsulated devices are predominately hole doped. In Fig. B.2(a), the data points of device A are spread along the strain axis, which corresponds to a strain variation of about 0.1% over the whole device area. With increasing ω_G, the data points shift globally along the strain axis while the spread along the strain axis does not change, which is in good agreement with a homogeneous external strain induced by the substrate bending. There is also a spread of the data points along the doping axis, which would correspond to a doping variation of $\sim 5 \times 10^{12}\,\mathrm{cm}^{-2}$ [178]. However, this doping variation is not realistic, because it is more than one order of magnitude higher than the typical residual doping in our devices. A typical Raman spectrum from one of the maps is shown in Fig. B.2(c), where the graphene G peak is not well resolved due to short integration time during the measurement. Therefore, we attribute the large spread of the data points along the doping axis to the uncertainties in extracting ω_G. For device B, in addition to the global shift, the spread of the data points along the strain axis extends with increasing ω_G (see Fig. B.2(b)), which is consistent with the externally induced strain gradient from the geometry design. In conclusion, the inhomogeneity in the maps in Fig. 5.6 in section 5.4 is mostly coming from long range strain variation.

B.3. FEM simulations of strain

Here we perform the strain simulations[1] for the two geometries given in section 5.4. We use Matlab's finite element method (FEM) modeling toolbox to solve the 2D partial differential equations in the plane strain mode to estimate the strain distribution in the limit of a continuous, homogeneous and isotropic medium. The elasticity parameters we use are a 2D Young's modulus of 340 N/m, a Poisson's ratio of 0.165 [42, 271], and no volume forces. We set the boundary conditions such that at the edge contacts (gray beams in Fig. B.3) are displaced by 10 nm in the direction of the gray arrows, and no normal forces act on all other boundaries. Since the bottom edge of device B is shorter than the top edge, for the same displacement the strain will be higher on the bottom edge than that on the top edge, which then results in the strain gradient. We plot the hydrostatic strain ($\varepsilon_{xx} + \varepsilon_{yy}$), the quantity expected to result in the shift of the Raman 2D-peak [177]. These settings reproduce

---

[1] The FEM simulations were performed by Andreas Baumgartner.

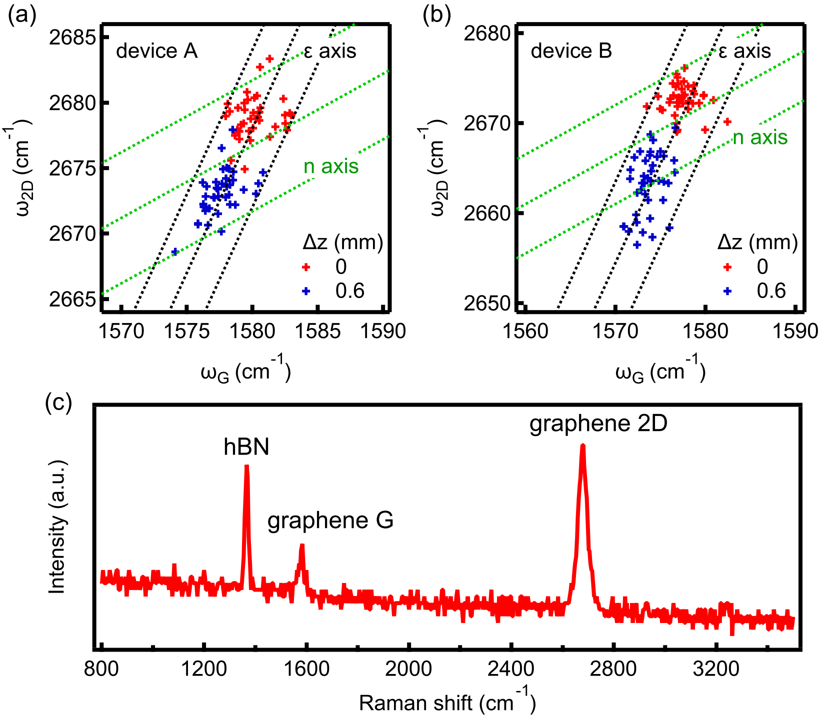

Figure B.2. Correlation between ω_{2D} and ω_G. Scatter plot of ω_{2D} versus ω_G at two different Δz values for device A **(a)** and device B **(b)** in section 5.4. Data points are taken from 40 different positions homogeneously distributed on each map. The $\Delta\omega_{2D}/\Delta\omega_G = 2.2$ lines (black dashed) correspond to the strain axis and the $\Delta\omega_{2D}/\Delta\omega_G = 0.55$ lines (green dashed) correspond to the hole doping axis.**(c)** Typical Raman spectrum from one of the maps.

the measured strain distributions quite well, which suggests a strong clamping mediated by the edge contacts. We note, however, that quantitatively, ε_{xx} alone resembles the Raman data more closely, which we tentatively attribute to the Raman laser being linearly polarized along the uniaxial strain direction (x-direction) [116, 118, 272].

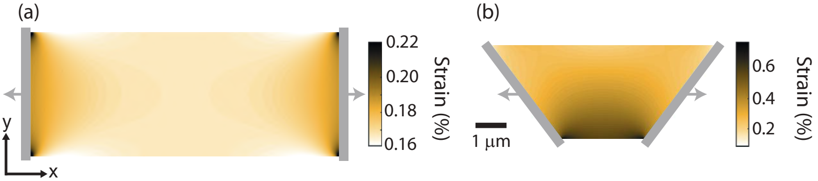

Figure B.3. FEM simulations of strain: for device A **(a)** and device B **(b)** in section 5.4.

B.4. Discussions on transport measurements of the suspended encapsulated device

The schematics of the encapsulated device discussed in section 5.4.6 is shown in Fig. 5.1(b). The Pd support is used to protect the LOR from UV exposure during the etching of the stack. In Fig. 5.12(c) of section 5.4.6, we note that the conductance is generally lower on the electron side for the suspended device compared to that of the on-substrate device. We attribute this to a region near the contacts, which is screened by the Pd and cannot be tuned by the bottom gate. It can form an additional p-n junction when the device is tuned to the electron side, which then suppresses the total conductance of the device.

Usually, in our on-substrate encapsulated devices, the graphene is hole doped at zero gate voltage. In the suspended encapsulated devices, the graphene is electron doped (see Fig. 5.12(c)), which is usually the case in suspended graphene devices fabricated with the LOR based suspension technique [135]. The electron doping might be attributed to LOR residuals.

C Further data and discussions on mobility enhancement experiments

This appendix contains additional information for the experiments presented in chapter 6, including reversibility of the mobility change with decreasing strain, the analysis of the mobility change on the hole side, another device showing mobility increase with strain and the parameters used for Raman measurements.

C.1. Geometry factor and reversibility of the strain induced mobility increase

A micrograph of the device discussed in chapter 6 is shown in Fig. C.1(a). The tapered geometry is intended for other experiments and is not relevant for the conclusions of this study. The dimensions of the device are shown in Fig. C.1(b). Assuming a homogeneous conductivity, the graphene can then be modeled as a set of parallel strips. With this, the geometry factor α for converting the conductance to conductivity can be calculated as:

$$G = \int_0^W \sigma \frac{dx}{L_1 + 2x \tan\theta},$$

where $\tan\theta = \frac{(L_2 - L_1)/2}{W}$, yielding $\sigma = \alpha G$ with $\alpha = \frac{L_2 - L_1}{W \ln(L_2/L_1)}$. Plugging the dimensions of this device, we obtain $\alpha = 1.28$.

The two-terminal differential conductance G is also measured for decreasing Δz, as shown in Fig. C.1(c). The conductance curves around the CNP become less steep for smaller Δz, indicating a decreasing mobility. The change from $\Delta z = 0.6\,\mathrm{mm}$ (red curve) to $\Delta z = 0.4\,\mathrm{mm}$ (orange curve) is very small, which can be attributed to the mechanical hysteresis of the setup when we turn from increasing Δz to decreasing Δz. The observation of decreasing mobility demonstrates that the mobility-increase effect presented in chapter 6 is reversible.

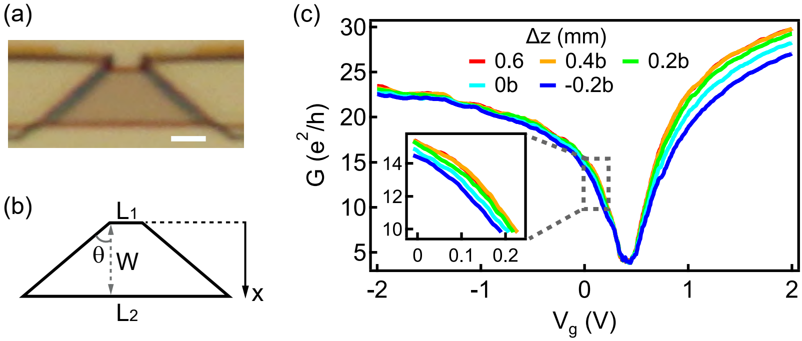

Figure C.1. Geometry factor and reversibility of mobility enhancement. (a) Micrograph of the measured device, scale bar: 1 µm. **(b)** Sketch of the device for calculating the geometry factor α, where $L_1 = 1\,\mu\text{m}$, $L_2 = 6.3\,\mu\text{m}$ and $W = 2.25\,\mu\text{m}$. **(c)** Two-terminal differential conductance G plotted as a function of gate voltage V_g for decreasing Δz. “b” stands for “decrease back”. The displacement Δz is defined relative to the mounting position, so negative value does not mean bending in the opposite direction. The inset shows the zoom-in to the hole side.

C.2. Analysis of the hole side

Here we present the results of the fitting on the hole side of Fig. 6.2(a). The extracted μ, n_0 and R_c are plotted for different Δz in Fig. C.2(a-c), respectively. When Δz is increased from 0 to 0.6 mm, the mobility increases gradually from $\sim$45 000 $\text{cm}^2\,\text{V}^{-1}\,\text{s}^{-1}$ to $\sim$54 000 $\text{cm}^2\,\text{V}^{-1}\,\text{s}^{-1}$ while the residual doping decreases gradually from $\sim 2.9 \times 10^{10}\,\text{cm}^{-2}$ to $\sim 2.1 \times 10^{10}\,\text{cm}^{-2}$. The contact resistance R_c is $\sim$1 kΩ (including $\sim$350 Ω line resistance), which is essentially constant and is higher than that on the electron side ($\sim$680 Ω). This is consistent with a p-n junction forming near the contacts which makes the mobility-increase effect less visible on the hole side. The (μ, n_0) pairs are plotted as $1/\mu$ versus n_0 in Fig. C.2(d). A linear fit yields a slope of $\sim 0.102 \times (h/e)$ and $\mu_0 \approx 102\,000\,\text{cm}^2\,\text{V}^{-1}\,\text{s}^{-1}$, both are consistent with the values extracted for the electron side in chapter 6.

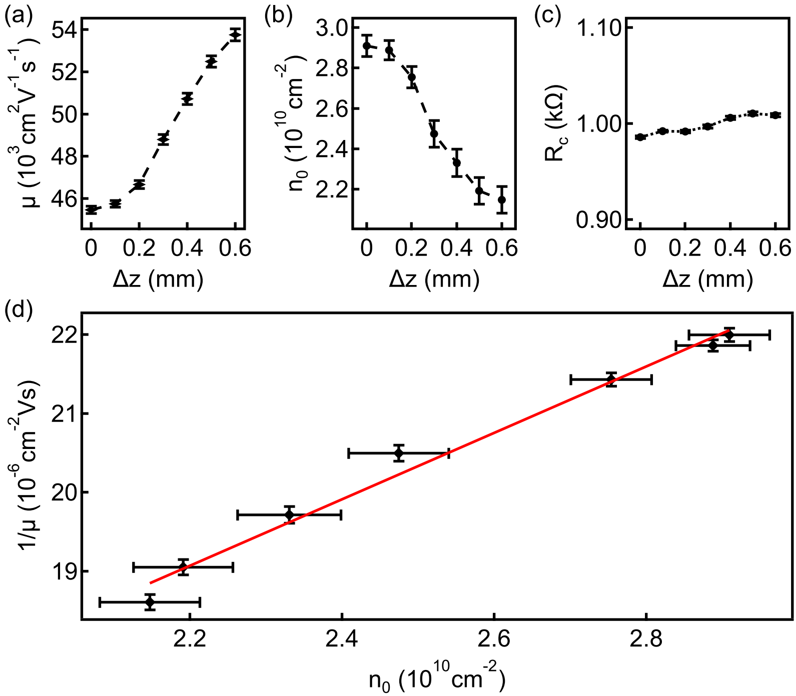

Figure C.2. Analysis on the hole side. Extracted **(a)** mobility μ, **(b)** residual doping n_0 and **(c)** contact resistance R_c (including ∼350 Ω line resistance) from fitting plotted as a function of Δz, respectively. The error bars are the standard errors from fits. The mobility μ shows a gradual increase while the residual doping n_0 shows a gradual decrease with increasing Δz. The contact resistance R_c stays essentially constant. **(d)** Same data as those of **(a)** and **(b)** plotted as $1/\mu$ versus n_0, showing a linear relation with a linear fit to the data, $1/\mu = (0.102 \pm 0.005) \times (h/e) n_0 + 1/\mu_0$, where $\mu_0 \approx 102\,000\,\mathrm{cm^2\,V^{-1}\,s^{-1}}$.

C.3. Second device with mobility-increase effect

The electron mobility of this device is around $70\,000\,\mathrm{cm^2\,V^{-1}\,s^{-1}}$, which shows a slight increase with increasing Δz, as plotted in Fig. C.3(a). The visibility of this effect on the hole side is suppressed by the higher contact resistance on this side and the additional conductance minimum at $V_\mathrm{g} \approx 1\,\mathrm{V}$, which originates from a double moiré superlattice effect in encapsulated graphene when both the top and the bottom hBN lattices are aligned to the graphene lattice [180]. In Raman measurements, the mean value of the center frequency $\bar{\omega}_\mathrm{2D}$ and the linewidth $\bar{\Gamma}_\mathrm{2D}$ of the 2D peak averaged over the whole device are plotted as a function of Δz in Fig. C.3(b,c), respectively. The value of $\bar{\omega}_\mathrm{2D}$ shows a linear decrease with increasing Δz, indicating an increasing average strain. For $\bar{\Gamma}_\mathrm{2D}$, it decreases first with Δz, implying reducing of the local strain fluctuations due to increasing average strain. The increase of $\bar{\Gamma}_\mathrm{2D}$ appears when the externally applied strain induced broadening of the 2D peak dominates. The overall large values of $\bar{\Gamma}_\mathrm{2D}$ come from the superlattice effect [273], which is also observed in transport measurements as shown in Fig. C.3(a).

C.4. Raman spectroscopy

After transport measurements at low temperature, we perform Raman measurements at room temperature to determine the strain if the device is still intact. The Raman setup is separate from the transport setup and sits in ambient conditions [166]. We use the commercially available confocal Raman system WiTec alpha300. All Raman spectra were acquired using a linearly polarized laser at a wavelength of 532 nm and a power of 1 mW. The laser spot size is $\sim$500 nm and the grating of the spectrometer is 600 grooves/mm.

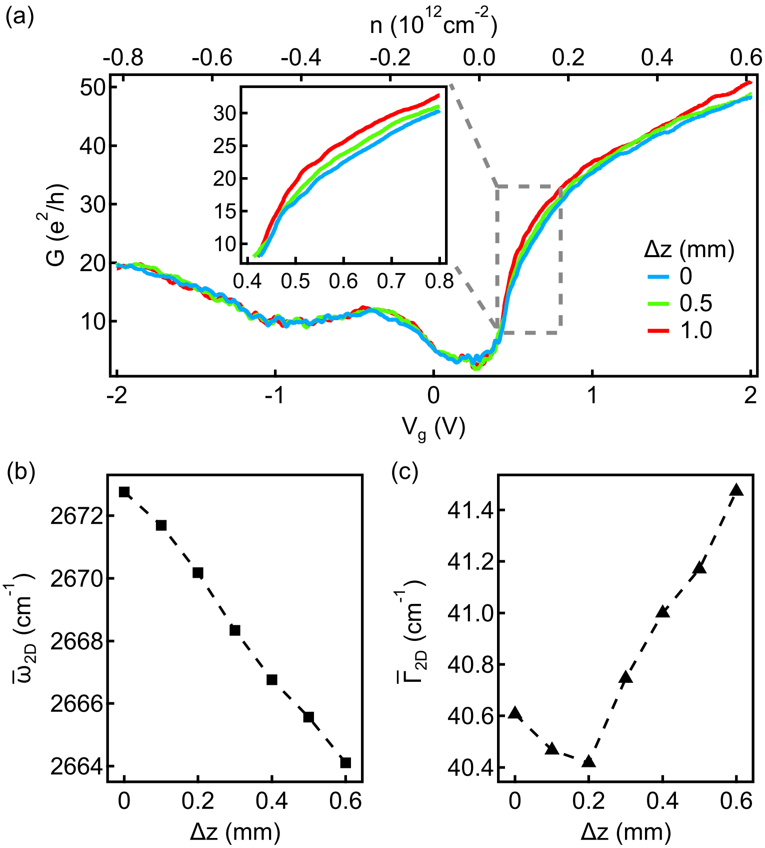

Figure C.3. Second device with mobility enhancement. (a) Two-terminal differential conductance G plotted as a function of gate voltage V_g for different Δz. The corresponding carrier density is shown on the top axis. **(b)** Averaged center frequency $\bar{\omega}_{2D}$ and **(c)** linewidth $\bar{\Gamma}_{2D}$ of the Raman 2D peak plotted as a function of Δz for the same device.

D Additional information and discussions on strain effects in various transport experiments

This appendix shows further measurements that support the discussions in chapter 7. First, strain effects on conductance fluctuations in gate voltage are presented and discussed for Sample2 A and Sample2 B. Second, two-terminal differential conductance of Sample3 B is shown for different Δz, followed by the discussion of the classical Hall effect and the effect of strain. Furthermore, a comparison of the quantum Hall effect between Sample3 B and a square device fabricated with the same stack is given.

D.1. Conductance fluctuations in gate voltage

The conductance fluctuations can be tuned by changing the charge carrier wavelength with an electric gating, which shifts the Fermi level in graphene. Strain can induce a scalar potential in graphene which acts effectively like gating. However, the scalar potentials achieved in our devices are relatively small and their effects on the conductance fluctuations are negligible, as can be seen in Fig. D.1. Most of the features are parallel to the Δz axis, suggesting vanishing strain dependence. This is in stark contrast to the observations shown in Fig. 7.3, where the conductance is plotted as a function of Δz and magnetic field. There it is found that within a similar Δz range the fluctuation patterns shift more than one full period.

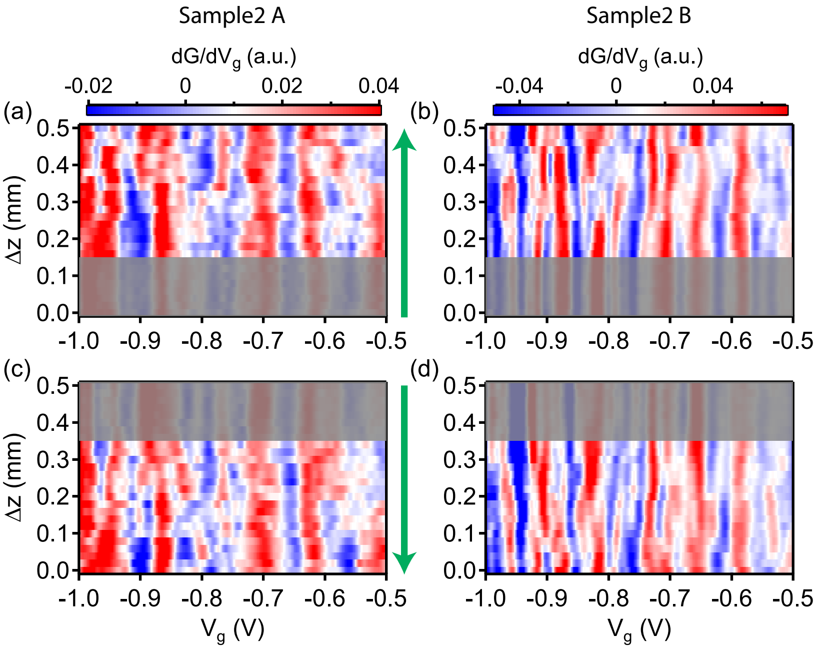

Figure D.1. Conductance fluctuations in gate voltage (a,b) Conductance fluctuations measured for a certain gate voltage range with increasing Δz for Sample2 A and B, respectively. A derivative in V_g is taken to remove the large conductance background. **(c,d)** The same as **(a,b)** for decreasing Δz. The mechanical hysteresis of the bending setup is marked with shaded boxes. The green arrows indicate the bending direction.

D.2. Classical Hall effect in Sample3 B

The two-terminal differential conductance of Sample3 B is plotted as a function of gate voltage for different Δz in Fig. D.2(a), where a mobility enhancement is observed with increasing strain.

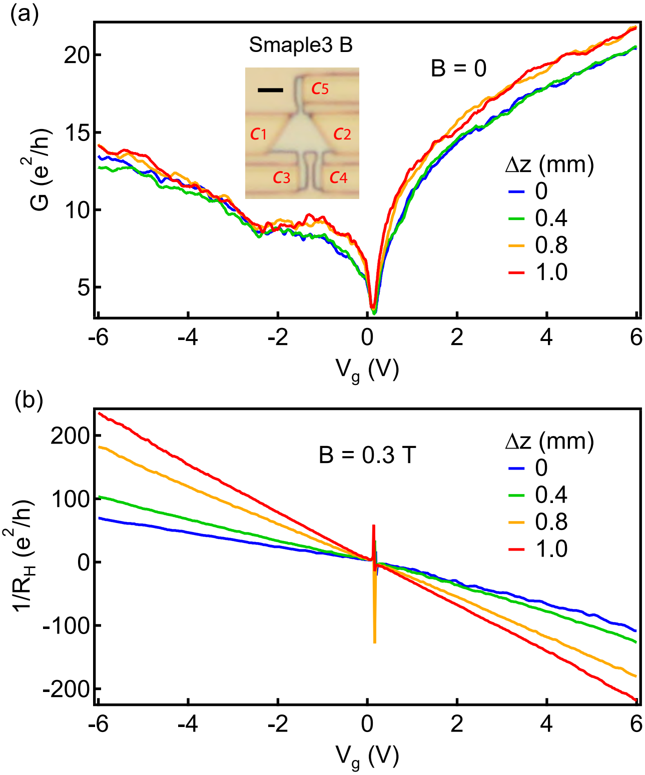

Figure D.2. Classical Hall effect in Sample3 B. (a) Two-terminal differential conductance G measured as a function of gate voltage V_g for different Δz. Inset: optical image of Sample3 B with scale bar corresponding to $2\,\mu\mathrm{m}$. **(b)** Hall conductance at $B = 0.3\,\mathrm{T}$ as a function of V_g for different Δz.

The Hall conductance $1/R_\mathrm{H} = en/B$ [52] measured as $I_{C_1C_2}/V_{C_3C_5}$ at $B = 0.3\,\mathrm{T}$ for different Δz is shown in Fig. D.2(b). Assuming a homogeneous carrier density regardless of the device geometry, a lever arm of $\sim 0.8 \times 10^{15}\,\mathrm{m}^{-2}\,\mathrm{V}^{-1}$ and $\sim 2.8 \times 10^{15}\,\mathrm{m}^{-2}\,\mathrm{V}^{-1}$ are extracted from the slope of the curves on the hole side for $\Delta z = 0$ and 1.0 mm, respectively. Such a big change of the lever arm with Δz is inconsistent with the measurements at $B = 0$ shown in Fig. D.2(a), where global transport through the whole device is measured. Since the Hall effect measurement is a local probe measurement, we therefore speculate that the carried density is inhomogeneous in the device, which might be caused by the device geometry [226], as discussed in section 7.6.3. However, the lever arm at $\Delta z = 1.0$ mm extracted here matches very well the one estimated from the plate capacitor model, which is consistent with the lever arm extracted from the quantum Hall effect of Sample3 A (see later), suggesting that the carrier density is homogeneous at $\Delta z = 1.0$ mm.

It seems the device is “abnormal” at $\Delta z = 0$ and the strain makes it “normal” at $\Delta z = 1.0$ mm, but how strain makes this change is not clear so far. This puzzling effect might also affect the quantitative interpretation of the strain effect observed in the transverse magnetic focusing experiments.

D.3. Comparison in quantum Hall regime

The two-terminal differential conductance of a square device (Sample3 A) fabricated from the same hBN/graphene/hBN stack of Sample3 B is shown as a function of gate voltage in Fig. D.3(a), where no significant effect is observed with Δz. In Fig. D.3(b), a comparison at $B = 9$ T between Sample3 A and Sample3 B is presented for different Δz. No strain effect is observed on this scale for Sample3 A, which is consistent with Sample1 A shown in section 7.6.1. The strain effect for Sample3 B is already discussed in section 7.6.3. The interesting finding here is that the curve of Sample3 B $\Delta z = 1.0$ mm is almost like that of Sample3 A, suggesting that Sample3 B really becomes “normal” at $\Delta z = 1.0$ mm, as discussed in the previous section.

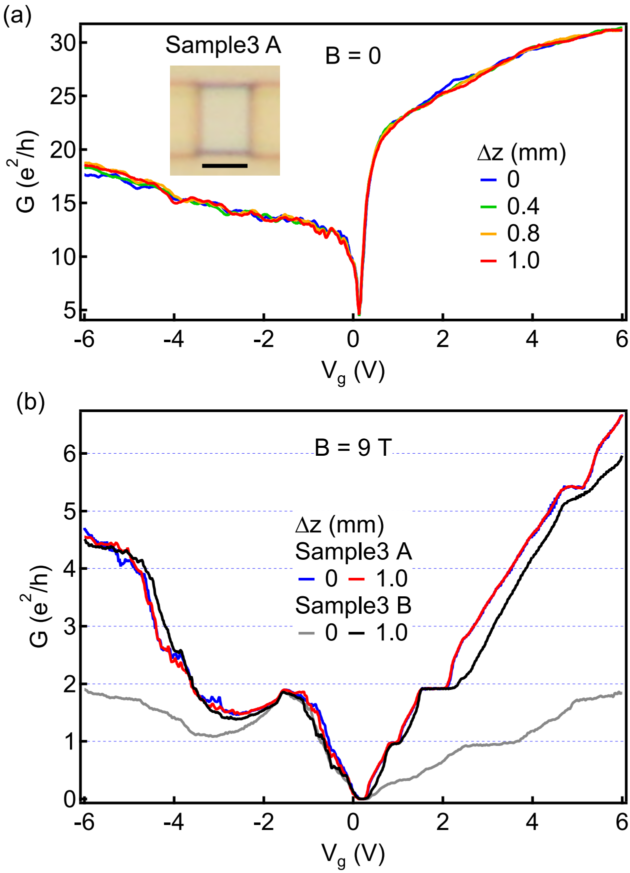

Figure D.3. Comparison in quantum Hall regime. (a) Two-terminal differential conductance G plotted as a function of gate voltage V_g for different Δz. Inset: optical image of Sample3 A with scale bar corresponding to 2 μm. **(b)** G of Sample3 A and Sample3 B as a function of V_g at $B = 9\,\mathrm{T}$ for different Δz.

E Further data and discussions of super-superlattice

This appendix provides supporting information for the experiments presented in chapter 8. First, additional information about fabrication is given. Then, further data of other devices from the first heterostructure (sample a) and data of devices from the second heterostructure (sample b) are presented.

E.1. Fabrication

We align hBN to graphene by aligning the straight edges of each layer. The probability for each alignment is 50%, because the straight edges can be along either zigzag or armchair direction. Since we need to align both hBN layers to graphene, the probability drops to 25%. We think that this is why only two out of five samples exhibit 3L-MSL features in the experiment. The stack is directly placed on the metallic gate, so the bottom hBN acts as the dielectric layer which is usually about 20-40nm thick in our case, resulting in a high gating efficiency.

E.2. Other devices of sample a

A flake with both monolayer and bilayer graphene as shown in Fig. E.1(a) was chosen for sample a. We fabricated six fully encapsulated devices out of this flake, with three monolayer devices and three bilayer devices. The different device geometries are designed for other experiments. The main device discussed in chapter 8 is device a2 in Fig. E.1(b). In the following we show the gate traces of all devices and the Landau fan diagram of monolayer device a3. Unfortunately, we do not have the complete data set for other devices due to a gate leak that appeared during the measurements.

In Fig. E.2, two-terminal differential conductance is plotted as a function of gate voltage for all devices. Each curve is offset by an individual V_0 in gate voltage in order to shift the MDP to zero gate voltage. All six devices spread over 50 µm show extra conductance minima in addition to the MDP at roughly the same gate voltage, suggesting an intrinsic lattice related origin of these features.

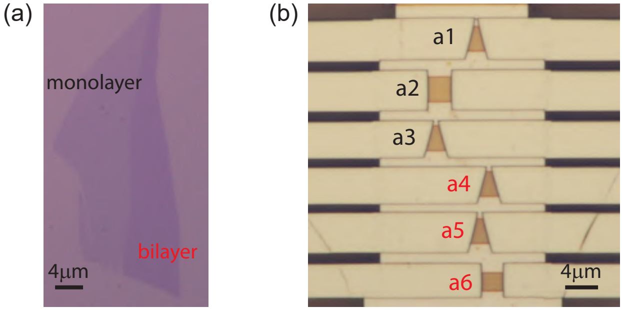

Figure E.1. **(a)** Micrograph of the graphene flake used for sample a. **(b)** Micrograph of all six finished fully encapsulated devices. a1-a3 are monolayer and a4-a6 are bilayer.

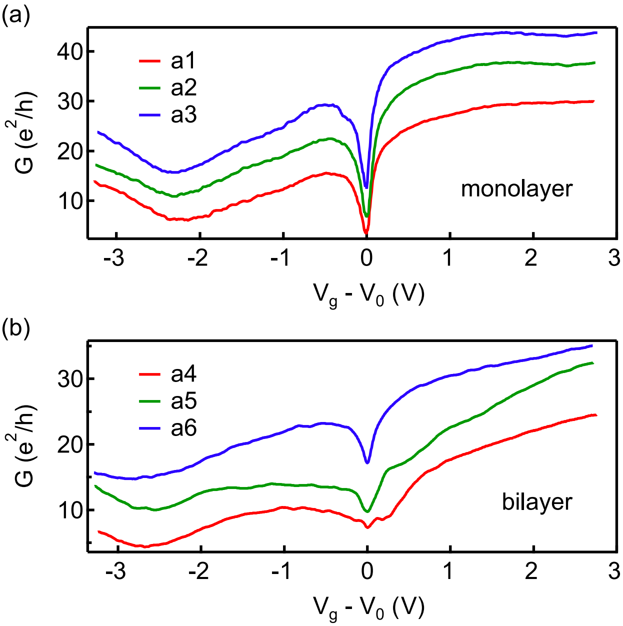

Figure E.2. Two-terminal differential conductance G as a function of gate voltage V_g measured at 4.2 K for all three monolayer devices **(a)** and all three bilayer devices **(b)**. V_0 is around 250 mV for all devices. Curves are shifted by $5e^2/h$ sequentially in y direction for clarity.

E.2.1. Device a3

The two-terminal differential conductance of monolayer device a3 is plotted as a function of charge carrier density n in Fig. E.3(a). In addition to the MDP, two pairs of conductance minima occur symmetrically at $n \approx \pm 2.4 \times 10^{12}\,\mathrm{cm}^{-2}$ and $n \approx \pm 1.4 \times 10^{12}\,\mathrm{cm}^{-2}$, respectively, exactly the same as in device a2 in chapter 8. The Landau fan diagram (see Fig. E.3(b)) also looks very similar as that of device a2.

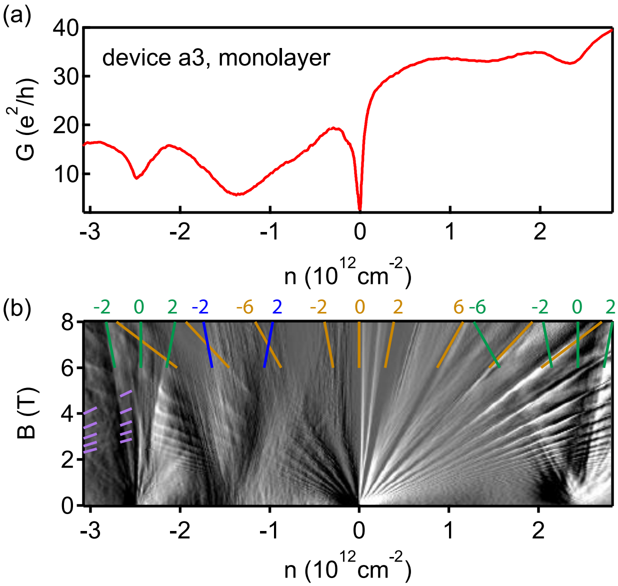

Figure E.3. Electronic transport of device a3 at 4.2 K. **(a)** Two-terminal differential conductance G as a function of charge carrier density n. **(b)** $\mathrm{d}G/\mathrm{d}n$ as a function of n and B of the same device. Filling factors are indicated on top of the diagram. The dashed lines mark the indications of filling factors fanning out from higher densities.

E.3. Other devices of sample b

The graphene flake used for sample b is shown in Fig. E.4(a). Ten fully encapsulated devices were fabricated out of this flake as depicted in Fig. E.4(b), with five monolayer devices, four bilayer devices and one trilayer device. The second device shown in chapter 8 is device b2. Here, we show the gate traces for all devices. Unfortunately, the gate started to leak during the measurements.

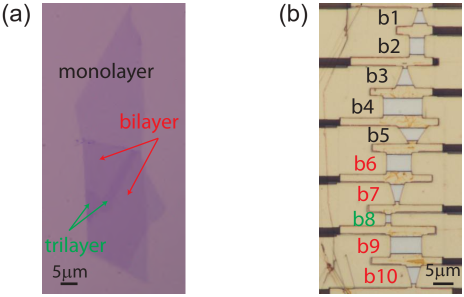

Figure E.4. **(a)** Micrograph of the graphene flake used for sample b. **(b)** Micrograph of all ten finished fully encapsulated devices. b1-b5 are monolayer, b6, b7, b9, b10 are bilayer and b8 is trilayer.

Two-terminal differential conductance of all ten devices are plotted as a function of gate voltage in Fig. E.5. The additional DPs occur at slightly different gate voltages for different devices. One reason for that might be the gate leak, resulting in different lever arms for different devices. The measuring sequence is the same as the labeling, with device b1 measured first and device b10 measured last. The second reason might be a tiny relative rotation of any of the three layers at different locations due to bubbles or ripples formed in the stack during fabrication [37], which leads to effectively slightly different MSLs for different devices. In Fig. E.5(c), it seems the 3L-MSL DP is almost absent in the trilayer device, which is expected due to the further separation of the top 2L-MSL and the bottom 2L-MSL.

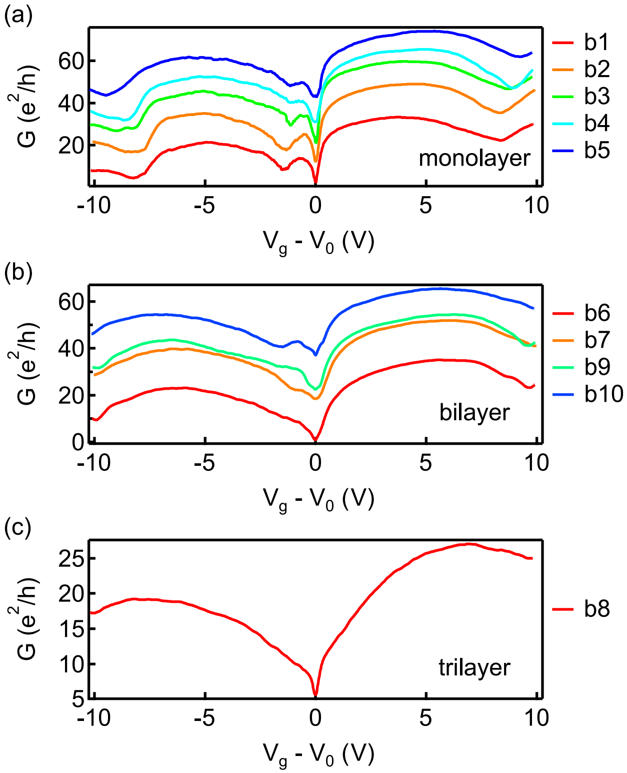

Figure E.5. Two-terminal differential conductance G as a function of gate voltage V_g measured at 4.2 K for all five monolayer devices **(a)**, all four bilayer devices **(b)** and one trilayer device **(c)**. V_0 varies from 20 mV to 220 mV for different devices. Curves are shifted by $10e^2/h$ sequentially in y direction for clarity.

Curriculum Vitae

Lujun Wang
Born on 15th December 1989 in Dainan, Jiangsu, China

Education

12/2015–12/2019	**PhD in Experimental Physics at the University of Basel, Switzerland** - Dissertation in the group of Prof. Dr. Christian Schönenberger *“Quantum Transport Experiments in Strain-Engineered Graphene”*
4/2013–7/2015	**Master of Science in Applied and Engineering Physics at the Technical University of Munich, Germany** - Master thesis in the group of Prof. Dr. Rudolf Gross *“Fabrication Stability of Josephson Junctions for Superconducting Qubits”*
9/2008–7/2012	**Bachelor of Science in Physics at Nanjing University, China**
2005–2008	**Yangzhou High School, Yangzhou, China**

Positions

12/2015–	*Teaching assistant for physics at the University of Basel*

Awards

2019	*Best poster prize at the international conference IWEPNM 2019*
2010	*Renmin scholarship at Nanjing University*

Publications

- *"Strain-induced scalar potential and pseudomagnetic field in graphene"*
  L. Wang, A. Baumgartner, P. Makk, S. Zihlmann, K. Watanabe, T. Taniguchi and C. Schönenberger
  in preparation
- *"Compact SQUID realized in a double layer graphene heterostructure"*
  D. I. Indolese, P. Karnatak, A. Kononov, R. Delagrange, R. Haller, **L. Wang**, P. Makk, K. Watanabe, T. Taniguchi, and C. Schönenberger
  arXiv:2006.05522 (2020)
- *"Out-of-plane corrugations in graphene based van der Waals heterostructures"*
  S. Zihlmann, P. Makk, M. K. Rehmann, **L. Wang**, M. Kedves, D.Indolese, K. Watanabe, T. Taniguchi, D. M. Zumbühl, and C. Schönenberger
  arXiv:2004.02690 (2020)
- *"Mobility enhancement in graphene by in situ reduction of random strain fluctuations"*
  L. Wang, P. Makk, S. Zihlmann, A. Baumgartner, D. I. Indolese, K. Watanabe, T. Taniguchi and C. Schönenberger
  Phys. Rev. Lett. **124**, 157701 (2020)
- *"In situ strain tuning in hBN-encapsulated graphene electronic devices"*
  L. Wang, S. Zihlmann, A. Baumgartner, J. Overbeck, K. Watanabe, T. Taniguchi, P. Makk and C. Schönenberger
  Nano Letters **19**, 4097 (2019)
- *"New generation of moiré superlattices in doubly aligned hBN/graphene/hBN heterostructures"*
  L. Wang, S. Zihlmann, M.-H. Liu, P. Makk, K. Watanabe, T. Taniguchi, A. Baumgartner and C. Schönenberger
  Nano Letters **19**, 2371 (2019)

Talks

- *Mobility enhancement in graphene by in situ reduction of random strain fluctuations*

4th Graphene and 2D Heterostructure Workshop, Budapest (Hungary), October 2019

- *Super-superlattice and strain engineering in hBN-encapsulated graphene*
  Annual meeting of the Swiss Nanoscience Institute, Lenzerheide (Switzerland), September 2019

- *Strain engineering in graphene*
  Group seminar, Nanoelectronics Research Lab, Budapest (Hungary), June 2019

- *New generation of moiré superlattices in doubly aligned hBN/graphene/hBN heterostructures*
  Moiré in Paris 2019, Paris (France), June 2019

- *Towards valley Hall physics by engineering strain in graphene*
  QCQT Research Seminar, Basel (Switzerland), November 2018

- *Strain engineering in graphene*
  3rd Graphene Workshop, Basel (Switzerland), June 2018

- *Towards valleytronics in strain-engineered graphene*
  Winter School of the Swiss Nanoscience Institute, Mürren (Switzerland), January 2018

- *Towards valleytronics in strain-engineered graphene*
  QSIT Junior Meeting, Passugg (Switzerland), June 2016

Poster Contributions

- *“Three-layer moiré superlattice and strain engineering in hBN-encapsulated graphene”*
  IWEPNM, Kirchberg (Austria), March 2019

- *“Towards valleytronics in strain-engineered graphene”*
  Winter School of the Swiss Nanoscience Institute, Braunwald (Switzerland), January 2019

- *“Towards valleytronics in strain-engineered graphene”*
  Graphene Week 2018, San Sebastian (Spain), September 2018

- *“Towards valleytronics in strain-engineered graphene”*
  QSIT Winter School, Arosa (Switzerland), February 2018

- *“Towards valleytronics in strain-engineered graphene”*
  Annual Meeting of the Swiss Nanoscience Institute, Lenzerheide (Switzerland), September 2017
- *“Towards valleytronics in strain-engineered graphene”*
  Swiss Nano Convention, Fribourg (Switzerland), June 2017
- *“Towards valleytronics in strain-engineered graphene”*
  IWEPNM, Kirchberg (Austria), March 2017
- *“Towards valleytronics in strain-engineered graphene”*
  Winter School of the Swiss Nanoscience Institute, Zermatt (Switzerland), January 2017
- *“Towards valleytronics in strain-engineered graphene”*
  Annual Meeting of the Swiss Nanoscience Institute, Lenzerheide (Switzerland), September 2016
- *“Electron optics in ballistic suspended graphene”*
  Swiss Nano Convention, Basel (Switzerland), June 2016

Acknowledgements

> *For His invisible attributes, namely, His eternal power and divine nature, have been clearly perceived, ever since the creation of the world, in the things that have been made. So they are without excuse.*
>
> – Romans 1:20 (ESV)

This PhD thesis would not have been possible without the help and support from many people. In the following, I would like to express my sincere gratitude to all of them for their precious contributions.

First of all, I would like to thank my thesis advisor Prof. Dr. Christian Schönenberger for giving me the opportunity to perform my doctoral research in his group. His passion for science was always an encouragement for me to face all the challenges I encountered in the past four years. I am very grateful for the freedom he gave me for my project. One of the most valuable lessons I learned is the conclusion of his lecture at one of the SNI winter schools–"Don't always listen to your professor, surprise him/her afterwards!" It was this lesson that helped to make all the achievements in this thesis possible. Christian is a leader who serves his team. He created an absolutely enjoyable working environment in the group. I still remember clearly the scene during one of our group excursions that he was cooking in the kitchen while his students were playing games and waiting in the dinning room. That picture will always be an inspiration for me if I would have the chance to become a leader in the future. I am also very thankful for his kindness. I will never forget the concerns and wishes he sent me during the two consecutive emergencies that I had to fly back to China. That supported me a lot during that tough time. All in all, it was a really wonderful and beneficial four years working with Christian, not only in terms of science, but also in many other aspects.

Second, I would like to thank Prof. Dr. Christoph Stampfer and Prof. Dr. Dmitri K. Efetov for making the effort to read my thesis. It is my great honor to have two such excellent physicists in my PhD committee.

I am very grateful to Péter Makk. Although he moved back to Budapest already in the second year of my PhD, his strong support never ceased. He could still find the appropriate way to push me, which helped a lot the project move forward. The countless discussions we had over Skype were certainly an indispensable element for our achievements. He always tried to and also motivated me to talk to different experts during conferences, which led to a deeper understanding of our data. Many thanks also go to Simon Zihlmann, who was not my postdoc officially but helped me more than a postdoc. His unlimited great ideas were one of the key factors that helped to get my PhD on the right track. The critical questions he raised for the manuscripts always hit the point and made me think twice about what I had written. It was also him who helped me troubleshoot problems with the measurement setup and introduced me to many tricks of Igor. I am very thankful to Andreas Baumgartner as well, from whom I learned a lot about lock-in and cryostat. The fruitful discussions with him always gave me inspirations for trying new ideas of interpreting our puzzling data. His fast and efficient simulations surely added more impact to our work. His amazing language polishing definitely made our manuscripts more enjoyable to read.

I would like to thank Ming-Hao Liu for the great collaborations. The beautiful illustration he made for the double moiré is still my favorite. I am looking forward to the simulation results of our new on-going collaborations. Special thanks go to Jan Overbeck and Oliver Braun, who spent a lot of time working with me on straining suspended graphene in the early time. I would also like to thank the other member of the graphene team–David Indolese, with whom I shared both excitements and frustrations in the lab, and also the bed at conferences! I am very thankful to Peter Rickhaus as well, with whom I had a lot of insightful discussions. The discussions with Paritosh Karnatak also helped to solve many of my questions about the physics of graphene. I am also very grateful to Minkyung Jung. Although we had only a few months overlap, I was benefiting a lot from his encouragements–"You should make more samples!" The nice furniture he gave me is still in use! Moreover, I would like to thank Gergő Fülöp and Joost Ridderbos for their help with programming. Thanks also go to Alessia Pally for helping me hold the break-out box during one cool-down, which (she claims) might be a relevant factor for the measurement results.

The PhD life would not have been so colorful without the lovely colleagues. With Arunav Bordoloi I shared a lot of fun time outside of work, be it playing Badminton, taking swimming courses or simply going for dinner. With him I also had my first (probably also the last) mountain biking trip in Switzerland! Having drinks with the gxxxxp boys–Frederick Thomas and Christian Jünger always brought a lot of laughter. The barbecues and Rhein swimming we had together definitely made the PhD life a lot more special and unforgettable. The firework watching event organized by Roy Haller was one of the highlights of the group activities. I also enjoyed a lot the discussions with Mirko Rehmann on all kinds of topics at the SNI events. Furthermore, I would like to thank all former and current members of the Nanoelectronics group: Jörg Gramich, Thomas Hasler, Clevin Handschin, Vishal Ranjan, Kishan Todkar, Gulibusi-

tan Abulizi, Raphaëlle Delagrange, Maria El Abbassi, Mihai-Cezar Harabula, Anton Vladyka, Masoud Baghernejad, Michel Calame, Malin Nilsson, Artem Kononov, Blesson Varghese, Luk Yi Cheung, Ian Correa Sampaio, Martin Endres, Olivier Faist, Lukas Gubser, Zarina Mingazheva, Mehdi Ramezani, Jann Ungerer, Dario Sufra and Melissa Osterwalder.

Special thanks also go to many people behind the scene at the Physics Department. Barbara Kammermann and Astrid Kalt were the best secretaries I ever met, from whom I got extremely helpful assistance to all administrative work. I am especially thankful to Sascha Martin and his excellent team at the mechanical workshop, without whom the strain experiments would not have been possible. I would also like to thank Dominik Sifrig for the supply of helium, Patrick Stöcklin for the help in the cryolab, Daniel Sacker and Laurent Marot for the help with the cleanroom.

Apart from science, I am very grateful to my parents and my sister for their unlimited support in all aspects throughout my life and accepting me as who I am. Their understanding, accompanying and encouragements gave me a lot of strength to get through the hard times. I would also like to thank all the friends from the Chinese Christian Church in Basel, especially the Youth Group, who made me feel like home and gave me support like family.

Without all these people I would not be where I am today.